EXPERIMENTAL ROLL-DAMPING, MAGNUS, AND STATIC-STABILITY CHARACTERISTICS OF TWO SLENDER MISSILE CONFIGURATIONS AT HIGH ANGLES OF ATTACK (0 TO 90 DEG) AND MACH NUMBERS 0.2 THROUGH 2.5

L. JENKE

VON KÁRMÁN GAS DYNAMICS FACILITY
ARNOLD ENGINEERING DEVELOPMENT CENTER
AIR FORCE SYSTEMS COMMAND
ARNOLD AIR FORCE STATION, TENNESSEE 37389

July 1976

Final Report for Period June 16 — September 18, 1975

Prepared for

AIR FORCE FLIGHT DYNAMICS LABORATORY (FGC)
WRIGHT-PATTERSON AIR FORCE BASE, OHIO 45433

NOTICES

When U. S. Government drawings specifications, or other data are used for any purpose other than a definitely related Government procurement operation, the Government thereby incurs no responsibility nor any obligation whatsoever, and the fact that the Government may have formulated, furnished, or in any way supplied the said drawings, specifications, or other data, is not to be regarded by implication or otherwise, or in any manner licensing the holder or any other person or corporation, or conveying any rights or permission to manufacture, use, or sell any patented invention that may in any way be related thereto.

Qualified users may obtain copies of this report from the Defense Documentation Center.

References to named commercial products in this report are not to be considered in any sense as an endorsement of the product by the United States Air Force or the Government.

This report has been reviewed by the Information Office (OI) and is releasable to the National Technical Information Service (NTIS). At NTIS, it will be available to the general public, including foreign nations.

APPROVAL STATEMENT

This technical report has been reviewed and is approved for publication.

FOR THE COMMANDER

CARL J. SCHULZE
Major, USAF
Chief Air Force Test Director, VKF
Directorate of Test

WILLIAM K. OFFICER
Colonel, USAF
Director of Test, Acting

REPORT DOCUMENTATION PAGE		READ INSTRUCTIONS BEFORE COMPLETING FORM
1 REPORT NUMBER AEDC-TR-76-58	2. GOVT ACCESSION NO.	3 RECIPIENT'S CATALOG NUMBER
4 TITLE (and Subtitle) EXPERIMENTAL ROLL-DAMPING, MAGNUS, AND STATIC-STABILITY CHARACTERISTICS OF TWO SLENDER MISSILE CONFIGURATIONS AT HIGH ANGLES OF ATTACK (0 TO 90 DEG) AND MACH NUMBERS 0.2 THROUGH 2.5		5 TYPE OF REPORT & PERIOD COVERED Final Report - June 16 - September 18, 1975 6. PERFORMING ORG. REPORT NUMBER
7 AUTHOR(s) Leroy M. Jenke - ARO, Inc.		8. CONTRACT OR GRANT NUMBER(s)
9 PERFORMING ORGANIZATION NAME AND ADDRESS Arnold Engineering Development Center (XO) Air Force Systems Command Arnold Air Force Station, Tennessee 37389		10. PROGRAM ELEMENT, PROJECT, TASK AREA & WORK UNIT NUMBERS Program Element 62201F Project 8219
11. CONTROLLING OFFICE NAME AND ADDRESS Air Force Flight Dynamics Laboratory (FGC) Wright-Patterson Air Force Base Ohio 45433		12. REPORT DATE July 1976 13. NUMBER OF PAGES 112
14 MONITORING AGENCY NAME & ADDRESS(if different from Controlling Office)		15 SECURITY CLASS. (of this report) UNCLASSIFIED 15a. DECLASSIFICATION/DOWNGRADING SCHEDULE N/A

16. DISTRIBUTION STATEMENT (of this Report)

Approved for public release; distribution unlimited.

17. DISTRIBUTION STATEMENT (of the abstract entered in Block 20, if different from Report)

18 SUPPLEMENTARY NOTES

Available in DDC

19. KEY WORDS (Continue on reverse side if necessary and identify by block number)

damping
roll
static stability
Magnus force
wind tunnel tests
angle of attack
missile configurations
transonic flow
supersonic flow

20 ABSTRACT (Continue on reverse side if necessary and identify by block number)

An experimental investigation was conducted to verify that the recently developed high-alpha missile roll-damping test mechanism could be used to obtain the roll-damping characteristics of slender missile configurations and to obtain roll-damping, Magnus, static-stability, and axial-force characteristics of a typical missile configuration. The verification tests were conducted with the Basic Finner Model at M_∞ = 0.22 and 2.50. Additional test

DD FORM 1 JAN 73 1473 EDITION OF 1 NOV 65 IS OBSOLETE

20. ABSTRACT (Continued)

results were obtained with a Modified Basic Finner Model for Mach number 0.6 through 2.5. Data were obtained for angles of attack from -5 to 90 deg and Reynolds numbers, based on model diameter, of 1 x 10^5 through 6 x 10^5. Both spin-up (canted fins) and spin-down (zero cant) data were recorded and the spin rate ranged from 0 to 1,250 radian/sec. Results of these tests are presented showing the effects of angle of attack, Mach number, Reynolds number, spin rate, and the support system on the roll-damping, Magnus, static-stability, and axial-force characteristics of two missile configurations. The results show that the roll-damping and Magnus characteristics are very nonlinear with spin rate at high angles of attack (α > 20 deg) and low Mach numbers ($M_\infty \leq 1.5$). In addition, large and erratic variations in side force and yawing moment were recorded at low spin rates (p < 100 radian/sec) for $M_\infty \leq 1.5$. The models also exhibited high autorotation characteristics (p $\approx$ 840 radian/sec) with zero canted fins at M_∞ < 0.9.

AFSC
Arnold AFS Tenn

PREFACE

The work reported herein was conducted by the Arnold Engineering Development Center (AEDC), Air Force Systems Command (AFSC), for the Air Force Flight Dynamics Laboratory (AFFDL), AFSC, under Program Element 62201F, Project 8219. The AFFDL project monitor was Dr. Robert C. Nelson. The results were obtained by ARO, Inc. (a subsidiary of Sverdrup & Parcel and Associates, Inc.), contract operator of AEDC, AFSC, Arnold Air Force Station, Tennessee. The work was done under ARO Project Numbers V41A-A8A and P41C-A0A. The project engineer for the Propulsion Wind Tunnel Facility test (M_∞ = 0.6 to 1.3) was Robert Paulk, ARO, Inc; the project engineer for the von Kármán Gas Dynamics Facility test and the author of this report was Leroy M. Jenke, ARO, Inc. The final data package was completed on November 18, 1975, and the manuscript (ARO Control No. ARO-VKF-TR-76-13) was submitted for publication February 9, 1976.

CONTENTS

Page

1.0 INTRODUCTION 5
2.0 APPARATUS
2.1 Models 5
2.2 Test Mechanism 6
2.3 Instrumentation 6
2.4 Test Facilities 7
3.0 PROCEDURE
3.1 Test Conditions 7
3.2 Test Procedure 9
3.3 Data Reduction Procedure 9
4.0 PRECISION OF MEASUREMENTS
4.1 Test Conditions 12
4.2 Roll Damping Data 12
4.3 Static-Stability Data 13
5.0 RESULTS AND DISCUSSION 14
6.0 CONCLUSIONS 17
REFERENCES 18

ILLUSTRATIONS

Figure

1. Model Photographs 19
2. Model Details 21
3. High-Alpha Missile Roll-Damping Test Mechanism 22
4. Photographs of the Test Mechanism 24
5. Brake Calibration 29
6. Test Facilities 30
7. Bearing Rolling-Moment Contributions 32
8. Variation of $C\ell_T$ with Spin Rate for the Basic Finner Model 35
9. Roll-Damping Characteristics of the Basic Finner Model 38
10. Variation of $C\ell_T$ with Spin Rate for the Modified Basic Finner Model 41
11. Autorotation Chacteristics of the Modified Basic Finner Model 55
12. Variation of $C\ell_p$ with Angle of Attack for the Modified Basic Finner Model, Linear Damping 56
13. Approximate Regions of Nonlinear Damping 59

Figure Page

14. Magnus-Force and Moment Characteristics of the Basic Finner Model 60
15. Variation of C_{Y_p} with C_{n_p} with Angle of Attack for the Basic Finner Model 62
16. Magnus-Force and Moment Characteristics of the Modified Basic Finner Model 65
17. Variation of C_{Y_p} with C_{n_p} with Angle of Attack for the Modified Basic Finner Model 79
18. Static Longitudinal Stability Characteristics of the Basic Finner Model, $p \approx 100$ radians/sec 87
19. Variation in Directional Stability with Angle of Attack for the Basic Finner Model 89
20. Axial Force Characteristics of the Basic Finner Model, $p \approx 100$ radians/sec 91
21. Static Longitudinal Stability Characteristics of the Modified Basic Finner Model, $p \approx 100$ radians/sec 92
22. Variation of Directional Stability with Angle of Attack for the Modified Basic Finner Model, $p \approx 100$ radians/sec 101
23. Axial-Force Characteristics of the Modified Basic Finner Model, $p \approx 100$ radians/sec 109

NOMENCLATURE 110

1.0 INTRODUCTION

A current trend in missile development is toward large fineness ratio configurations which are highly maneuverable. The damping derivatives (pitch, yaw and roll), especially on slender vehicles with fins, have a strong influence on the vehicle response at extreme maneuver conditions. Theoretical predictions at best apply only at low angles of attack, and since the new missiles are highly maneuverable, large angle-of-attack experimental data are desired for the computerized flight trajectory programs.

A program was initiated at the Arnold Engineering Development Center (AEDC), von Kármán Gas Dynamics Facility (VKF), by the Air Force Flight Dynamics Laboratory (AFFDL) for the purpose of developing the capability for obtaining high angle-of-attack roll-damping, Magnus, and static-stability data on current missile configurations. The developed mechanism has an angle-of-attack range of approximately -5 to 90 deg and was designed for use in both the VKF Tunnel A (M_∞ = 1.5 to 6.0) and PWT Tunnel 4T (M_∞ = 0.2 to 1.3).

Wind tunnel tests were conducted on two missile configurations at Mach numbers of 0.22 through 2.50 utilizing the free spin test technique. Data were obtained at angles of attack from -5 to 90 deg at Reynolds numbers, based on diameter, from 1 x 10^5 to 6 x 10^5.

2.0 APPARATUS

2.1 MODELS

Two stainless steel models (Figs. 1 and 2) were designed and fabricated by AEDC for these tests. One of them is commonly referred to as the Basic Finner. It consists of a cone-cylinder with four rectangular fins. Overall model length is ten calibers, the cone half-angle is 10 deg, and the fins are approximately one caliber in chord and have an overall span of three calibers. Three interchangeable sets of fins with cant angles of 0, 2.5, and 5 deg were tested. One additional configuration, the Modified Basic Finner, was also tested. It utilized the same body but used an ogive nose and four fins with a trapezoidal planform and zero cant angle.

The models were dynamically balanced in roll (±1 in. gm) at the VKF so that there would be no vibrational loads on the balance. The moments of inertia (Fig. 2) of the models, determined by VKF, are considered to be accurate to ±0.5 percent.

2.2 TEST MECHANISM

The VKF high-alpha missile roll-damping test mechanism (Figs. 3 and 4) is a free-spin system. A six-component balance is supported by a strut that can be manually set in 6-deg increments to provide various prebend angles. These manual settings along with the tunnel pitch mechanism provide an angle-of-attack range from -5 to 90 deg. The balance supports an adapter with three ball bearings, and the model is mounted directly to the bearings. An air-operated brake is located on the front of the adapter and is used to stop model rotation. The maximum dynamic braking moment produced by the brake is 13.5 in.-lb (Fig. 5); however, this could possibly be increased by using different braking materials. The brake as well as a mechanical lock can be used to obtain static force coefficients at zero spin rate. Roll-damping data are obtained as the model spins up (for models with canted fins) or as the model spins down after it is spun up by high-pressure air jets impinging on the fins.

The rotational speed, roll position, and roll direction are computed from the electrical pulses produced by a ring with alternating reflective and nonreflective surfaces passing three internally mounted infrared-emitting diodes and phototransistors. The mechanism is designed for spin rates up to 12,000 rpm and normal force loads of 300 lb.

2.3 INSTRUMENTATION

Model forces and moments were measured with the VKF six-component, moment-type, strain-gage balance (-71). The small outrigger side beams (Fig. 4e) of the balance were used to obtain the sensitivity required to measure small side loads while maintaining adequate balance stiffness for the larger pitch loads. A normal-force to side-force capability ratio of six was achieved for a 300-lb normal-force loading. The balance design loads and uncertainties are as follows:

		Tunnel A Tests		Tunnel 4T Tests	
Balance Component	Design Load	Range of Static Loads	Measurement Uncertainty	Range of Static Loads	Measurement Uncertainty
Normal Force, lb	±300	±200	±0.40	±300	±0.69
Pitching Moment[a], in.-lb	±820	±400	±0.70	±820	±1.02
Side Force, lb	± 50	± 15	±0.15	± 50	±0.15
Yawing Moment[a], in.-lb	±135	± 30	±0.15	±135	±0.29
Rolling moment, in.-lb	± 30	± 8	±0.04	± 30	±0.08
Axial Force, lb	± 50	± 10	±0.08	± 50	±0.18

[a] About the balance forward moment bridge

The transfer distance to the model moment reference was measured with a precision of ±0.005 in.

2.4 TEST FACILITIES

Supersonic Wind Tunnel A (Fig. 6a) is a continuous, closed-circuit, variable-density wind tunnel with an automatically driven flexible-plate-type nozzle and a 40- by 40-in. test section. The tunnel can be operated at Mach numbers from 1.5 to 6.0 at maximum stagnation pressures from 29 to 200 psia, respectively, and stagnation temperatures up to 750°R (M_∞ = 6). Minimum operating pressures range from about one-tenth to one-twentieth of the maximum at each Mach number. Although Tunnel A is primarily a supersonic tunnel, it can also be operated subsonically from Mach numbers 0.2 to 0.8 by opening the throat (M_∞ = 1.2 setting) and closing the diffuser until the tunnel chokes at that point. The tunnel is equipped with a model injection system which allows removal of the model from the test section for model changes while the tunnel remains in operation.

The Aerodynamic Wind Tunnel 4T (Fig. 6b) is a closed-circuit, continuous flow, variable density tunnel capable of being operated at Mach numbers from 0.20 to 1.30. At all Mach numbers, the stagnation pressure can be varied from about 2 to 27 psia. The test section is 48 in. square and 150 in. long with perforated, variable-porosity (0.5 to 10 percent) walls. It is completely enclosed in a plenum chamber from which the air can be evacuated, allowing part of the tunnel airflow to be removed through the perforated walls of the test section. The wall perforations are 0.50-in.-diam holes inclined 60 deg from the normal to the wall surface. This design allows control of wave attenuation and blockage effects. Further control of wall interference effects can be accomplished by converging or diverging the top and bottom test section walls by as much as 0.50 deg. The tunnel model support system consists of a pitch sector, strut, and sting attachment receptacle, and the system has a pitch capability of from -12 to 28 deg with respect to the tunnel centerline.

3.0 PROCEDURE

3.1 TEST CONDITIONS

The nominal test conditions for these tests and a complete test summary are listed below.

Nominal Test Conditions

M_∞	p_o, psia	T_o, °R	q_∞, psia	V_∞, ft/sec	Re x 10^{-6}, ft^{-1}	Re_d x 10^{-5}
0.22[a]	7.40	560	0.24	254	0.70	1.05
0.60	7.85	570	1.55	678	1.73	2.60
0.60	12.64	↓	2.50	678	2.78	4.17
0.90	6.25	↓	2.10	977	1.73	2.60
0.90	10.07	↓	3.38	977	2.78	4.17
1.15	9.51	↓	3.87	1196	2.78	4.17
1.30	9.51	↓	4.06	1315	2.78	4.17
1.50	5.93	560	2.54	1444	1.72	2.58
1.50	9.48	↓	4.07	1444	2.75	4.13
1.76	10.25	↓	4.11	1604	2.75	4.13
2.00	7.00	↓	2.51	1729	1.71	2.57
2.00	11.20	↓	4.01	1729	2.73	4.10
2.25	12.57	↓	3.85	1839	2.73	4.10
2.49[a]	6.50	↓	1.66	1929	1.24	1.86
2.49	8.90	↓	2.30	1929	1.71	2.57
2.50	14.25	↓	3.65	1933	2.73	4.10
2.50[a]	20.80	↓	5.33	1933	3.98	5.97

[a] For the Basic Finner Model

Test Summary[a]

M_∞	Re_d x 10^{-5}	Angle-of-Attack Range, deg	
		Basic Finner	Modified Basic Finner
0.22	1.05	-5 to 83	---
0.60	2.60	---	-5 to 90
0.60	4.17	---	-5 to 63
0.90	2.60	---	-5 to 90
0.90	4.17	---	-5 to 28
1.15	4.17	---	-5 to 90
1.30	4.17	---	-5 to 90
1.50	2.58	---	-5 to 43
1.50	4.13	---	-5 to 65
1.76	4.13	---	-5 to 90
2.00	2.57	---	-5 to 65
2.00	4.10	---	-5 to 90
2.25	4.10	---	-5 to 90
2.49	1.86	-5 to 90[b]	---
2.49	2.57	---	-5 to 90
2.50	4 10	---	-5 to 90
2.50	5.97	-5 to 43[b]	---

[a] Data were generally recorded every 2.5 deg.

[b] Data were also obtained with a straight sting for α = -5 to 20 deg.

3.2 TEST PROCEDURE

The test procedure, for models with zero fin cant, was to position the model at the desired altitude; set the spin air pressure to a sufficiently high value (up to 3,000 psi); open a solenoid valve; when the desired spin rate was achieved, close the solenoid valve; and record data as the spin rate decreased. For models with canted fins, the test procedure was to set the brake pressure sufficiently high to prevent model rotation, the brake was released, and data were recorded as the spin rate increased. Some additional data were recorded with the brake on (zero spin rate).

3.3 DATA REDUCTION PROCEDURE

3.3.1 Roll Damping

The one-degree-of-freedom equation of motion in roll can be written as

$$I_x\ddot{\phi} = L_T \tag{1}$$

where L_T is the total rolling moment. By assuming linear aerodynamics (i.e., $L_T = L_o + L_p\, p$), the equation of motion becomes

$$I_x\ddot{\phi} = L_o + L_p p$$

With the initial conditions, $\dot{\phi} = p_I$ and $\phi = \phi_I$ at $t = t_I$, this equation can be integrated to give

$$\dot{\phi} = p = \left(p_I - \frac{L_o}{L_p}\right) e^{\frac{L_p}{I_x}(t-t_I)} - \frac{L_o}{L_p} \tag{2}$$

$$\phi = \left(p_I + \frac{L_o}{L_p}\right)\left[e^{\frac{L_p}{I_x}(t-t_I)} - 1\right] \times \frac{I_x}{L_p} - \frac{L_o}{L_p}(t - t_I) + \phi_I \tag{3}$$

Equation (3) was fitted to approximately 200 points of roll position (ϕ), time (t) data using a differential correction, least-squares technique to determine the constants L_o, L_p, p_I, and ϕ_I. Equation (2) was then used to calculate the roll rate.

The accuracy of the fit of the equation to the data is determined by the standard deviation of the roll position ($\delta\phi$) defined as

$$\delta\phi = \left[\sum_{i=1}^{N_p} \left(\phi_c - \phi_d\right)_i^2 \Big/ \left(N_p - N_c\right)\right]^{1/2}$$

where ϕ_c is the calculated value from the fitted equation, ϕ_d is the measured value. N_p is the number of data points, and N_c is the number of constants determined (4 in this case). If $\delta\phi$ is large compared to the uncertainty of the measurement, the linear equation does not adequately describe the rolling moment. This was found to be the case for subsonic speeds and high angles of attack over a large range of roll rates. For these conditions, the following equation was assumed for the rolling moment:

$$L_T = L_0 + L_{p_1}\dot{\phi} + L_{p_2}\dot{\phi}^2 + L_{p_3}\dot{\phi}^3 + L_{p_5}\dot{\phi}^5$$

The equation of motion thus becomes

$$I_x\ddot{\phi} = L_0 + L_{p_1}\dot{\phi} + L_{p_2}\dot{\phi}^2 + L_{p_3}\dot{\phi}^3 + L_{p_5}\dot{\phi}^5 \qquad (4)$$

with the same aforementioned boundary conditions. Since Eq. (4) cannot be solved explicitly for ϕ as a function of time, Eq. (4) is fitted to the ϕ,t data using a numerical technique established by Chapman and Kirk (Ref. 1). In the data reduction scheme, if the linear equation does not provide a satisfactory fit as determined from $\delta\phi$, the additional terms in Eq. (4) (L_{p_2}, L_{p_3}, and L_{p_5}) are added one at a time until a satisfactory fit is obtained.

For the linear data, it is convenient to discuss the data as a rolling-moment coefficient at p = 0, $C\ell_0$, and a roll-damping coefficient $C\ell_p$ defined as

$$C\ell_0 = \left(L_{0_w} - L_{0_B}\right)/q_\infty Ad$$

$$C\ell_p = \left(L_{p_w} - L_{p_B}\right)(2V_\infty)/q_\infty Ad^2$$

where the subscripts w and B denote wind-on and bearing, respectively. It is notable that $C\ell_0$ is the static rolling-moment coefficient caused by fin cant, striations, etc., averaged over ϕ from 0 to 360 deg.

For the nonlinear cases, the roll damping coefficient has little significance. Therefore, these data are discussed in terms of the total rolling-moment coefficient:

$$C\ell_T = \left(L_{T_w} - L_{T_B}\right)/q_\infty Ad$$

It was found that some of the data were so nonlinear that even the nonlinear equation of motion would not adequately describe the total rolling moment. For these data, the ϕ,t data were divided into several overlapping segments and Eq. (3) was fitted to each segment.

The bearing contribution was evaluated by fitting the equation of motion to roll rate and time data obtained at vacuum conditions and from the recorded variations of the static rolling moment of the balance with spin rate at each test condition. The results presented in Fig. 7a clearly show the effect of atmospheric pressure on the total rolling moment of the model-bearing system. The bearing static rolling moment (L_{o_B}) and damping moment terms (L_{p_1}, L_{p_2}, L_{p_3}, and L_{p_5}) of the equation of motion, which were obtained at each pressure level, can be plotted as a function of atmospheric pressure and their extrapolated values at zero pressure correspond to the bearing contribution (bearing tare values). It was found that the higher order terms (L_{p_2}, L_{p_3}, and L_{p_5}) were zero at vacuum and that only L_{o_B} and $L_{p_{1_B}}$ were required in the data reduction. The variation of L_{o_B} with bearing load (model normal force) was determined from the measured balance rolling moment (Fig. 7b). By extrapolating to zero spin rate (p = 0), the static rolling moment for a given load could be determined. The variation of L_{o_B} with $F_{N_{B_T}}$ (total bearing normal-force loading) is presented in Fig. 7c. The results show that the magnitude of L_{o_B} varies considerably with each test installation since the bearings were changed and the preloading applied to the bearing during installation could not be accurately repeated (compare the three test installations). The value of L_{o_B} was very significant at the high load conditions in correcting the total roll moment. The bearing roll damping (L_{p_B}) showed little variation with load and was, therefore, considered to be a constant value.

3.3.2 Static Stability

The static stability and Magnus force and moment data were reduced with the standard VKF and PWT static-stability data reduction program and each plotted data point is the average of several recorded data points. The static-stability data are time correlated with the roll rate data obtained from the fitting techniques.

Values of C_{Y_p} and C_{n_p} were determined with the computer by fitting a linear least-squares curve fit to a section of C_Y versus $pd/2V_\infty$ and C_n versus $pd/2V_\infty$, respectively. For Mach numbers 0.22 to 1.30, the range of $pd/2V_\infty$ fitted was 0.005 to 0.03. For Mach numbers of 1.5 to 2.5, the range of $pd/2V_\infty$ fitted was 0.0005 to 0.0180.

As a result of the large amount of data recorded, most of the presented data were plotted by the computer with a straight line drawn between data points.

4.0 PRECISION OF MEASUREMENTS

4.1 TEST CONDITIONS

Uncertainties (bands which include 95 percent of the calibration data) in the basic tunnel parameters (p_o, T_o, and M_∞) were estimated from repeat calibrations of the instrumentation and from the repeatability and uniformity of the test section flow during tunnel calibration. These uncertainties were then used to estimate uncertainties in the other free-stream properties using the Taylor series method of error propagation. The uncertainties for the test conditions are:

		Uncertainty, percent						
M_∞	$Re_d \times 10^{-5}$	M_∞	p_o	T_o	q_∞	V_∞	Re	$pd/2V_\infty$
0.22[a]	1.05	±0.91	±0.20	±0.50	±1.77	±0.94	±1.12	±1.02
0.60	2.60	±0.38	±0.32	±0.20	±0.67	±0.37	±0.47	±0.54
0.60	4.17	±0.38	±0.24	±0.20	±0.63	±0.37	±0.42	±0.54
0.90	2.60	±0.34	±0.34	±0.20	±0.49	±0.31	±0.43	±0.51
0.90	4.17	±0.34	±0.29	±0.20	±0.46	±0.31	±0.39	±0.51
1.15	4.17	±0.66	±0.29	±0.20	±0.46	±0.59	±0.38	±0.71
1.30	4.17	±1.14	±0.29	±0.20	±0.40	±0.86	±0.39	±0.95
1.50	2.58	±1.30	±0.25	±0.50	±0.34	±0.95	±0.85	±1.03
1.50	4.13	±1.30	±0.20		±0.31	±0.95	±0.83	±1.03
1.76	4.13	±1.14	±0.20		±0.80	±0.75	±1.01	±0.85
2.00	2.57	±1.00	±0.21		±1.13	±0.61	±1.14	±0.73
2.00	4.10	±1.00	±0.20		±1.13	±0.61	±1.14	±0.73
2.25	4.10	±0.89	±0.20		±1.37	±0.51	±1.22	±0.65
2.49[a]	1.86	±0.80	±0.23		±1.53	±0.45	±1.31	±0.60
2.49	2.57	±0.80	±0.20		±1.52	±0.44	±1.27	±0.59
2.50	4.10	±0.80	±0.20		±1.52	±0.44	±1.27	±0.59
2.50[a]	5.97	±0.80	±0.20		±1.52	±0.44	±1.30	±0.59

[a] For the Basic Finner Model

Measurements of the model pitch attitude, including the model-balance deflections, are precise within ±0.1 deg based on repeat calibrations.

4.2 ROLL DAMPING DATA

The uncertainty in evaluating the rolling-moment coefficients is a function of the precision of the moment of inertia, roll position-time data, the errors produced from data fits, and the uncertainty in the tunnel parameters. The estimated uncertainties in the fitting of the data are obtained as a by-product of the fitting technique. The uncertainties in the roll-damping data as a result of using the Taylor series method of error propagation are listed below.

		Uncertainty			
M_∞	$Re_d \times 10^{-5}$	C_{ℓ_o}, absolute	C_{ℓ_T}[a], absolute	C_{ℓ_T}[b], percent	C_{ℓ_p}[c], percent
0.22	1.05	±0.032	±0.0140	±4.2	±4.1
0.60	2.60	---	±0.0064	±2.3	±3.2
0.60	4.17	---	±0.0040	±2.3	±2.2
0.90	2.60	---	±0.0047	±2.3	±3.7
0.90	4.17	---	±0.0030	±2.3	±2.1
1.15	4.17	---	±0.0026	±2.0	±2.2
1.30	4.17	---	±0.0025	±2.0	±2.3
1.50	2.58	---	±0.0039	±1.9	±3.2
1.50	4.13	---	±0.0024	±1.9	±2.3
1.76	4.13	---	±0.0024	±2.0	±2.3
2.00	2.57	---	±0.0040	±2.2	±3.2
2.00	4.10	---	±0.0025	±2.2	±2.4
2.25	4.10	---	±0.0026	±2.3	±2.5
2.49	1.86	±0.008	±0.0044	±2.0	±3.6
2.49	2.57	---	±0.0043	±2.4	±2.6
2.50	4.10	---	±0.0027	±2.4	±4.0
2.50	5.07	±0.008	±0.0014	±2.0	±2.6

[a] Near the minimum value

[b] Near the maximum value

[c] For linear damping only

4.3 STATIC-STABILITY DATA

The balance uncertainties listed in Section 2.3 were combined with uncertainties in the tunnel parameters, assuming a Taylor series error propagation, to estimate the precision of the aerodynamic coefficients. The uncertainties near the minimum and maximum loads are presented below.

Uncertainty near Minimum Loads

		Uncertainty, absolute						
M_∞	$Re_d \times 10^{-5}$	C_N	C_m	C_Y	C_n	C_{A_T}	C_{Y_p}[a]	C_{n_p}[a]
0.22	1.05	±0.64	±0.70	±0.08	±0.20	±0.100	±5.0	±9.0
0.60	2.60	±0.17	±0.29	±0.04	±0.07	±0.050	---	---
0.60	4.17	±0.11	±0.18	±0.02	±0.04	±0.030	---	---
0.90	2.60	±0.13	±0.22	±0.03	±0.05	±0.030	±0.5	±1.5
0.90	4.17	±0.08	±0.13	±0.02	±0.03	±0.020	±0.3	±1.0
1.15	4.17	±0.07	±0.12	±0.02	±0.03	±0.020	±0.3	±1.0
1.30	4.17	±0.07	±0.11	±0.01	±0.03	±0.020	±0.2	±1.0
1.50	2.58	±0.06	±0.11	±0.02	±0.04	±0.012	±0.5	±2.0
1.50	4.13	±0.04	±0.07	±0.01	±0.02	±0.008	±0.3	±1.5
1.76	4.13	±0.04	±0.07	±0.01	±0.02	±0.008	±0.3	±1.5
2.00	2.57	±0.06	±0.11	±0.02	±0.04	±0.013	±0.3	±1.5
2.00	4.10	±0.04	±0.08	±0.01	±0.03	±0.008	±0.2	±1.0
2.25	4.10	±0.04	±0.08	±0.02	±0.03	±0.008	±0.2	±1.0
2.49	1.86	±0.09	±0.12	±0.03	±0.04	±0.016	±0.5	±1.0
2.49	2.57	±0.07	±0.14	±0.03	±0.05	±0.014	±0.3	±1.2
2.50	4.10	±0.04	±0.09	±0.02	±0.03	±0.009	±0.2	±1.0
2.50	5.97	±0.03	±0.04	±0.02	±0.03	±0.005	±0.5	±1.0

[a] Uncertainties based on data repeatability

Uncertainty near Maximum Loads

M_∞	$Re_d \times 10^{-5}$	Uncertainty, percent				
		C_N	C_m	C_Y	C_n	C_{A_T}
0.22	1.05	±4.4	±9.4	±3.7	±4.9	±20.0
0.60	2.60	±1.3	±2.0	±3.9	±4.6	±22.8
0.60	4.17	±0.9	±1.3	±2.4	±2.9	±14.2
0.90	2.60	±1.0	±1.5	±2.9	±2.6	±16.9
0.90	4.17	±0.7	±1.0	±2.3	±1.8	±10.5
1.15	4.17	±0.6	±0.9	±5.1	±1.9	± 3.7
1.30	4.17	±0.6	±0.8	±4.8	±1.8	± 3.5
1.50	2.58	±0.6	±1.2	±9.3	±3.6	± 2.3
1.50	4.13	±0.4	±0.8	±6.0	±2.2	± 1.4
1.76	4.13	±0.8	±0.9	±6.0	±2.3	± 1.7
2.00	2.57	±1.2	±1.3	±9.1	±3.8	± 2.8
2.00	4.10	±1.1	±1.2	±6.2	±3.0	± 1.9
2.25	4.10	±1.4	±1.5	±6.5	±3.2	± 2.1
2.49	1.86	±1.6	±1.9	±6.0	±3.0	± 3.4
2.49	2.57	±1.6	±1.7	±9.5	±5.1	± 3.1
2.50	4.10	±1.5	±1.6	±6.8	±3.4	± 2.3
2.50	5.97	±1.5	±1.6	±2.9	±2.0	± 1.7

It should be noted that the data repeatability, which is a measure of the random errors, was generally well within the maximum propagated uncertainties quoted.

5.0 RESULTS AND DISCUSSION

The current tests were conducted primarily to verify that the new high-alpha missile roll-damping test mechanism could be used to obtain roll-damping data and to obtain roll-damping, Magnus, and static-stability data on a typical missile configuration. Data were obtained at Mach numbers from 0.22 through 2.50 for angles of attack from -5 to 90 deg and spin rates up to 1,250 radians/sec.

The variations of the total rolling-moment coefficient ($C\ell_T$) with spin rate for the Basic Finner Model are presented in Fig. 8. At Mach number 0.22 (Fig. 8a), the variation of $C\ell_T$ is a linear function of roll rate only at small angles of attack ($\alpha < 20$ deg). At the higher angles of attack, the variations are very nonlinear, and as a result, $C\ell_p = \partial C\ell_T/\partial(pd/2V_\infty)$ varies with $pd/2V_\infty$ and cannot be used in the traditional manner. Therefore, in this report, values of $C\ell_p$ will only be presented for linear or nearly linear damping. At Mach number 2.5 (Figs. 8b and c), the variation of $C\ell_T$ was linear for both spin-up and spin-down cases at all angles of attack.

The roll-damping characteristics of the Basic Finner Model at $M_\infty = 0.22$ and 2.50 are presented in Fig. 9 as a function of angle of attack. At $M_\infty = 0.22$, the damping was nonlinear for $\alpha > 17.5$ deg, and the agreement of the linear data with results obtained by Regan (Ref. 2) was good. The model exhibited an autorotation characteristic at the high angles of attack. At $\alpha \approx 75$ deg, the steady-state spin rate was nearly double the steady-state spin rate at $\alpha = 0$. The results presented in Fig. 9b for $M_\infty = 2.5$ show that

there is excellent agreement in $C\ell_p$ values for the spin-up data (δ = 2.5 deg) and the spin-down data (δ = 0). It should be noted that the two sets of data were recorded during different tunnel test entries, thereby indicating good data repeatability. There is also fair agreement with the test results obtained by Regan for $\alpha < 15$ deg.

The effects of the support system and of Reynolds number on $C\ell_p$ at $M_\infty = 2.5$ for the Basic Finner Model are shown in Fig. 9c. The results obtained with the high-alpha missile roll-damping test mechanism (Fig. 4a) are in excellent agreement with those obtained with a straight sting (Fig. 4b) with and without the spin jet tubes. The results also show that there is no Reynolds number effect on $C\ell_p$ for the two Reynolds numbers tested.

The variations of the total rolling-moment coefficient ($C\ell_T$) with spin rate for the Modified Basic Finner are presented in Fig. 10. Although data were generally obtained every 2.5 deg, the results are only presented for approximately every 10 deg for the sake of clarity. The results show that $C\ell_T$ is very nonlinear at the lower Mach numbers ($M_\infty \leq 0.9$) and that some nonlinearities even exist at the supersonic Mach numbers ($M_\infty \leq 1.5$). In addition, at $M_\infty \leq 0.9$, the value of $C\ell_T$ is zero at spin rates other than p = 0. Therefore, the model will autorotate at these conditions. Figure 11 presents the spin rates at which the model (corrected for bearing moments) would autorotate. At M_∞ = 0.6, the model began to autorotate at $\alpha \approx 45$ deg and reached a maximum value ($pd/2V_\infty$ = 0.095, p ≈ 840 radians/sec) at α = 90 deg. At M_∞ = 0.9, the autorotation started at $\alpha \approx 58$ deg, reached a maximum value ($pd/2V_\infty$ = 0.026, p ≈ 340 radians/sec) at α = 63 deg, and did not autorotate above α = 78 deg.

The variations of $C\ell_p$ with angle of attack for the Modified Basic Finner Model are presented in Fig. 12. As noted before, only the results for linear damping are presented with the exception of slightly nonlinear values at lower angles of attack ($\alpha < 30$ deg). The results show that as the Mach number increases, the range of angles of attack for which the damping is linear also increases. The dashed line fairing indicates regions of nonlinear damping as well as the general indicated data trend. The effects of Reynolds number are generally small with the largest effects occurring for $\alpha < 30$ deg at M_∞ = 1.5 and 2.0.

The approximate regions of nonlinear damping for the Modified Basic Finner Model is indicated in Fig. 13. The figure shows that nonlinear damping occurs at low Mach numbers ($M_\infty \lesssim 1.5$) and high angles of attack ($\alpha \gtrsim 17$ deg). It was found that very nonlinear damping occurred at the subsonic Mach numbers ($M_\infty < 1.0$) and $\alpha > 30$ deg. The indicated regions could vary considerably with Reynolds number and spin-rate range. It would also be expected that model geometry would have a strong influence.

Although the mechanism was designed primarily to obtain roll damping data, the system records the forces and moments acting on the model as the spin rate varies. Figures 14 through 17 present the Magnus force (side force) and Magnus moment (yawing moment) characteristics of the Basic Finner Model. The magnitude of both C_Y and C_n increase with spin rate at $M_\infty = 2.5$ (Fig. 14b) in the typical manner. The maximum values were obtained at approximately 40-deg angle of attack. At $M_\infty = 0.22$, the variations with spin rate are clearly shown; however, at some of the angles ($\alpha \approx 60$ deg), large values of C_Y and C_n are indicated at zero spin rate. These forces are probably the result of the unsteady asymmetric vortex system which was discussed by Gowen and Perkins (Ref. 3).

The Magnus force and moment spin derivative coefficients of the Basic Finner Model are presented in Fig. 15 as a function of angle of attack. At $M_\infty = 0.22$, there are erratic variations in the data for $\alpha > 30$ deg. Two items that could contribute to these variations are the relatively small range of spin rates, which results in only short segment of data being fitted (see Fig. 14a), and the unsteady vortex system. Although there are erratic variations, the data show a definite trend in the magnitude of both C_{Y_p} and C_{n_p} as the angle of attack increases. The maximum values of both C_{Y_p} and C_{n_p} occurred at $\alpha \approx 50$ deg. At $M_\infty = 2.5$, the variations of C_{Y_p} and C_{n_p} with α are very smooth, and the agreement of the values obtained from the spin-down data with the values obtained from the spin-up data was excellent. It should be noted that the signs of both parameters changed as the Mach number increased from 0.22 to 2.50. The effects of the support system and of Reynolds number are presented in Fig. 15c. The results show that there was no effect produced by the high-alpha missile roll-damping test mechanism strut or by the spin-jet tubes. Increasing the Reynolds number increased the magnitude of both parameters at $\alpha > 10$ deg.

The variations of C_Y and C_n with spin rate for the Modified Basic Finner Model are presented in Fig. 16. For $M_\infty \leq 1.5$, the values and trends of C_Y and C_n change abruptly with changes in angle of attack, indicating the strong influence of the vortex system. At $M_\infty > 1.5$, the trends are systematic and both C_Y and C_n approach zero as the spin rate approaches zero.

The values of C_{Y_p} and C_{n_p} for the Modified Basic Finner Model presented in Fig. 17 clearly show the large variations in the Magnus parameters with angle of attack. For $M_\infty \leq 1.3$, both C_{Y_p} and C_{n_p} may change signs several times as the angle of attack increases from 0 to 90 deg. The values of C_{Y_p} and C_{n_p} at M_∞ 0.6 could not be computed because of the model autorotation. Increasing the Reynolds number generally increased the magnitude of both parameters.

The static longitudinal and directional stability and axial-force characteristics of both models rotating at a spin rate of approximately 100 radians/sec (33 radians/sec at M_∞ = 0.22, Fig. 19a) are presented in Figs. 18 through 23. For both models, there was no effect of Reynolds number on the stability characteristics and only small effects on the axial force. The results for the Basic Finner Model (Figs. 18 and 19) indicate no effect of the support strut, and there is excellent agreement of the spin-down and spin-up results with those obtained by Shantz and Groves (Ref. 4). As mentioned before, large C_Y and C_n values are indicated for zero spin rate at the lower Mach numbers. The values of C_Y and C_n at spin rates of 33 radians/sec (M_∞ = 0.22) and 100 radians/sec ($M_\infty \geq 0.6$) are shown for the Basic Finner Model in Fig. 19a and for the Modified Basic Finner Model in Fig. 22. For these spin rates, the Magnus forces are small and the values should be representative of values occurring at p = 0. The results show that large and abrupt changes in both C_Y and C_n occur with small changes in angle of attack for $M_\infty \leq 1.5$. The axial-force characteristics (Figs. 20a and 23) for both models are negative at large angles of attack and subsonic Mach numbers. No base pressures could be recorded, but it is suspected that high base pressures are responsible for the negative values.

6.0 CONCLUSIONS

Wind tunnel tests were conducted with a newly developed high-alpha missile roll-damping test mechanism. Data were obtained on two missile configurations from M_∞ = 0.22 through 2.5 for angles of attack from -5 to 90 deg and Reynolds numbers, based on model diameter, of 1 x 10^5 through 6 x 10^5. Conclusions based on the test results are given below:

1. The roll-damping characteristics vary considerably with Mach number and angle of attack.

2. The rolling moment is generally nonlinear with spin rate at large angles of attack ($\alpha > 20$ deg) and low Mach numbers ($M_\infty \lesssim 1.5$).

3. Roll-damping characteristics of the Basic Finner Model obtained in these tests (both spin up and spin down) are in agreement with existing data.

4. The Modified Basic Finner Model, with zero canted fins, autorotated (spin rates up to 840 radians/sec) at subsonic Mach numbers (M_∞ = 0.6 and 0.9) and high angles of attack ($\alpha > 45$ deg).

5. There was no effect produced by the test mechanism strut or the spin-jet tubes on the test results at M_∞ = 2.5.

6. The Magnus force and moment characteristics are very nonlinear with spin rate for $M_\infty < 1.76$.

The results obtained in this study indicate the potential problem of maintaining roll control of a missile of this type if its trajectory includes high-alpha maneuvers which take place at the lower Mach numbers. The presence of the large side loads would also be a potential problem. The nonlinearity of the rolling moment means that the data cannot be used in the normal manner in trajectory programs and that current preliminary design trajectories being computed without these parameters could have gross errors.

REFERENCES

1. Chapman, Gary T. and Kirk, Don B. "A New Method for Extracting Aerodynamic Coefficients from Free-Flight Data." AIAA Journal, Vol. 8, No. 4, April 1970.

2. Regan, F. J. "Roll-Damping Moment Measurements for the Basic Finner at Subsonic and Supersonic Speeds." NAVORD Report 6652, June 1964.

3. Gowen, Forrest E. and Perkins, Edward W. "A Study of the Effects of Body Shape on the Vortex Wakes of Inclined Bodies at a Mach Number of 2." NACA RM A 53 I 17, December 1953.

4. Shantz, Irving and Groves, Robert T. "Dynamic and Static Stability Measurements of the Basic Finner at Supersonic Speeds." NAVORD Report 4516, January 1960.

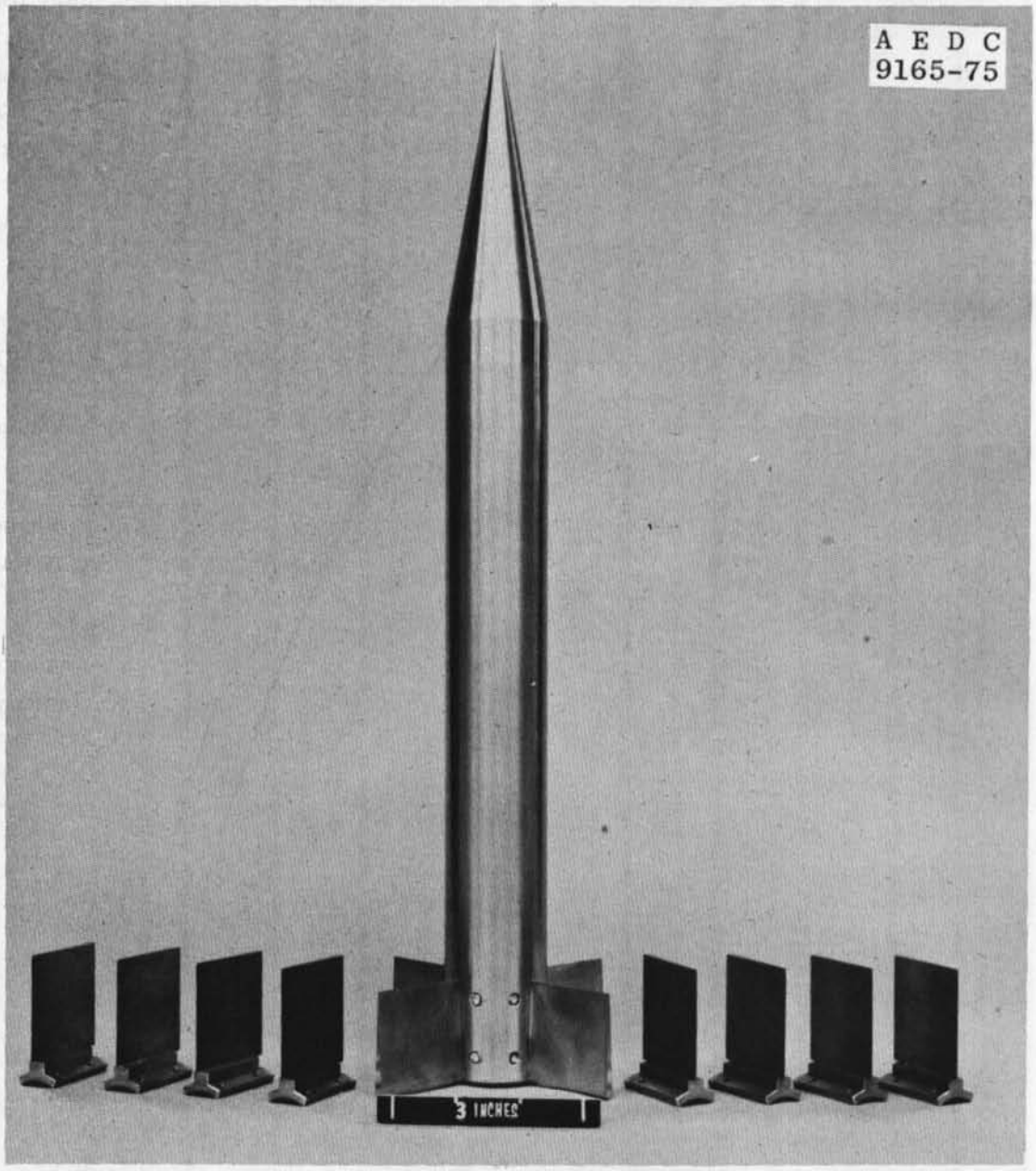

a. Basic Finner Model

Figure 1. Model photographs.

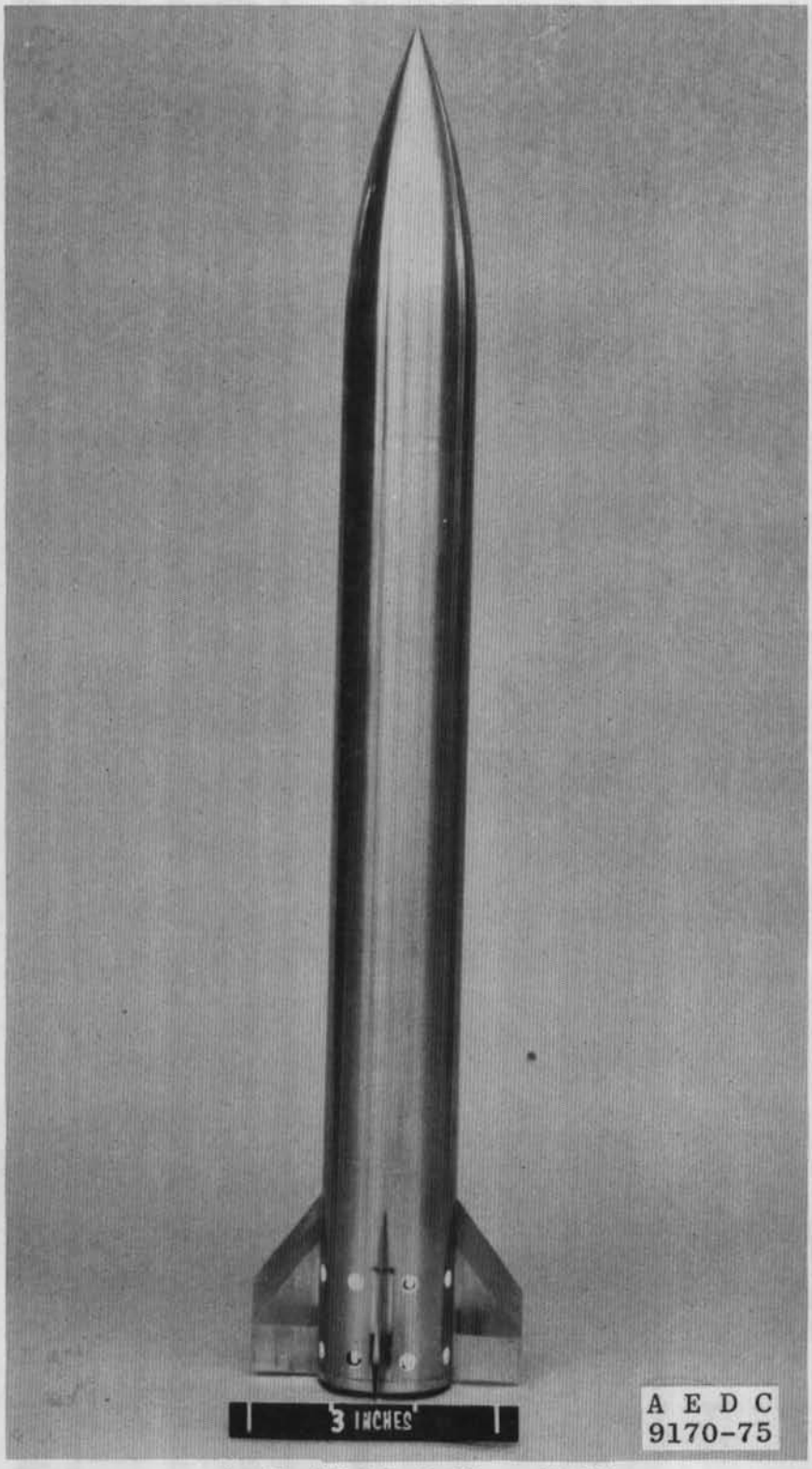

b. Modified Basic Finner Model
Figure 1. Concluded.

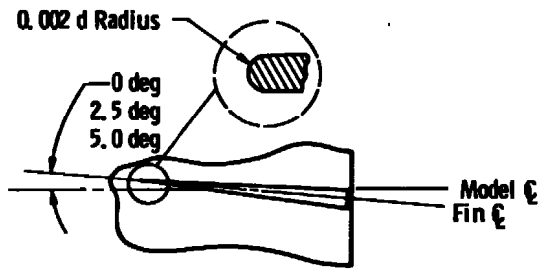

Fin Details - Basic Finner

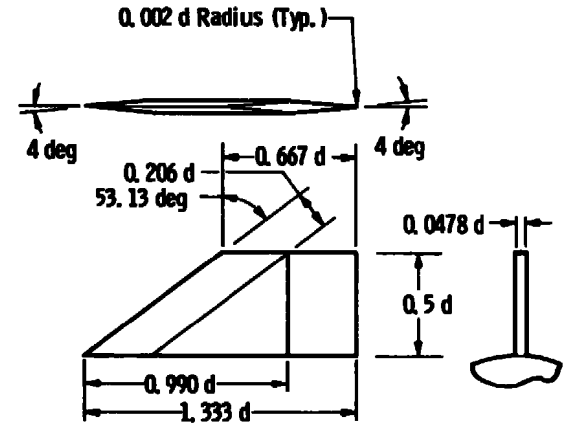

Fin Details - Modified Basic Finner

Note: 1. d = 1.8 Inches
2. All Dimensions in Calibers
3. For the Basic Finner Model, I_X = 0.00098 slugs-ft^2, X_p = 6.1 d
4. For the Modified Basic Finner Model, I_X = 0.00090 slugs-ft^2, X_p = 5 d

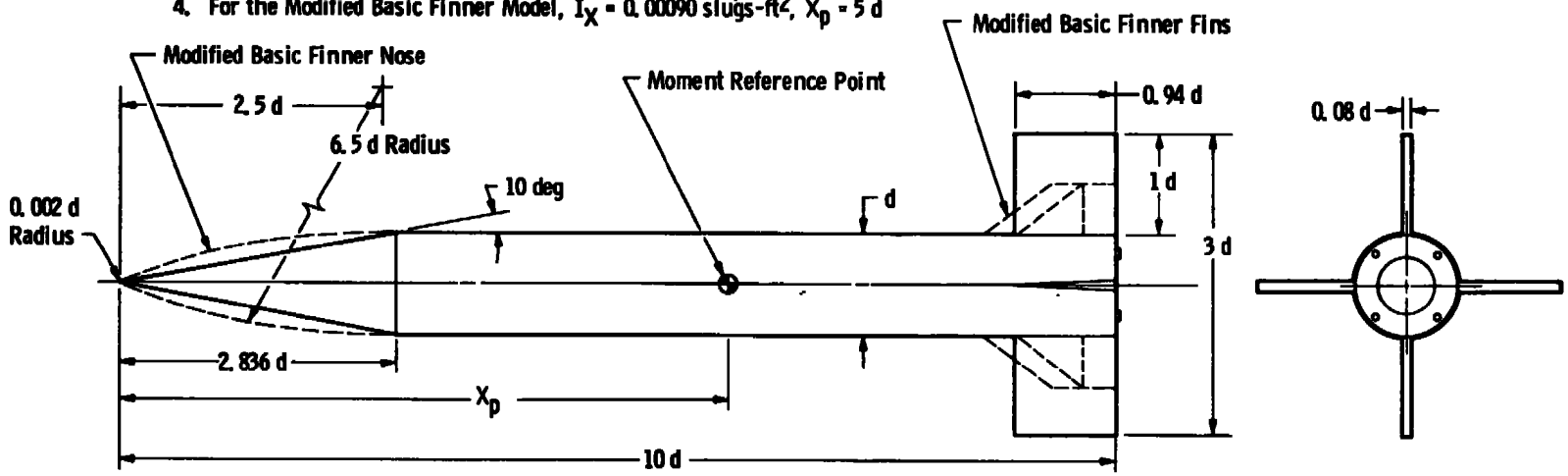

Figure 2. Model details.

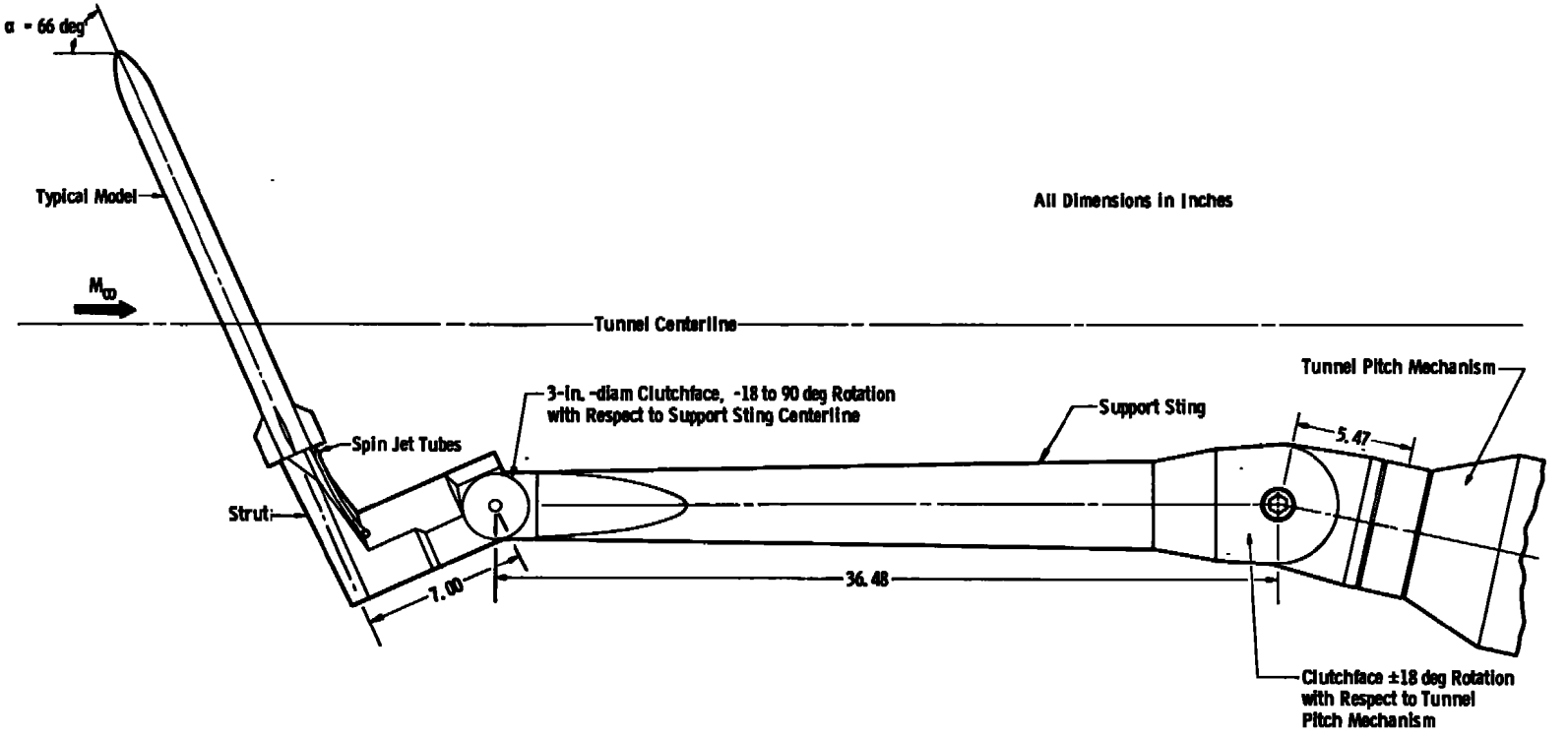

a. Installation sketch

Figure 3. High-alpha missile roll-damping test mechanism.

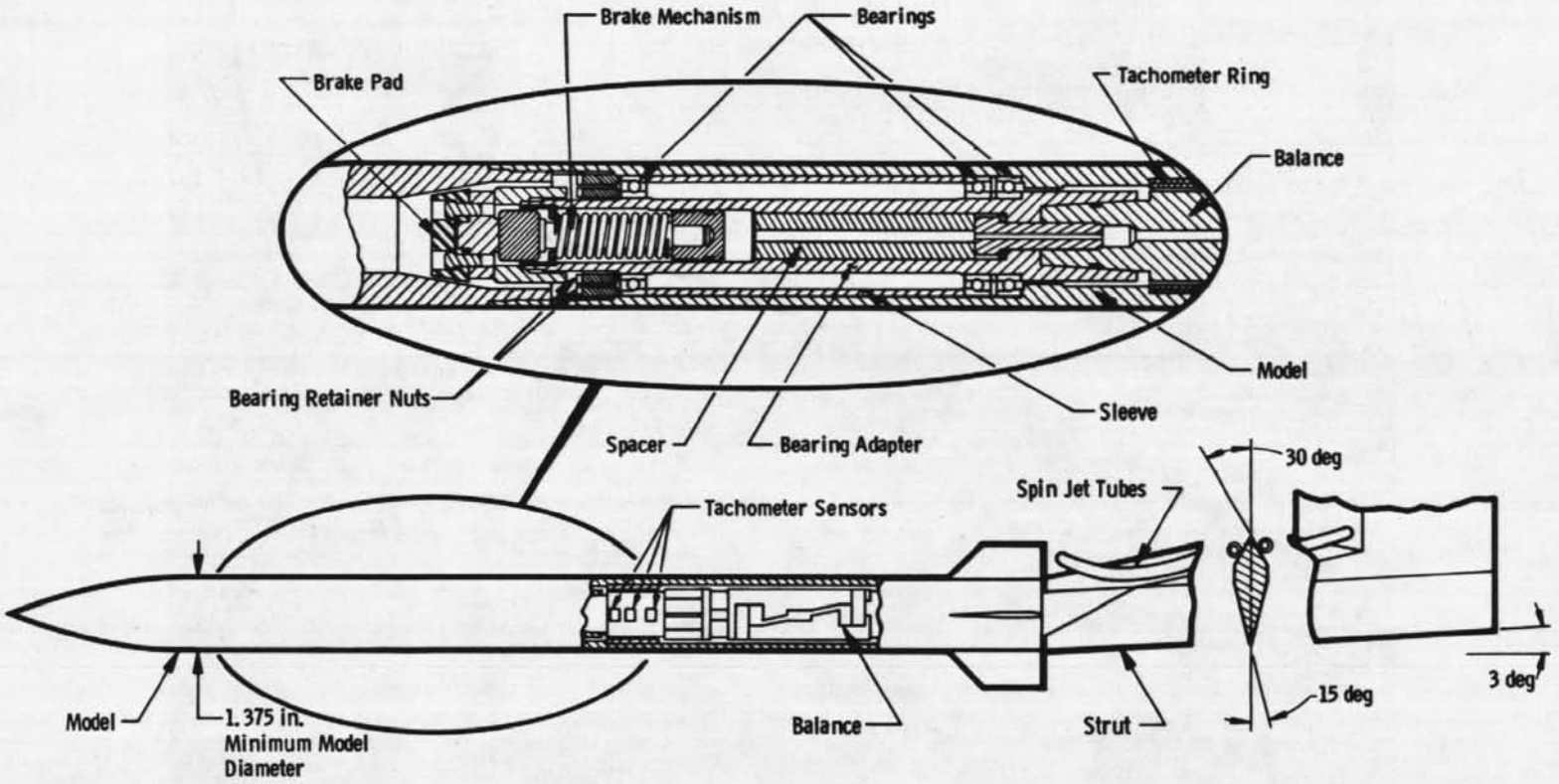

b. Mechanism details

Figure 3. Concluded.

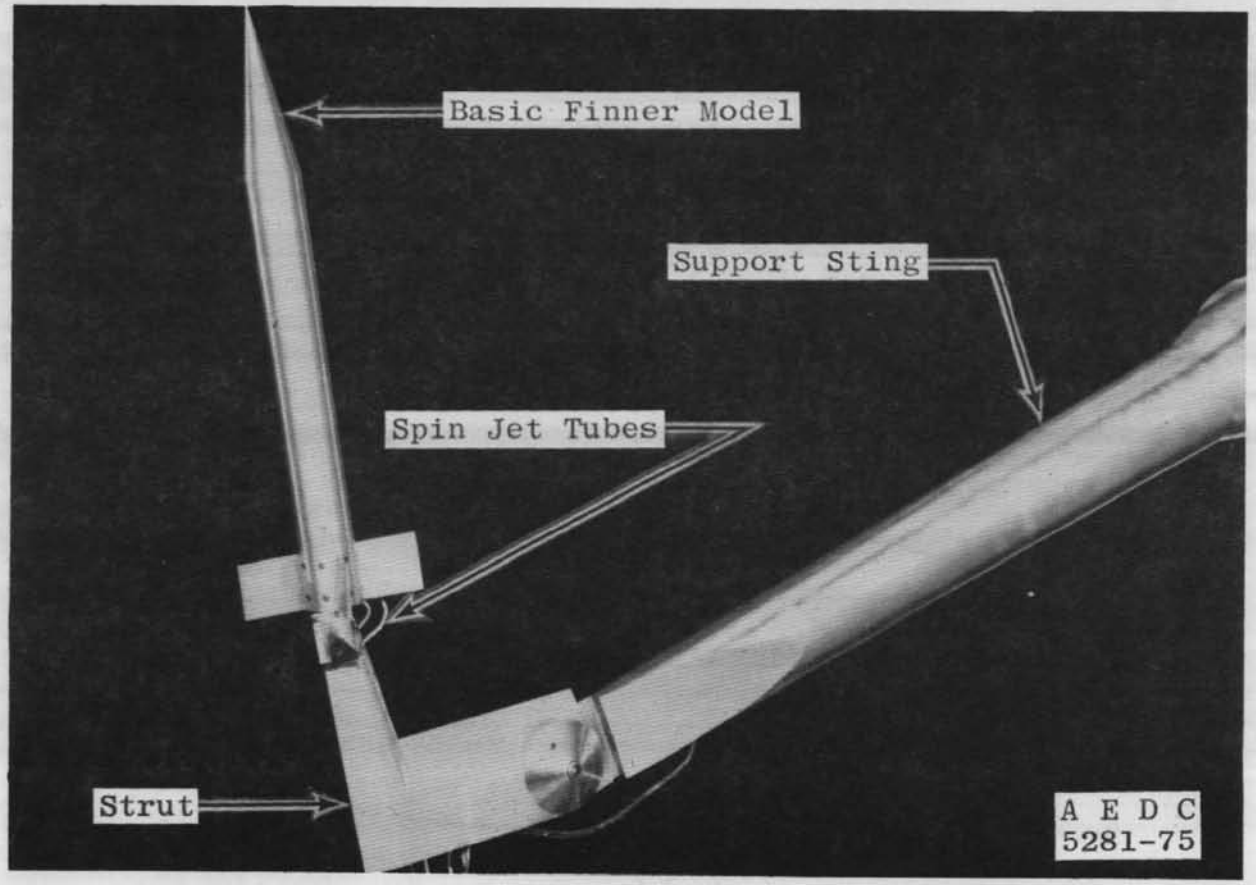

a. Tunnel A installation, high-alpha missile roll-damping test mechanism

Figure 4. Photographs of the test mechanism.

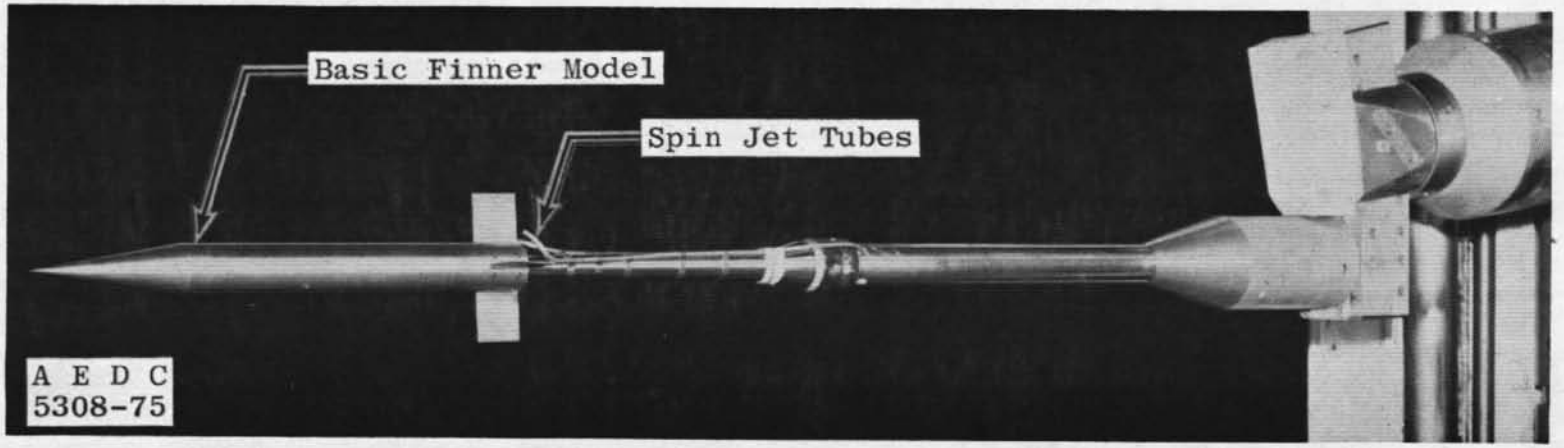

b. Tunnel A installation, straight sting
Figure 4. Continued.

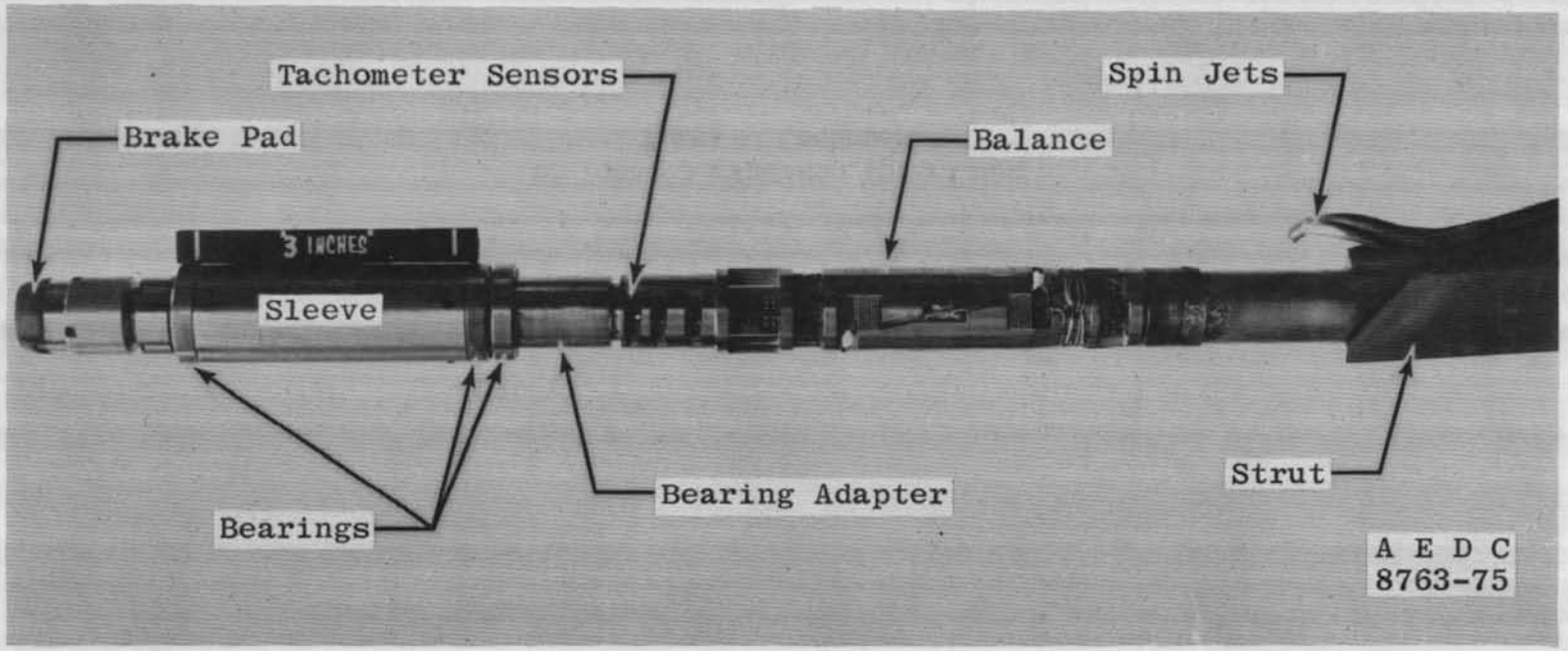

c. Mechanism with model removed
Figure 4. Continued.

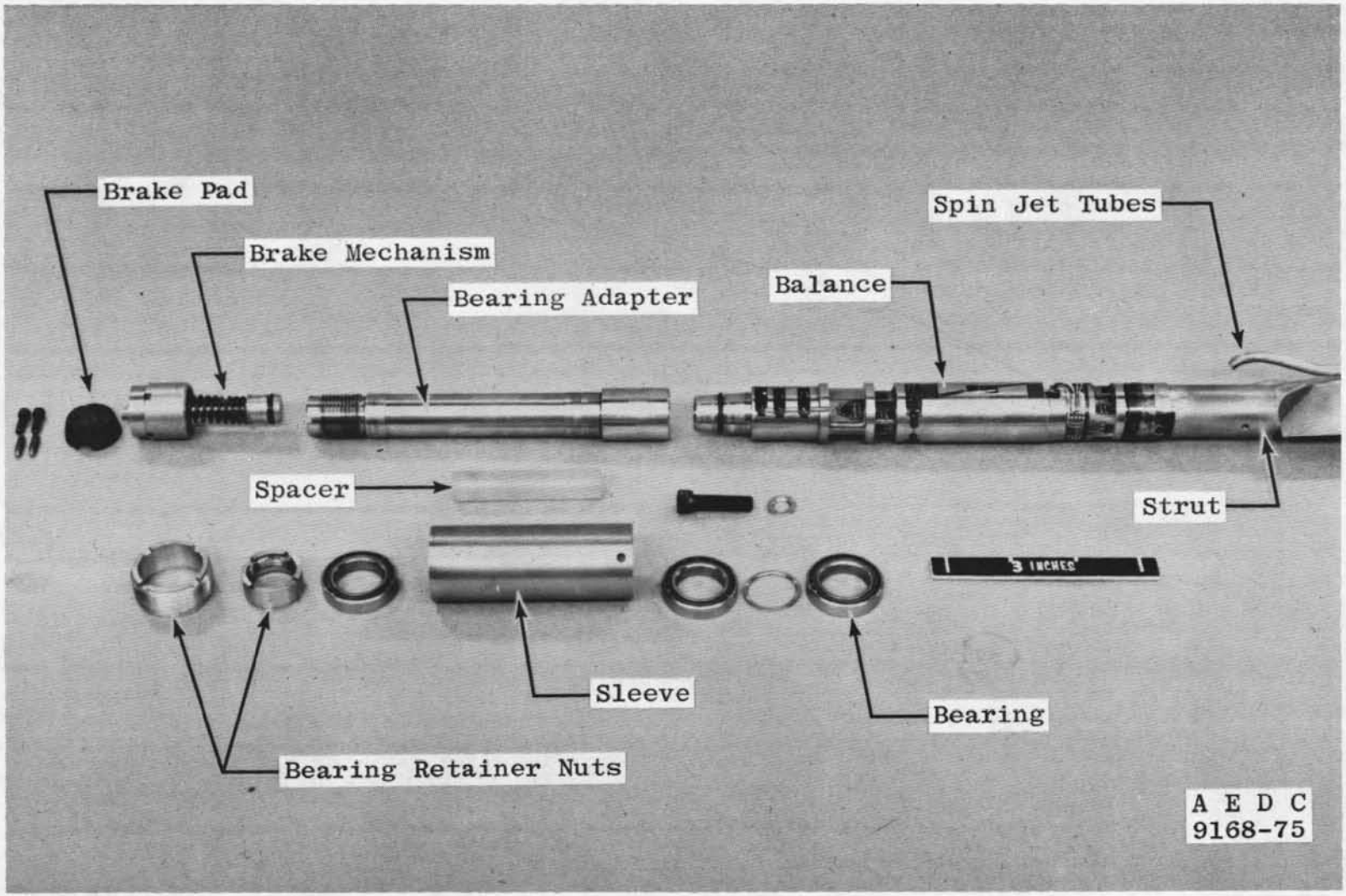

d. Mechanism disassembled
Figure 4. Continued.

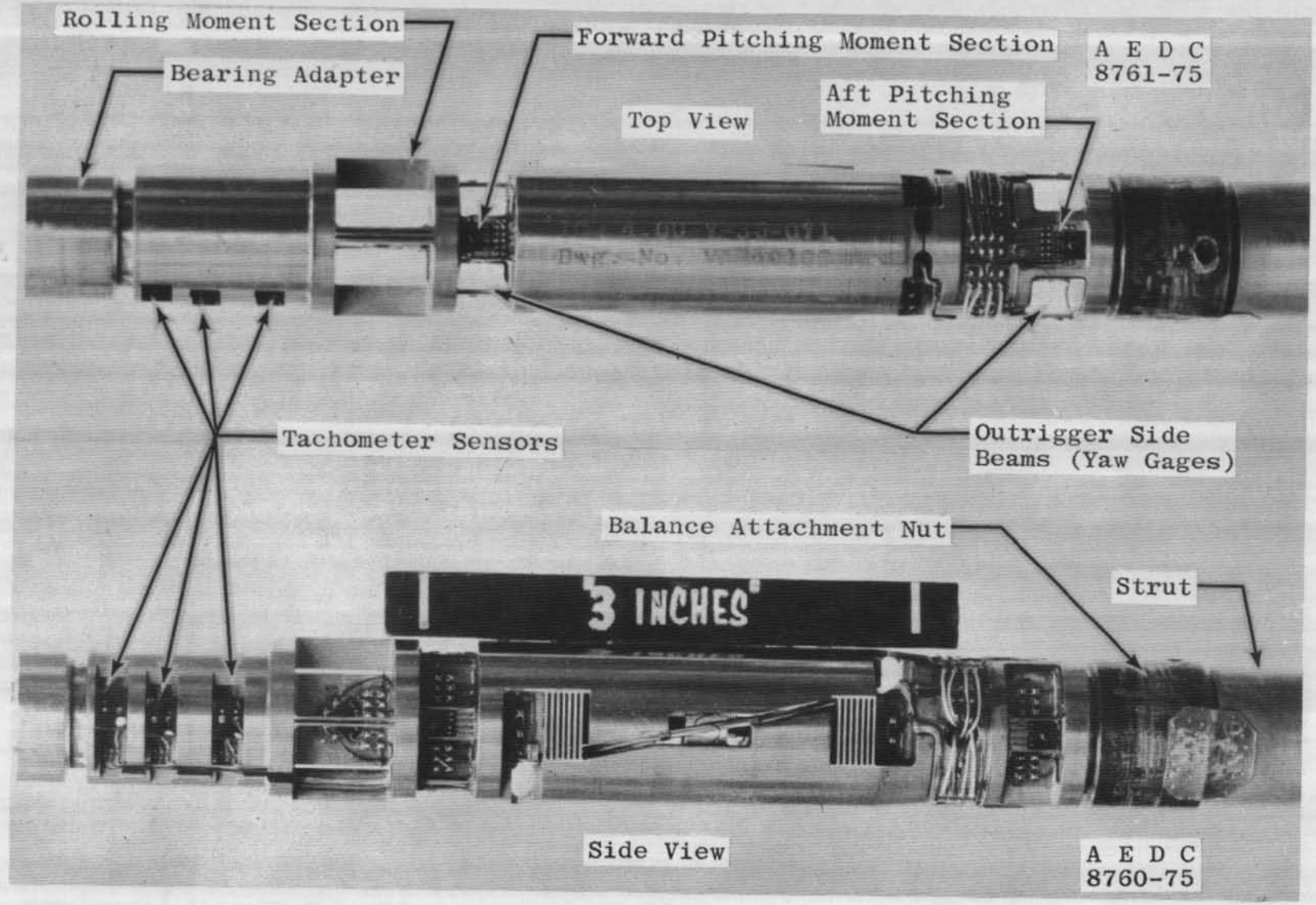

e. Balance

Figure 4. Concluded.

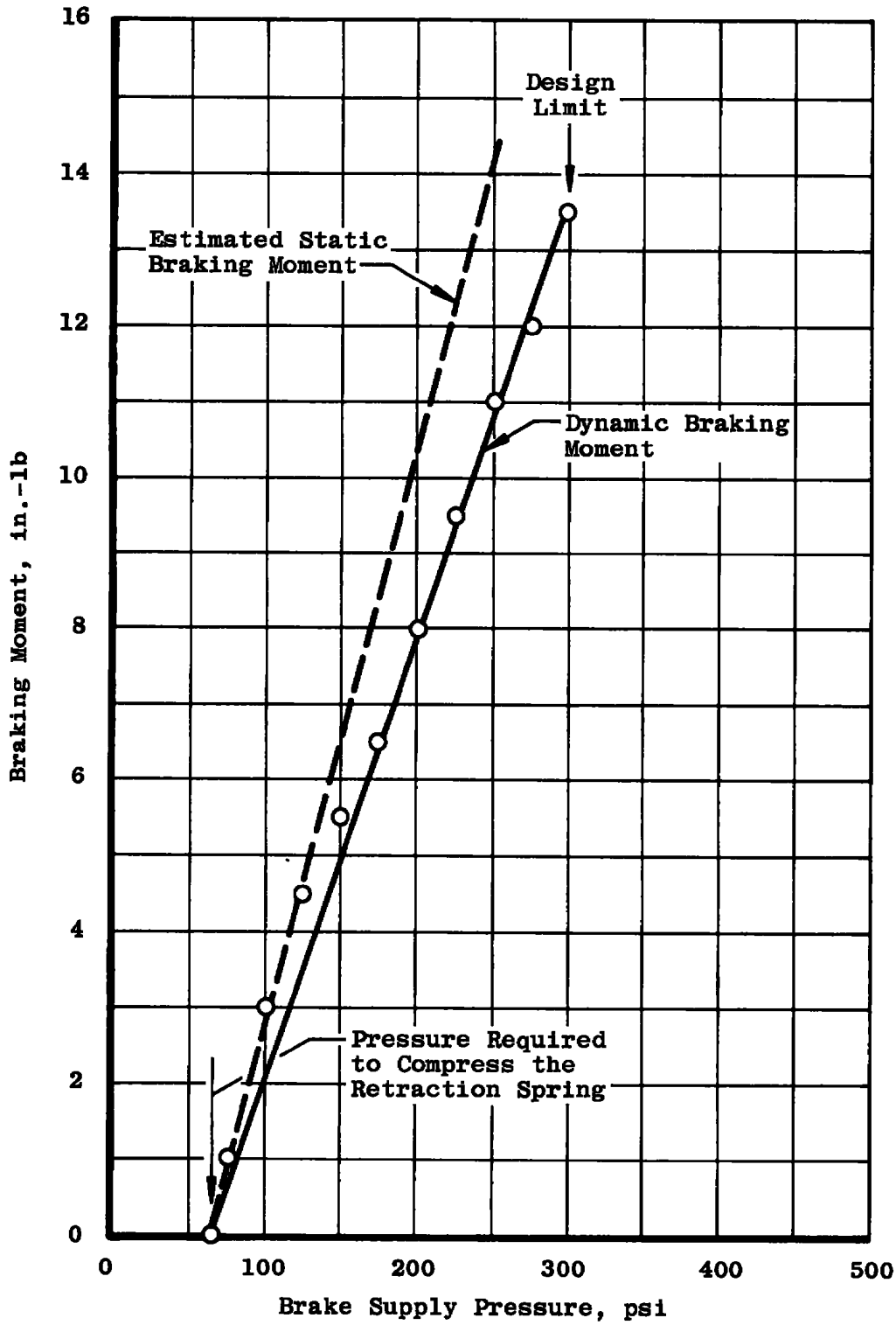

Figure 5. Brake calibration.

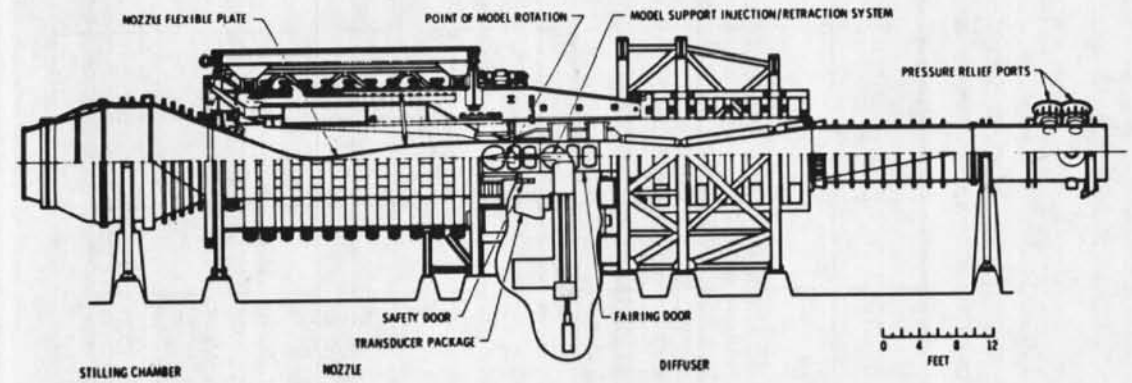

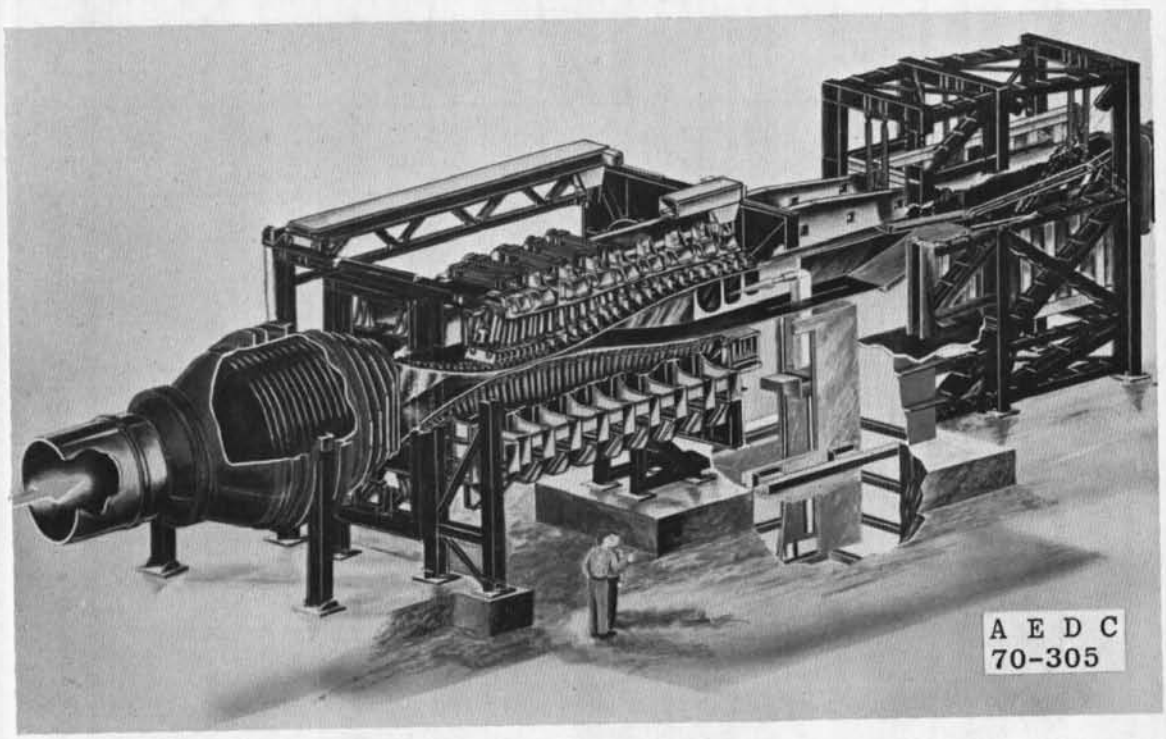

a. Tunnel A

Figure 6. Test facilities.

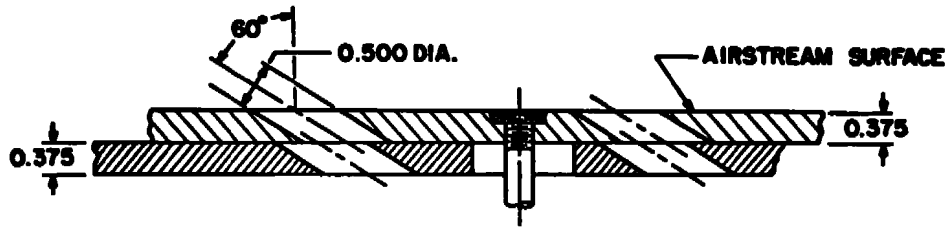

TYPICAL PERFORATED WALL CROSS SECTION

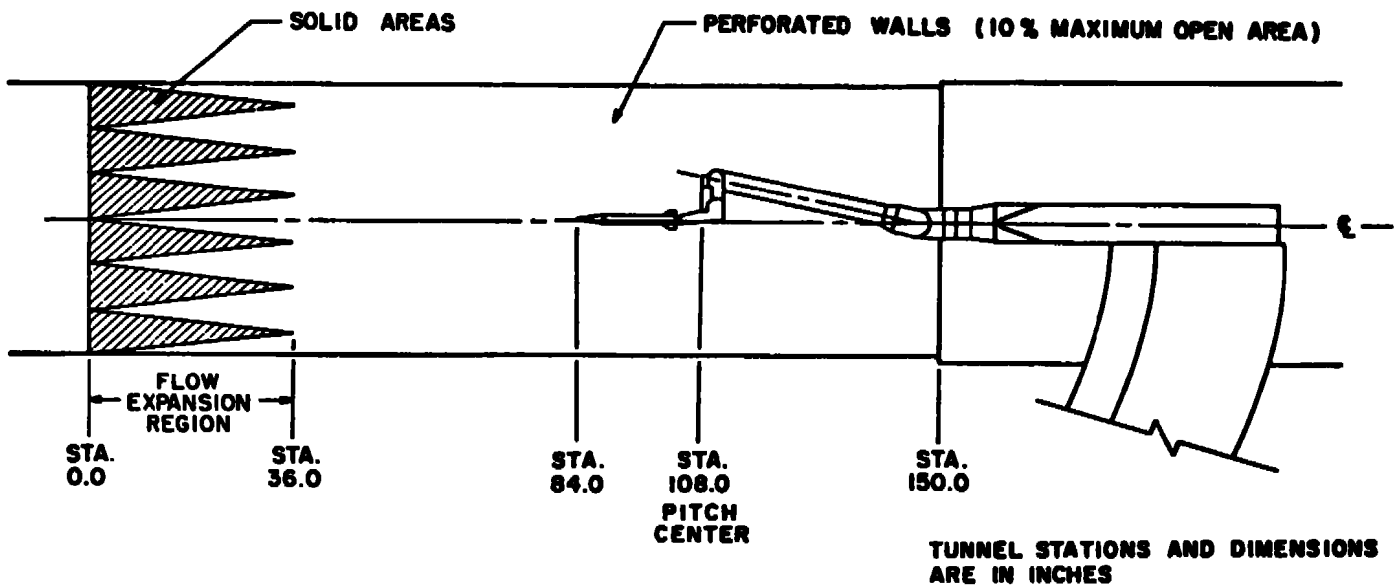

UNCLASSIFIED

b. Tunnel 4T

Figure 6. Concluded.

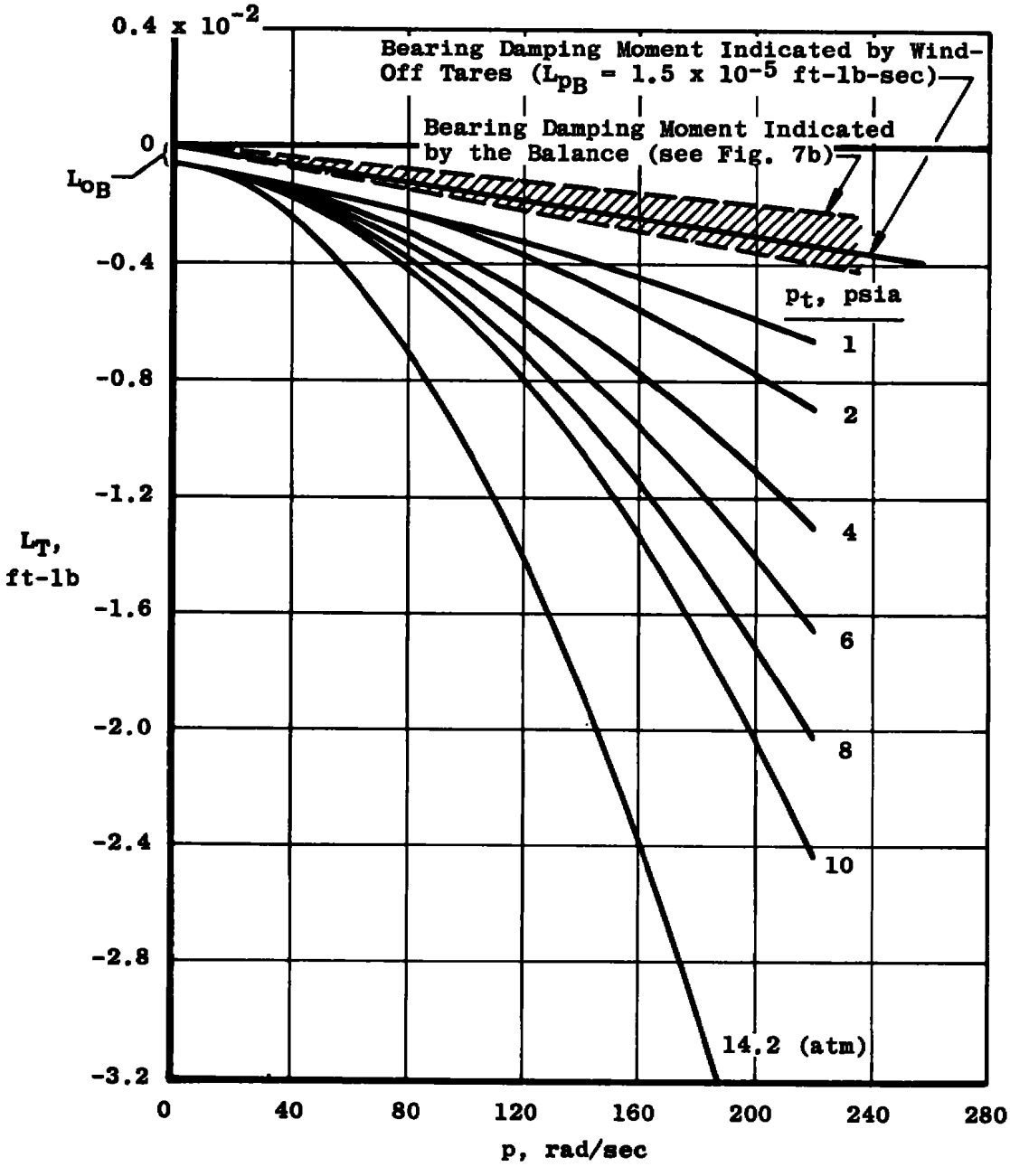

a. Model-bearing system total rolling moment

Figure 7. Bearing rolling-moment contributions.

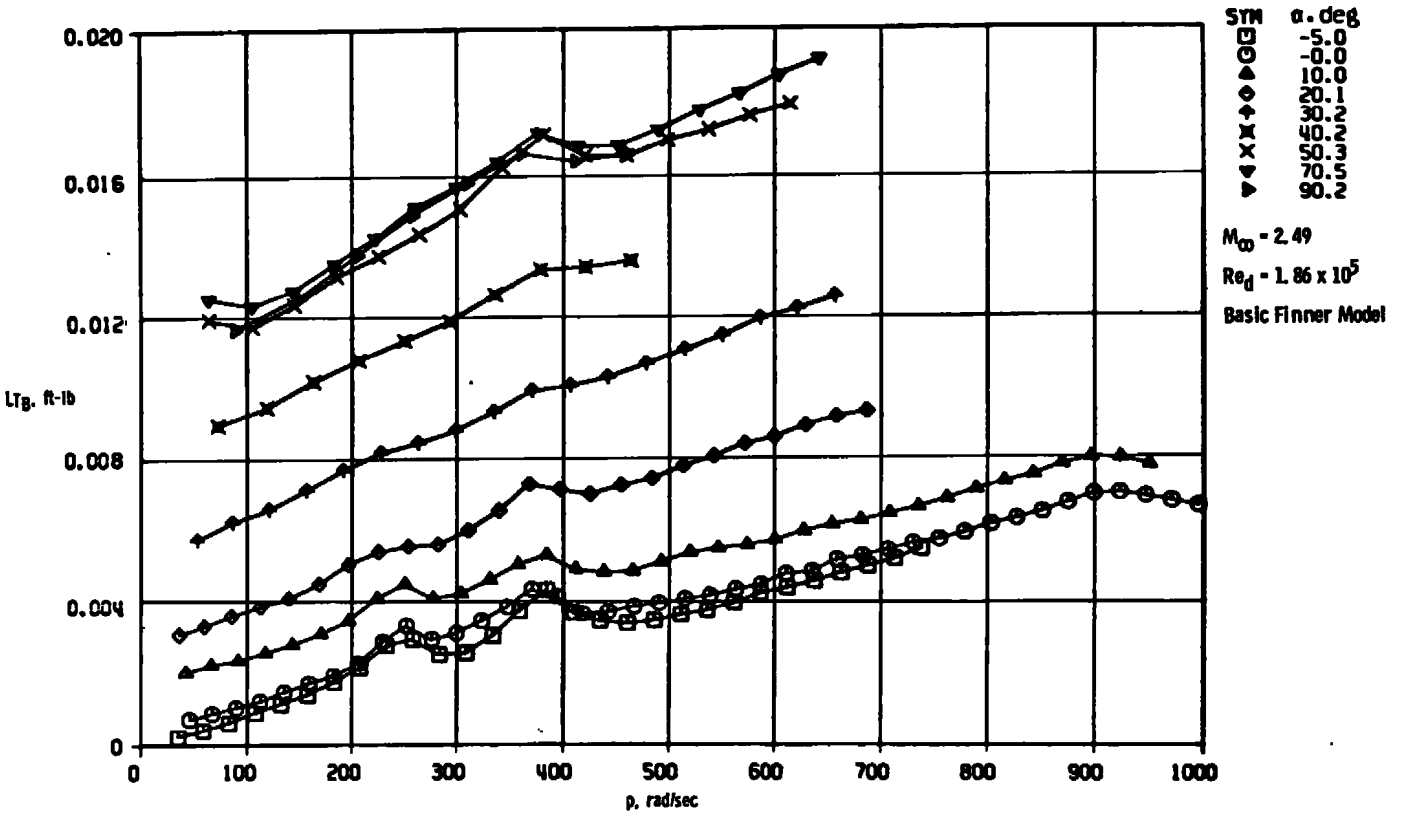

b. Total-bearing moment measured by the balance
Figure 7. Continued.

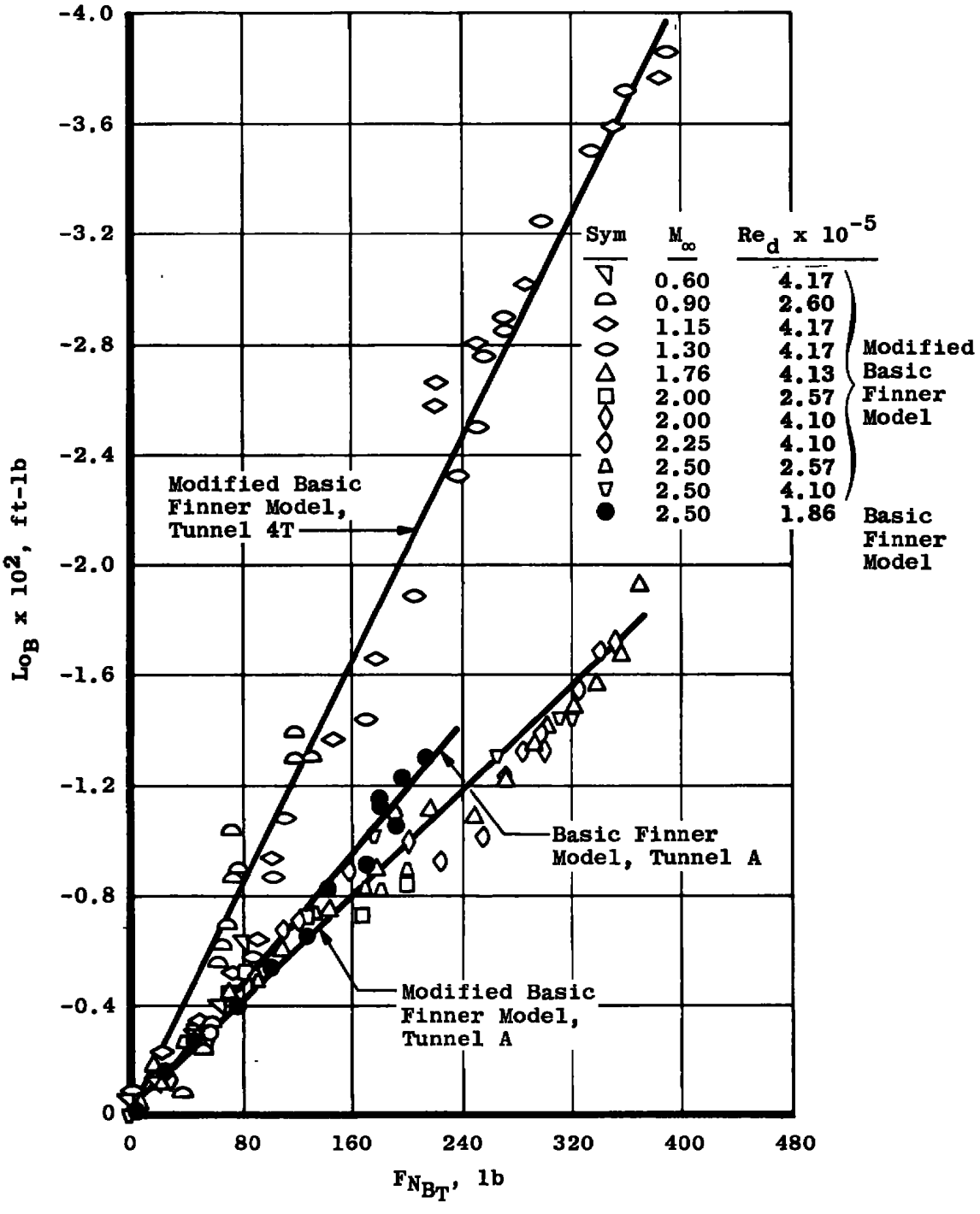

c. Variation of bearing static rolling moment with load
Figure 7. Concluded.

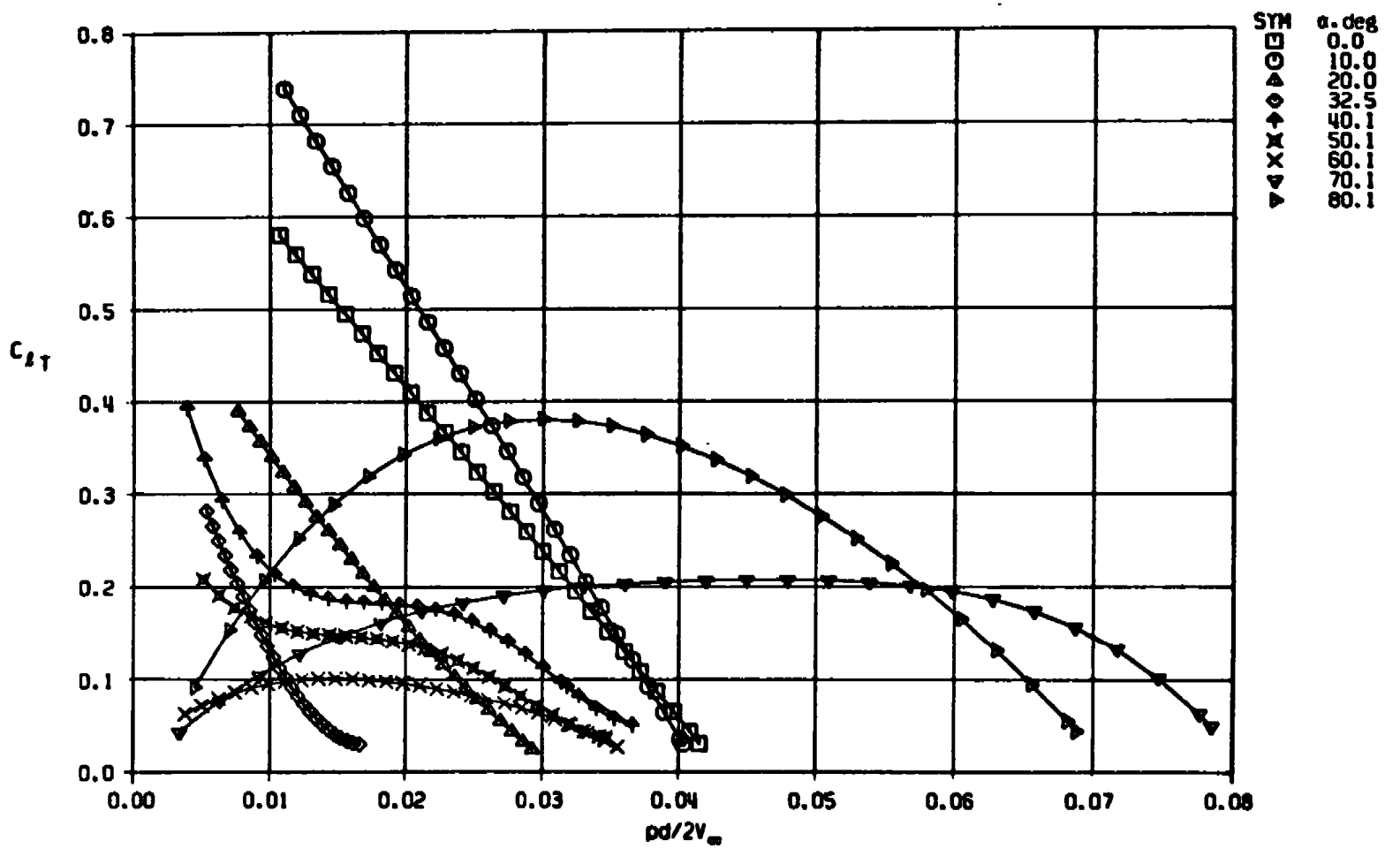

a. $M_\infty = 0.22$, spin up with $\delta = 5$ deg

Figure 8. Variation of $C\ell_T$ with spin rate for the Basic Finner Model.

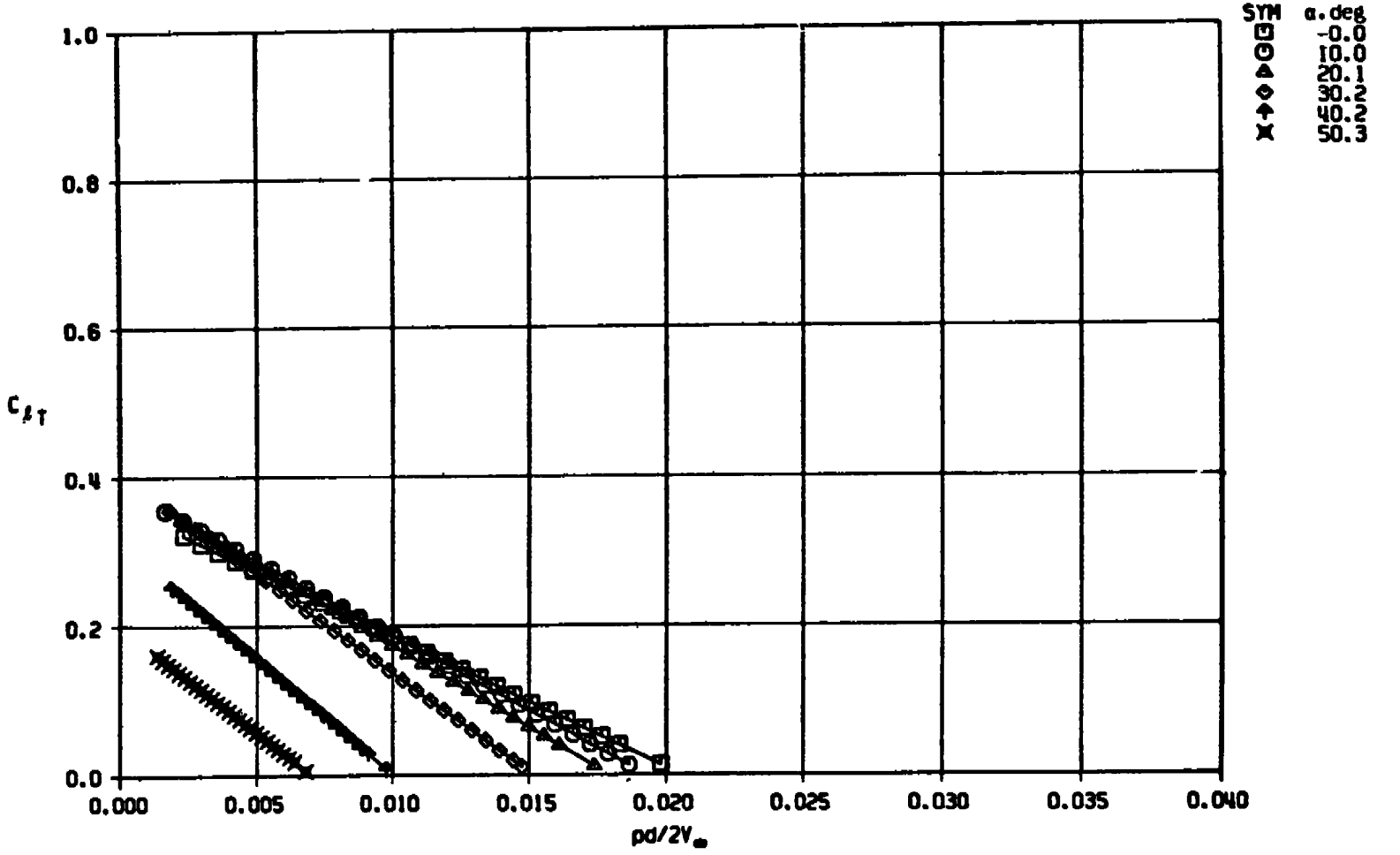

b. $M_\infty = 2.50$, $Re_d = 1.86 \times 10^5$, spin up with $\delta = 2.5$ deg

Figure 8. Continued.

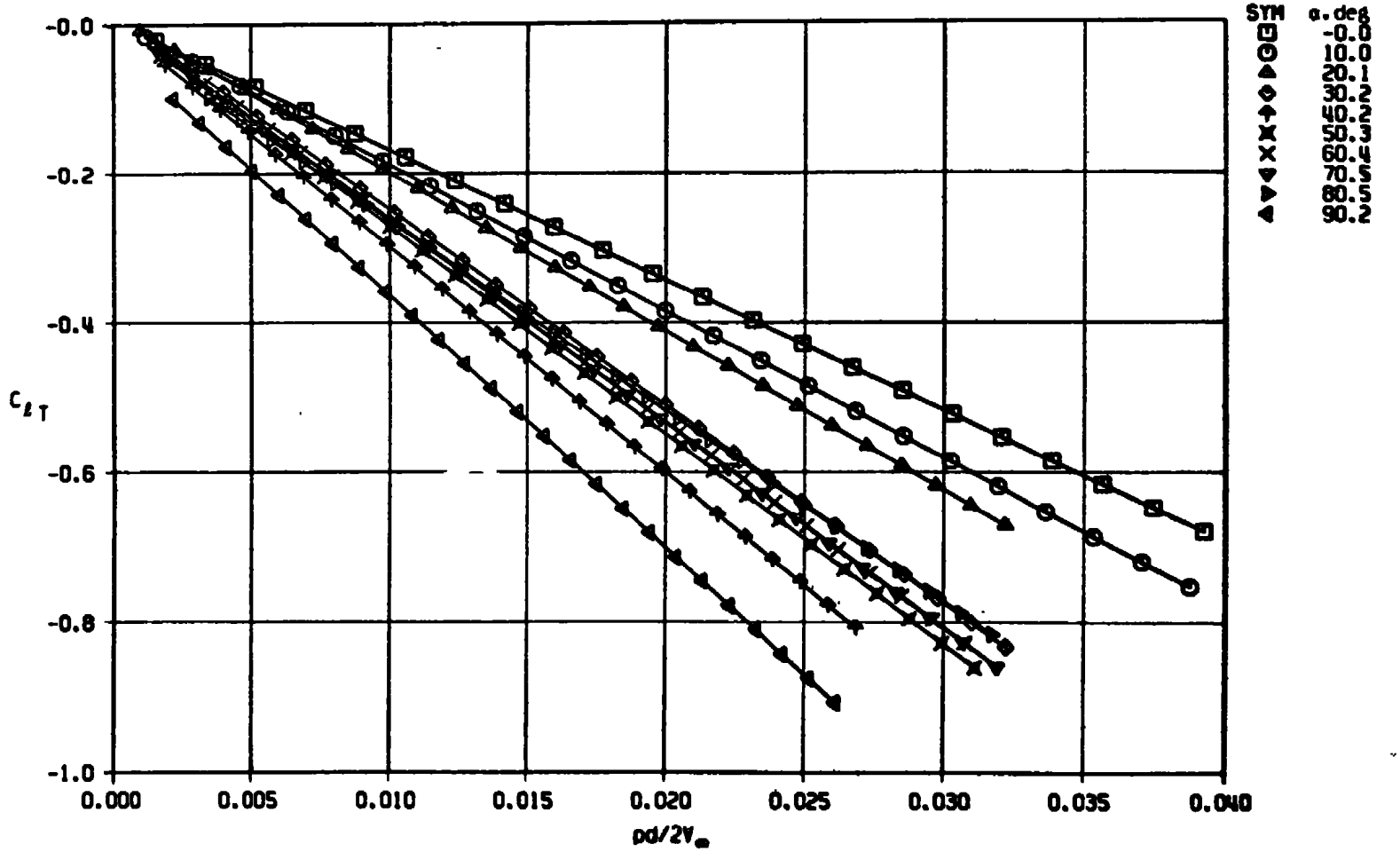

c. $M_\infty = 2.50$, $Re_d = 1.86 \times 10^5$, spin down with $\delta = 0$ deg

Figure 8. Concluded.

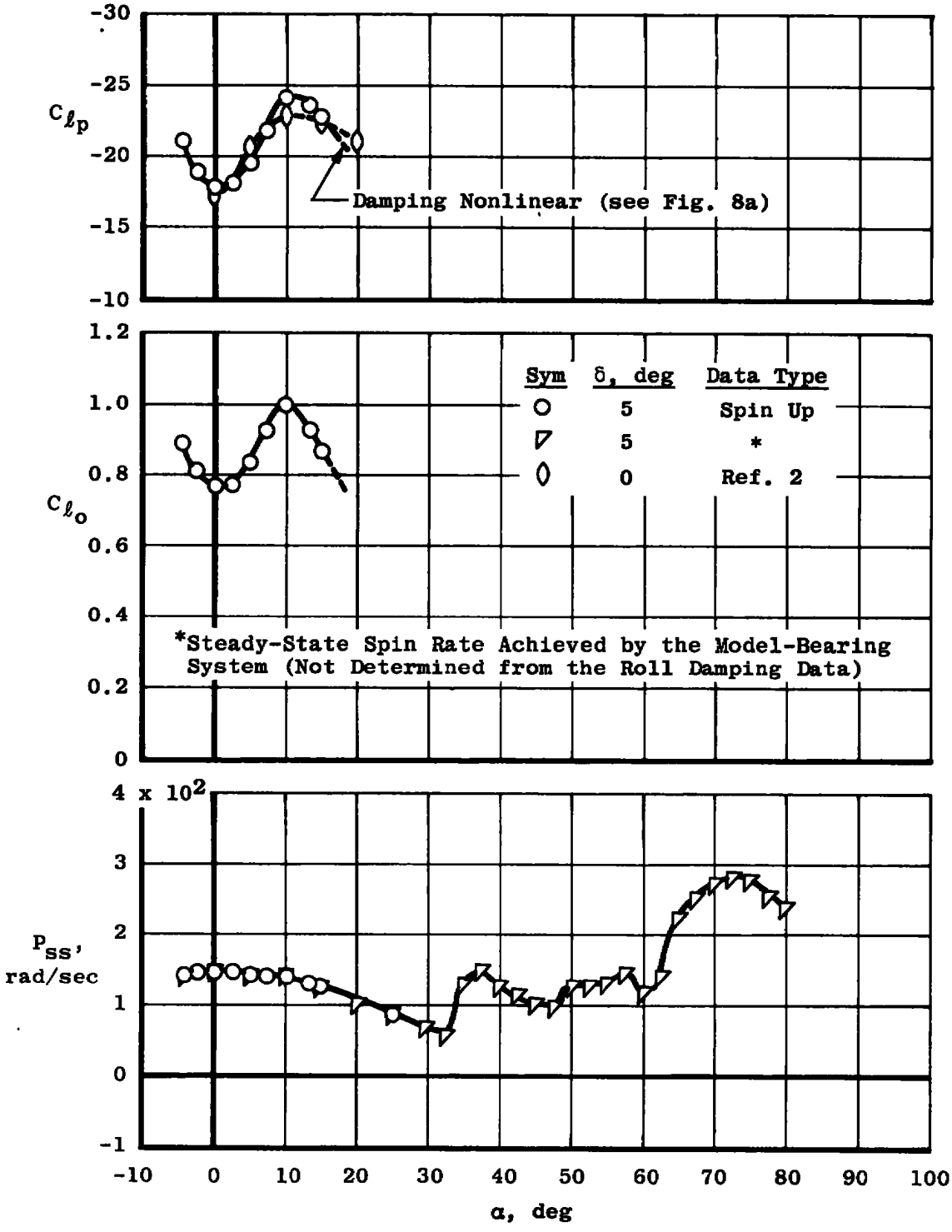

a. $M_\infty = 0.22$, $Re_d = 1.05 \times 10^5$

Figure 9. Roll-damping characteristics of the Basic Finner Model.

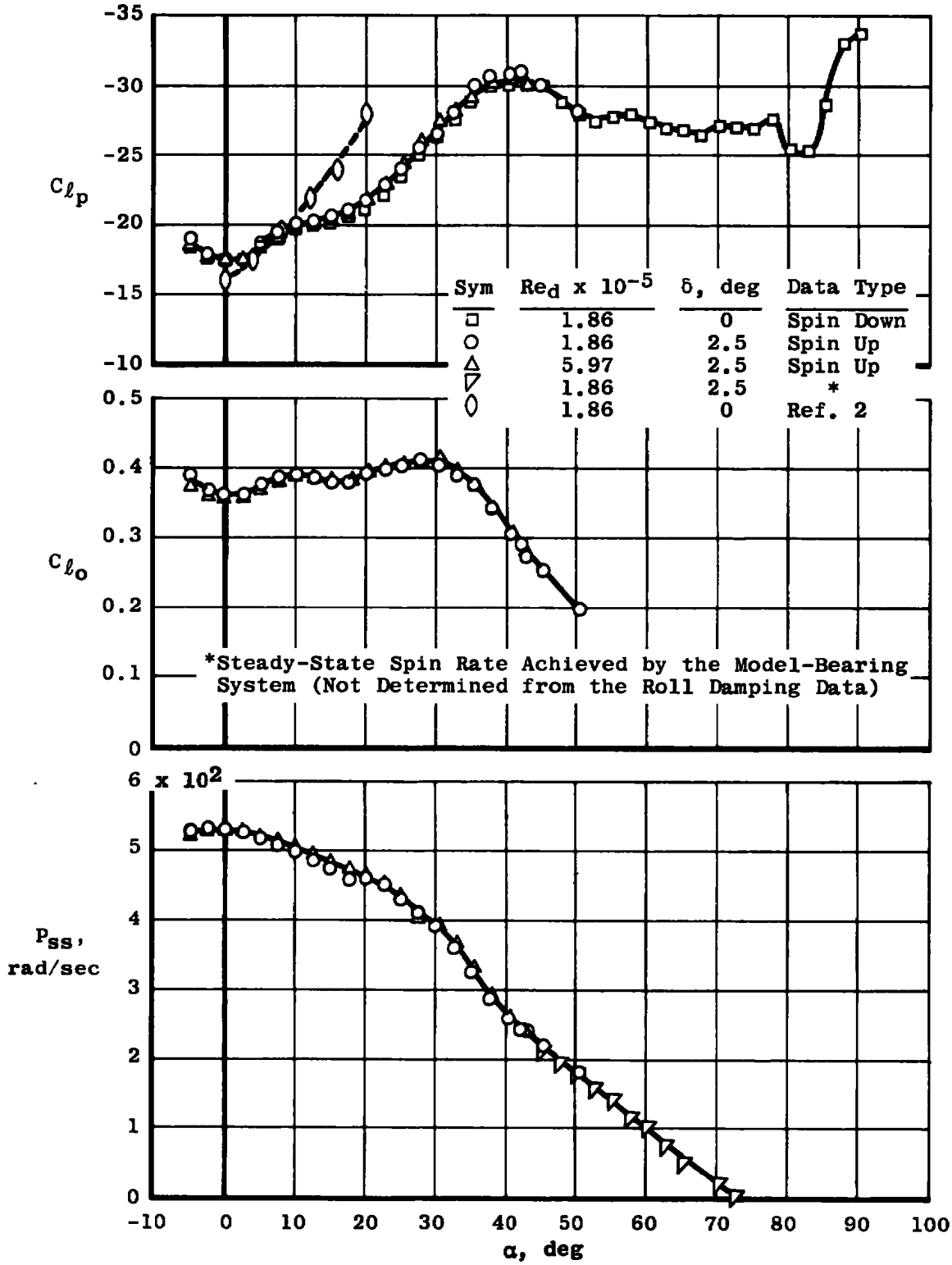

b. $M_\infty = 2.50$, $Re_d = 1.86 \times 10^5$

Figure 9. Continued.

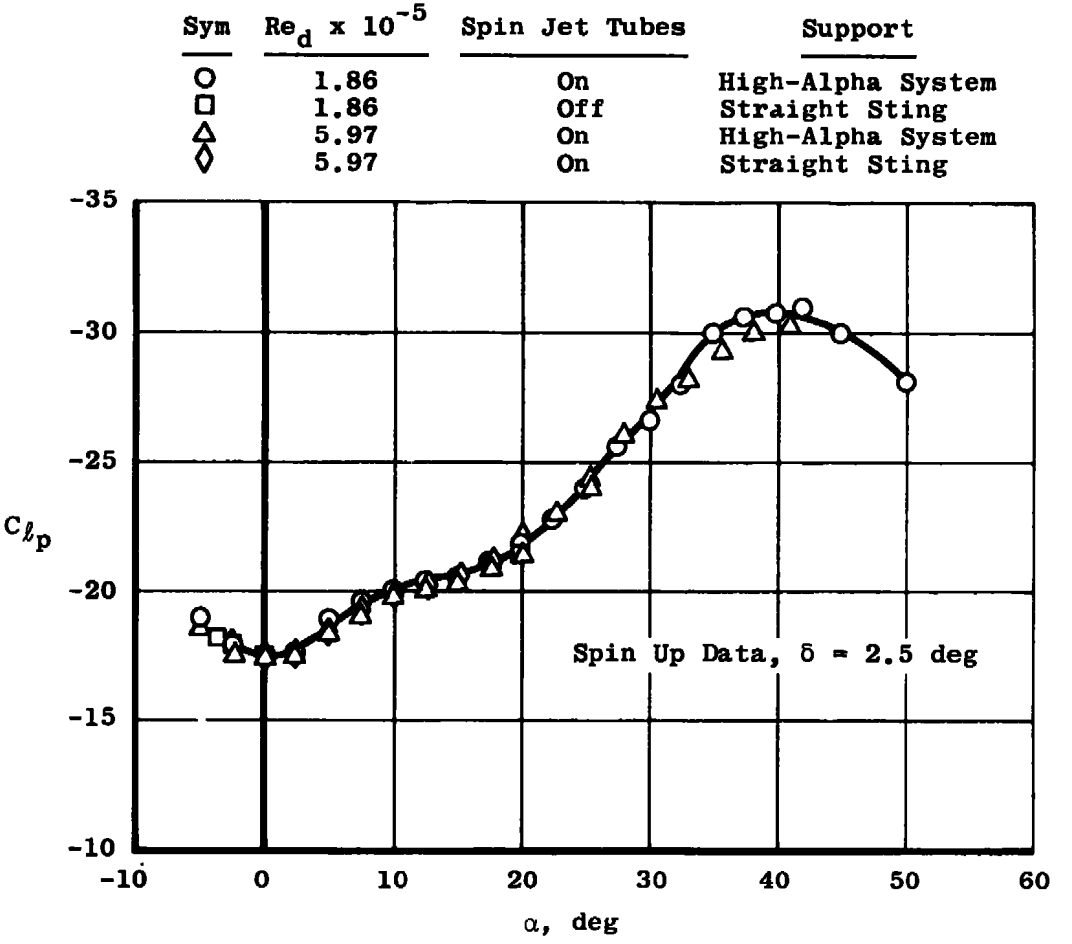

c. Effects of support system and Reynolds number, $M_\infty = 2.5$
Figure 9. Concluded.

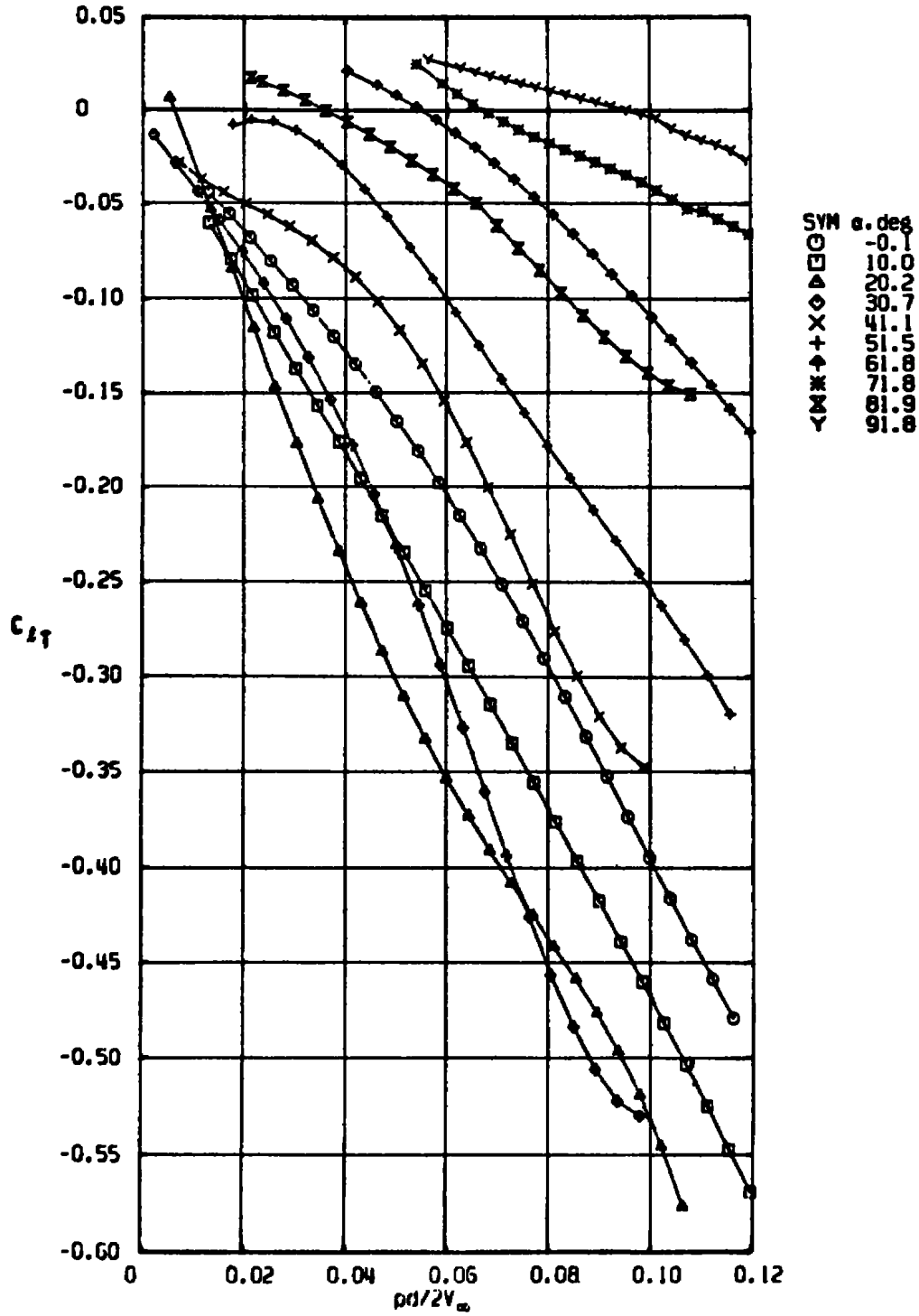

a. $M_\infty = 0.60$, $Re_d = 2.60 \times 10^5$

Figure 10. Variation of $C\ell_T$ with spin rate for the Modified Basic Finner Model.

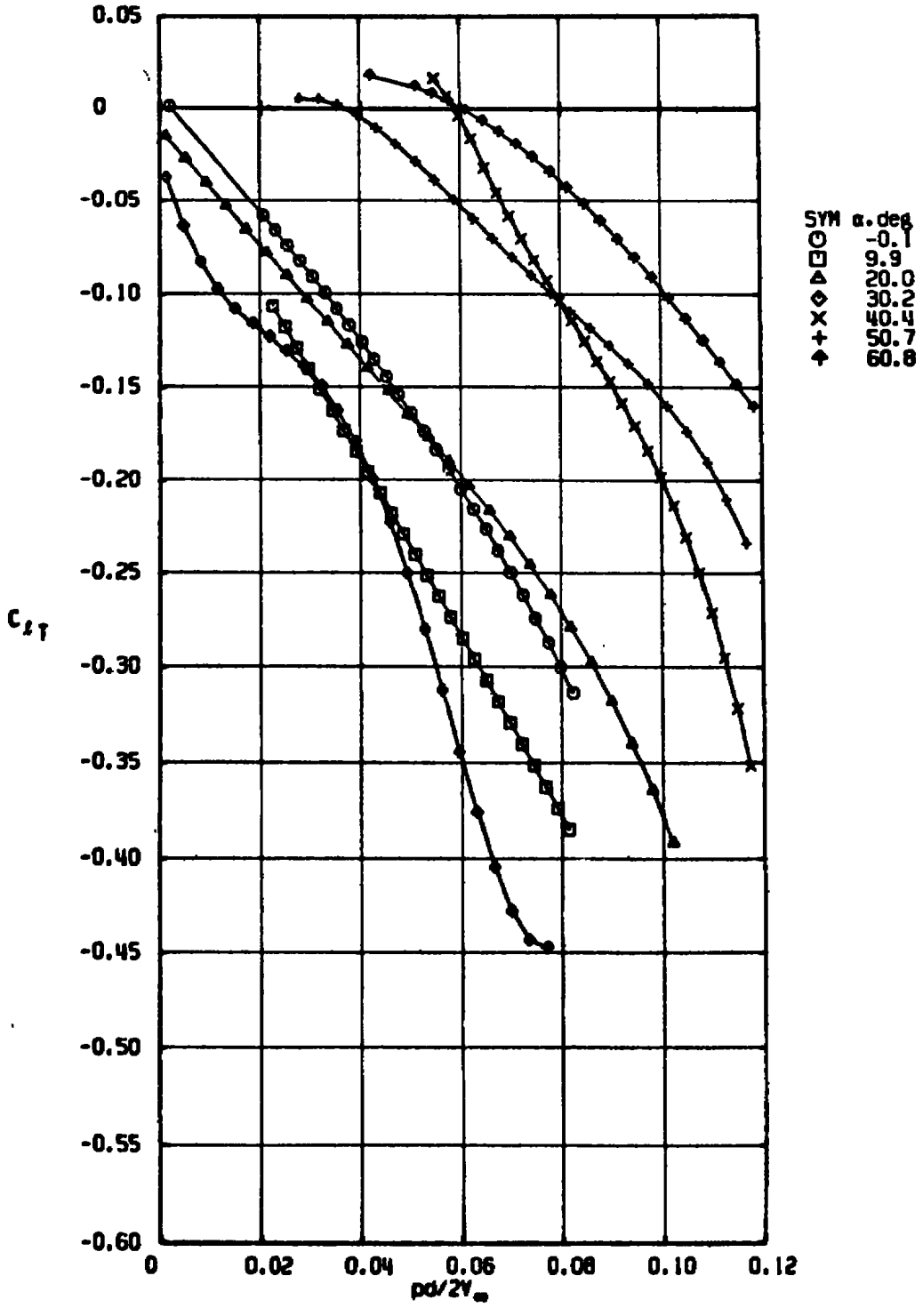

b. $M_\infty = 0.60$, $Re_d = 4.17 \times 10^5$

Figure 10. Continued.

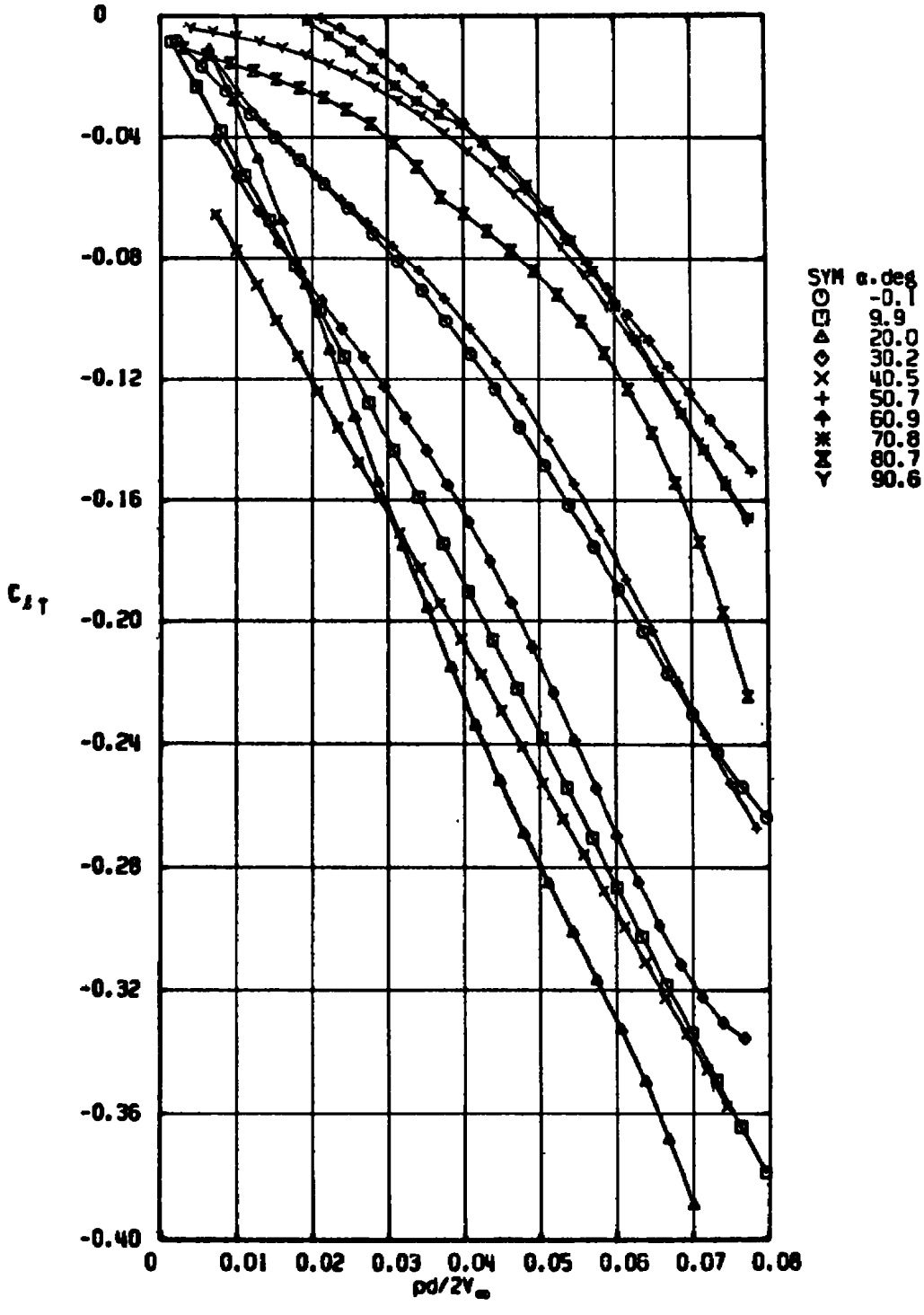

c. $M_\infty = 0.90$, $Re_d = 2.60 \times 10^5$

Figure 10. Continued.

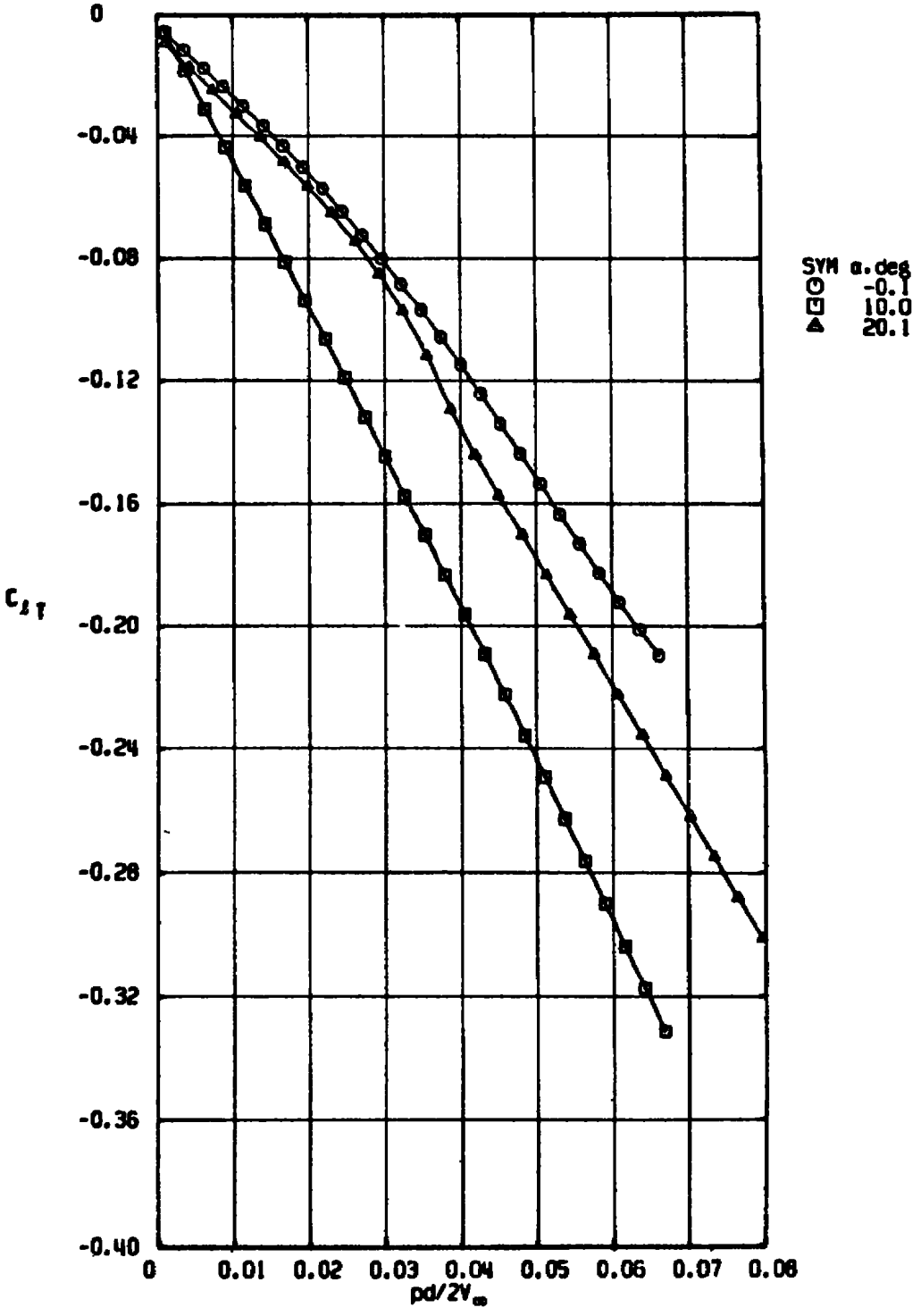

d. $M_\infty = 0.90$, $Re_d = 4.17 \times 10^5$

Figure 10. Continued.

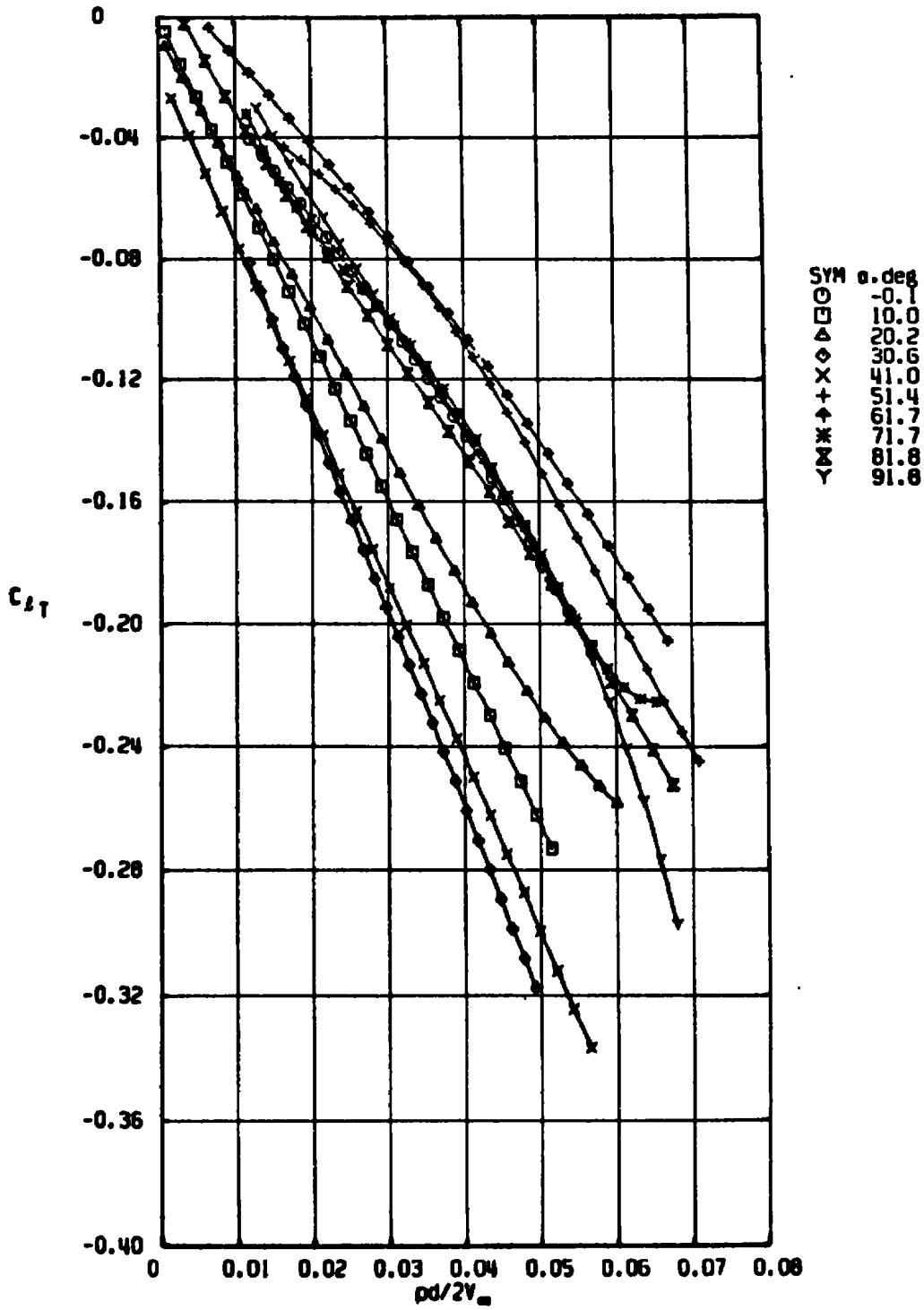

e. $M_\infty = 1.15$, $Re_d = 4.17 \times 10^5$

Figure 10. Continued.

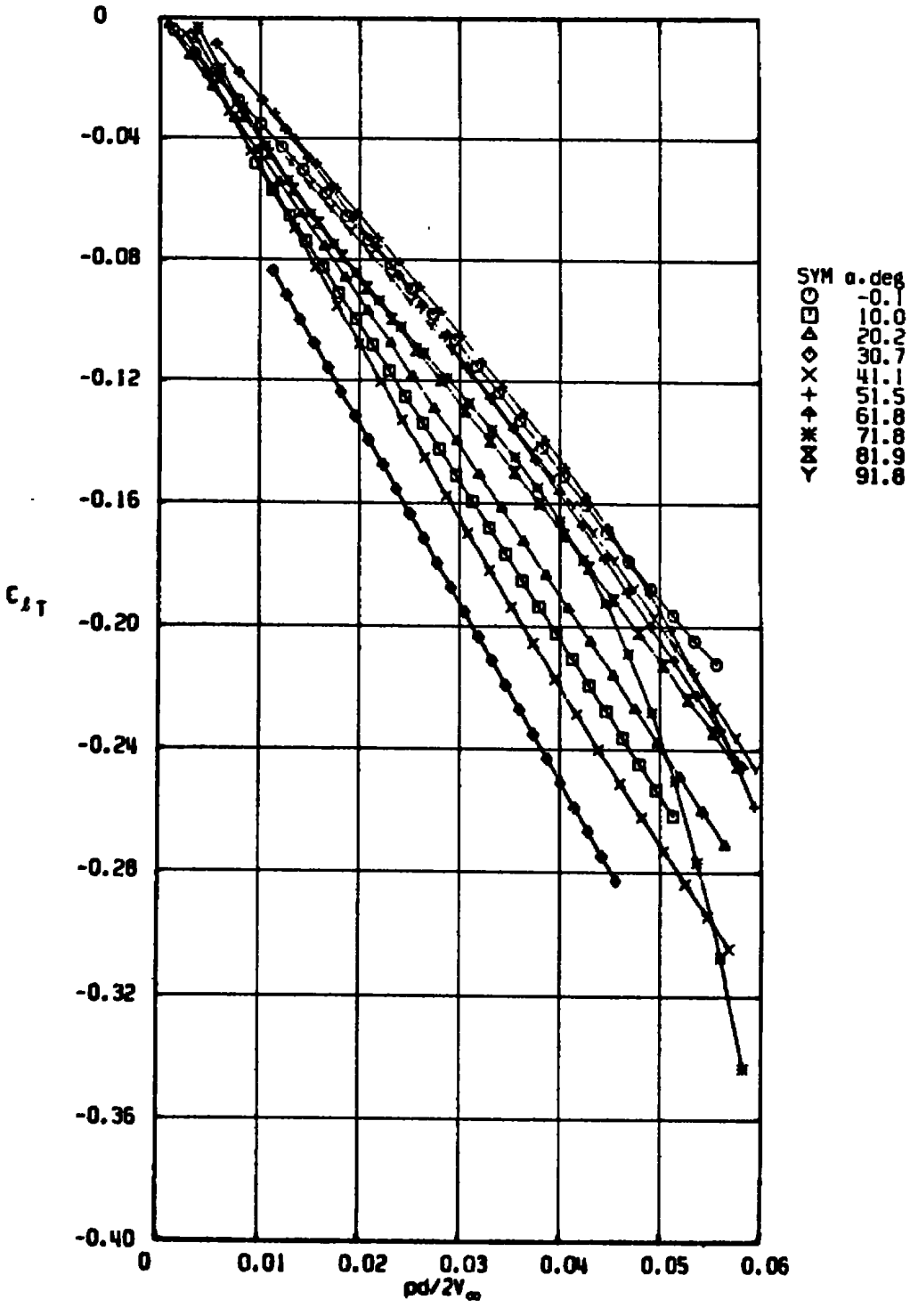

f. $M_\infty = 1.30$, $Re_d = 4.17 \times 10^5$

Figure 10. Continued.

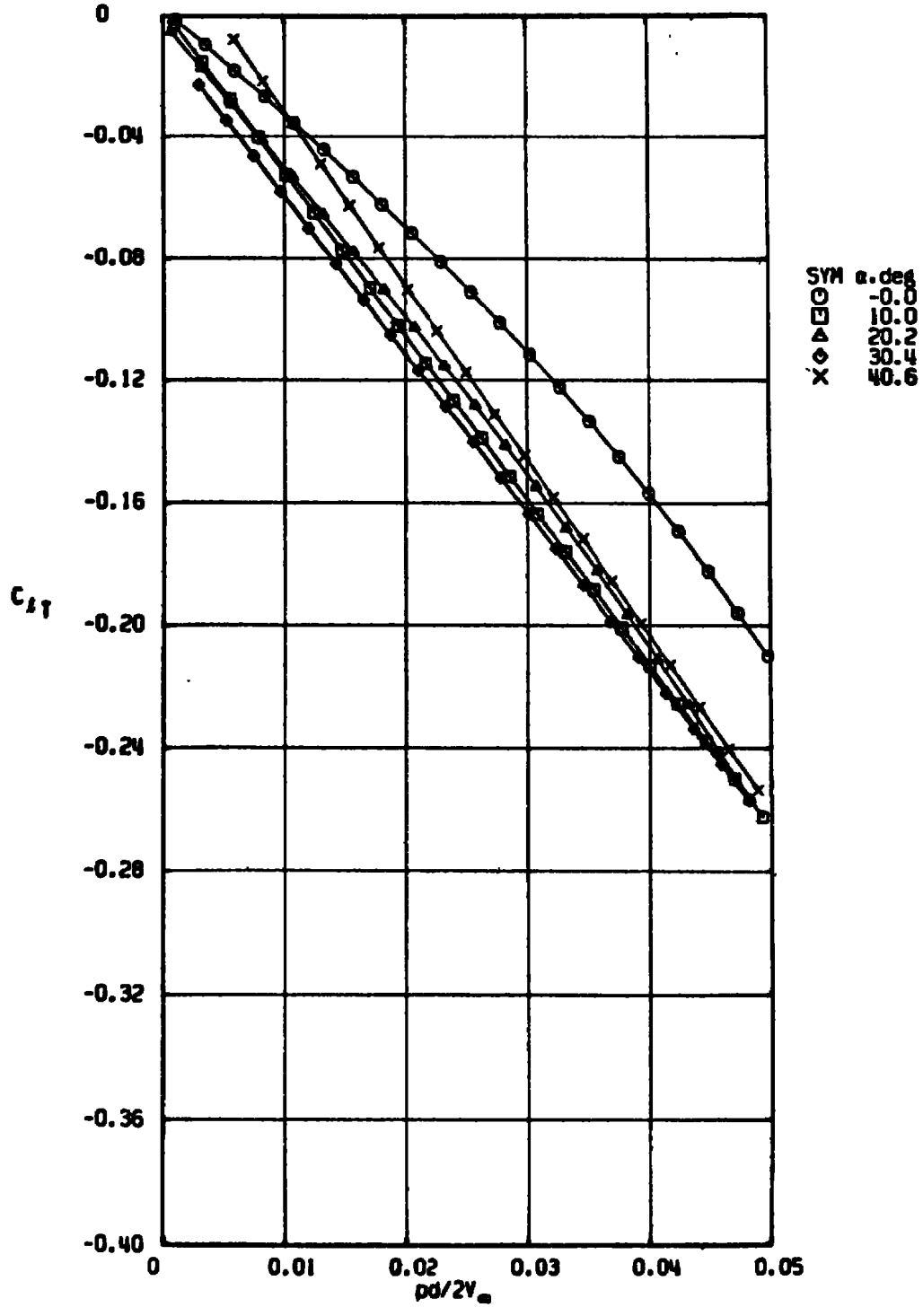

g. $M_\infty = 1.50$, $Re_d = 2.58 \times 10^5$

Figure 10. Continued.

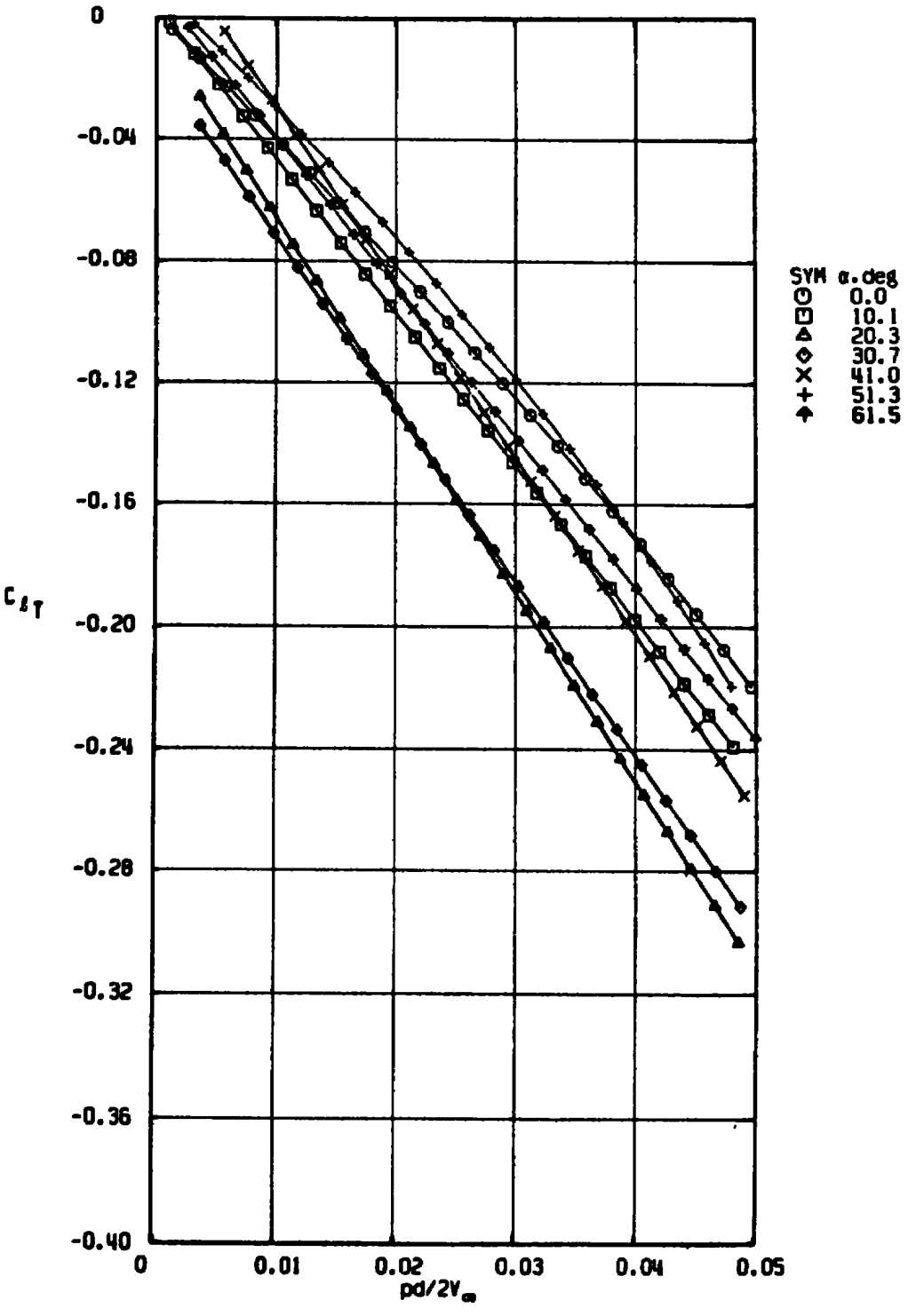

h. $M_\infty = 1.50$, $Re_d = 4.13 \times 10^5$

Figure 10. Continued.

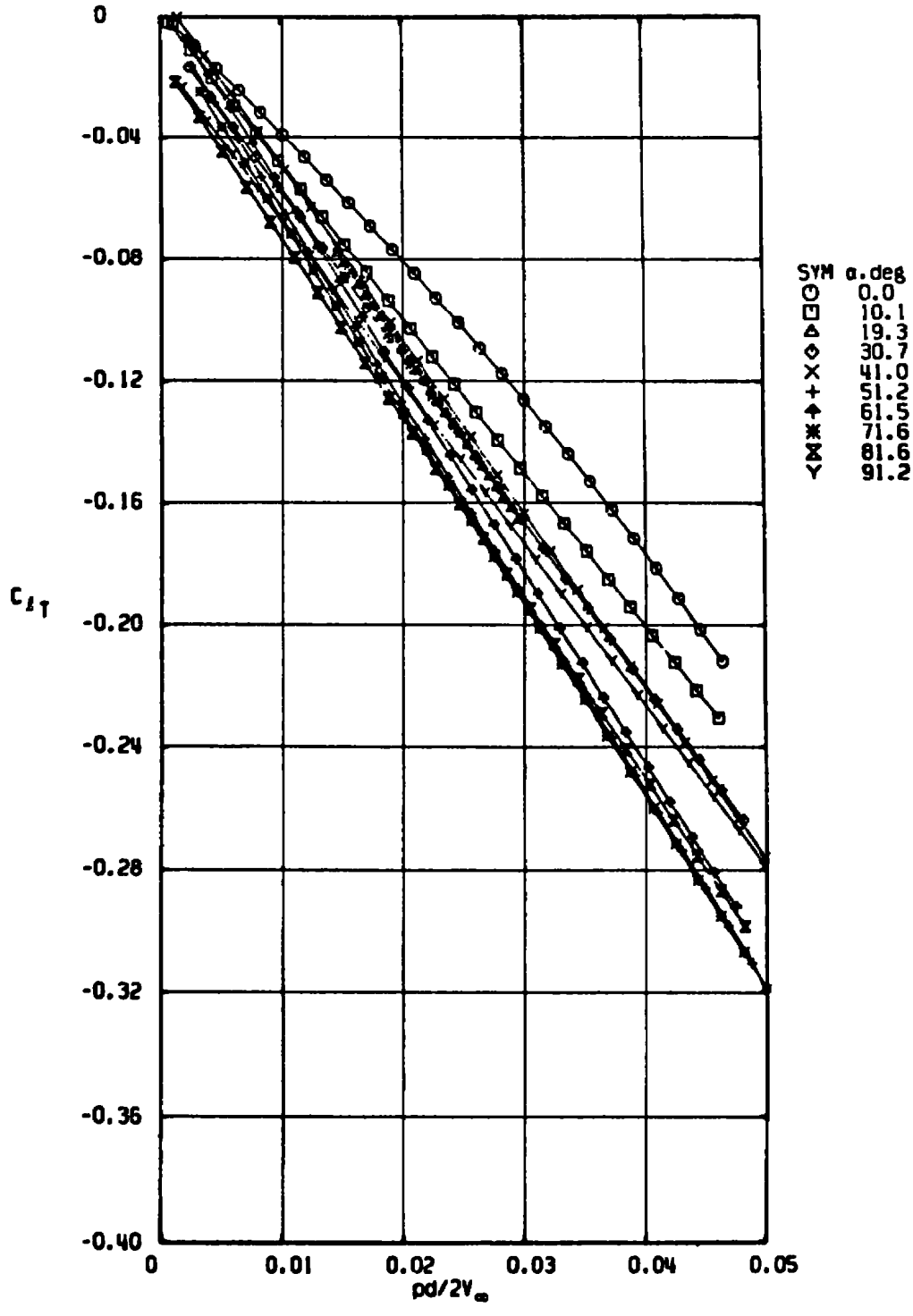

i. $M_\infty = 1.76$, $Re_d = 4.13 \times 10^5$

Figure 10. Continued.

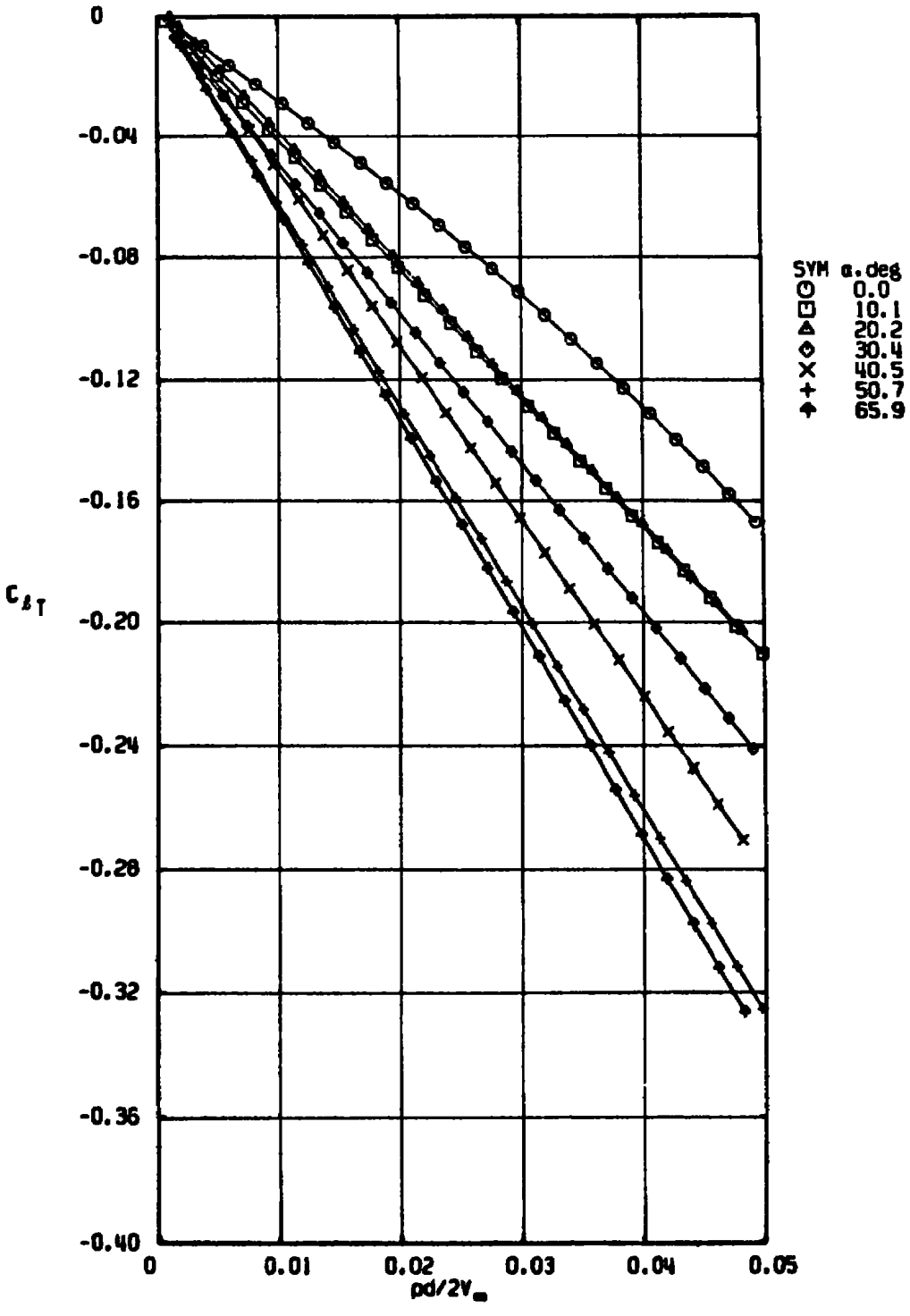

j. $M_\infty = 2.00$, $Re_d = 2.57 \times 10^5$

Figure 10. Continued.

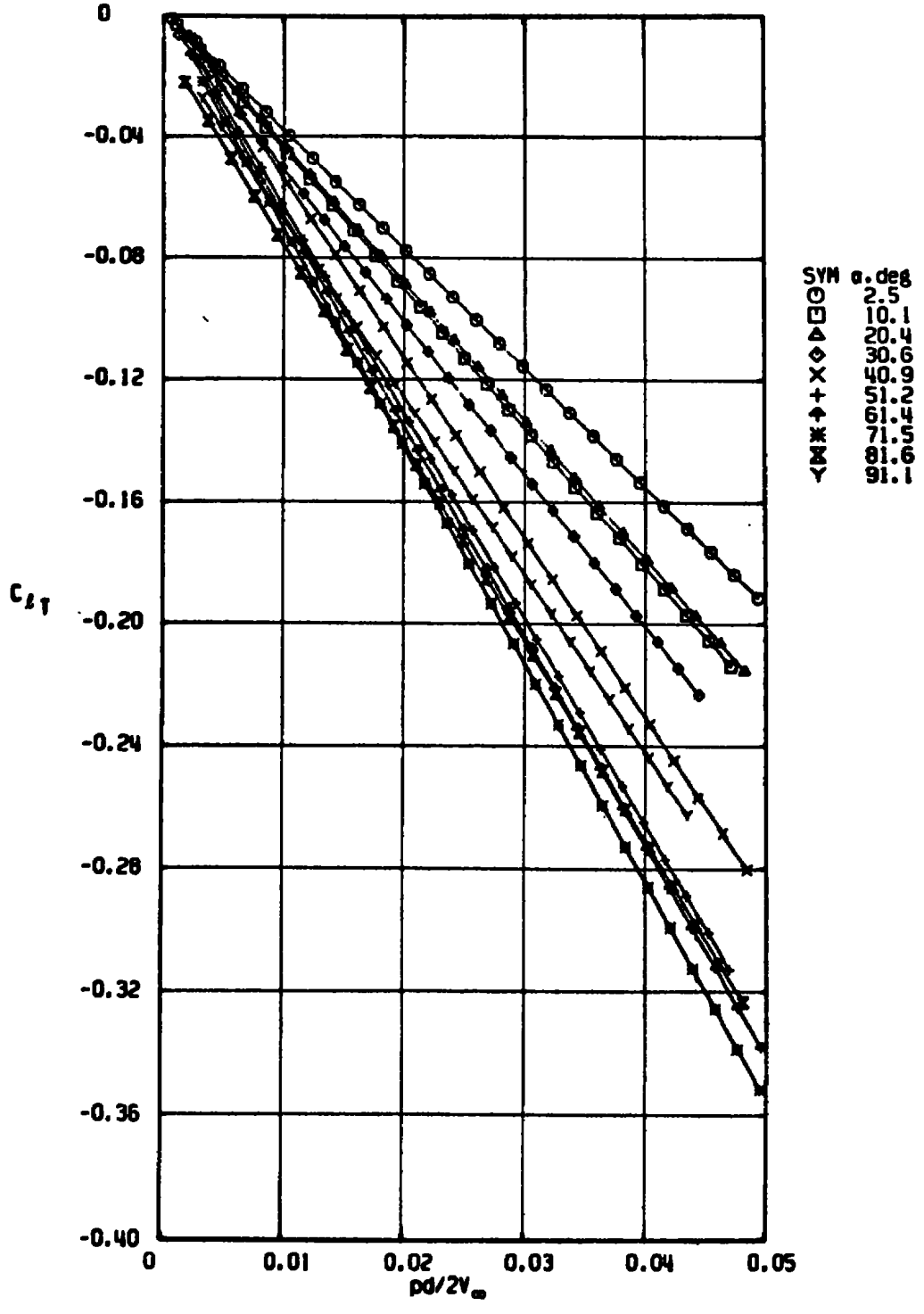

k. $M_\infty = 2.00$, $Re_d = 4.10 \times 10^5$

Figure 10. Continued.

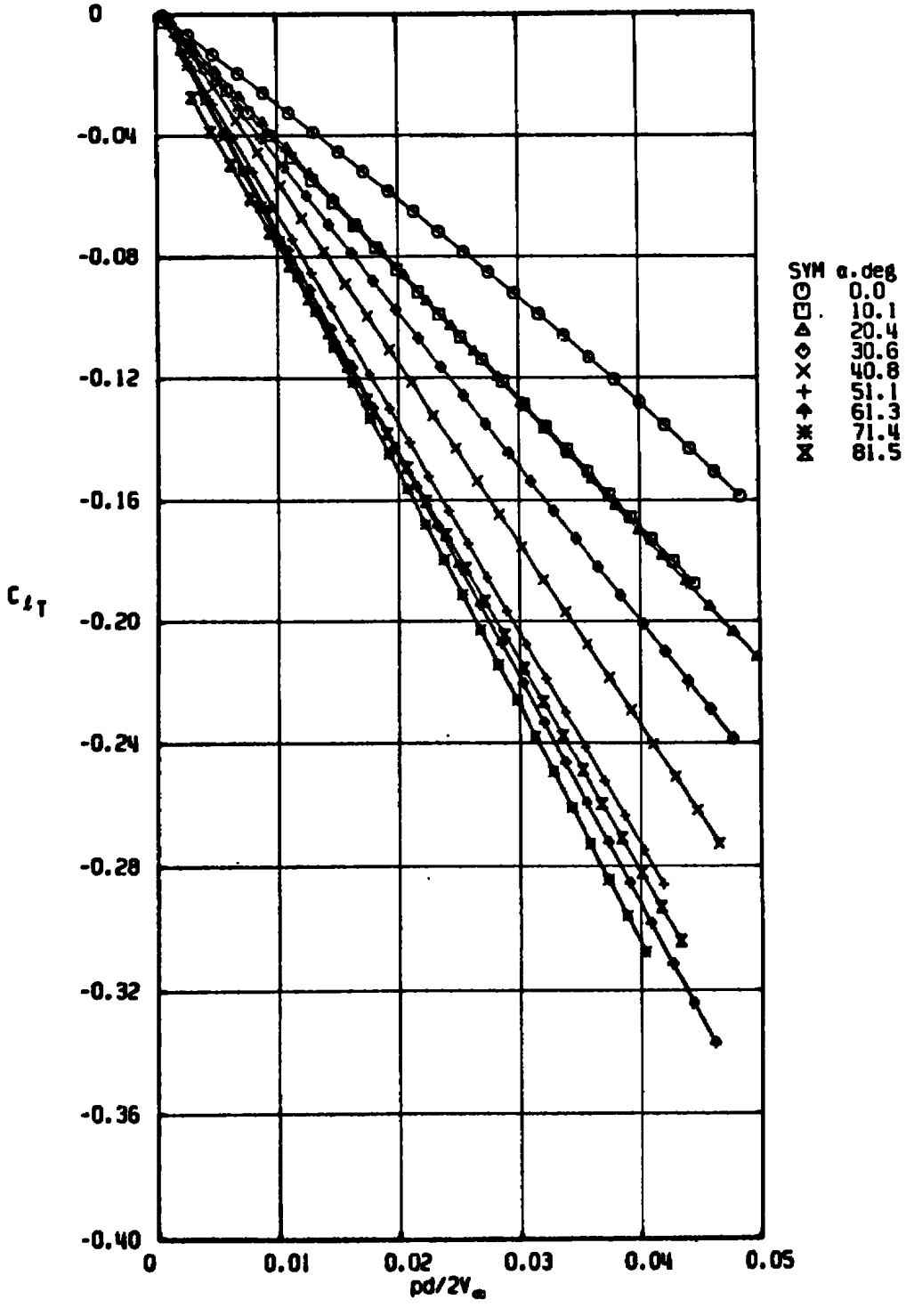

l. $M_\infty = 2.25$, $Re_d = 4.10 \times 10^5$

Figure 10. Continued.

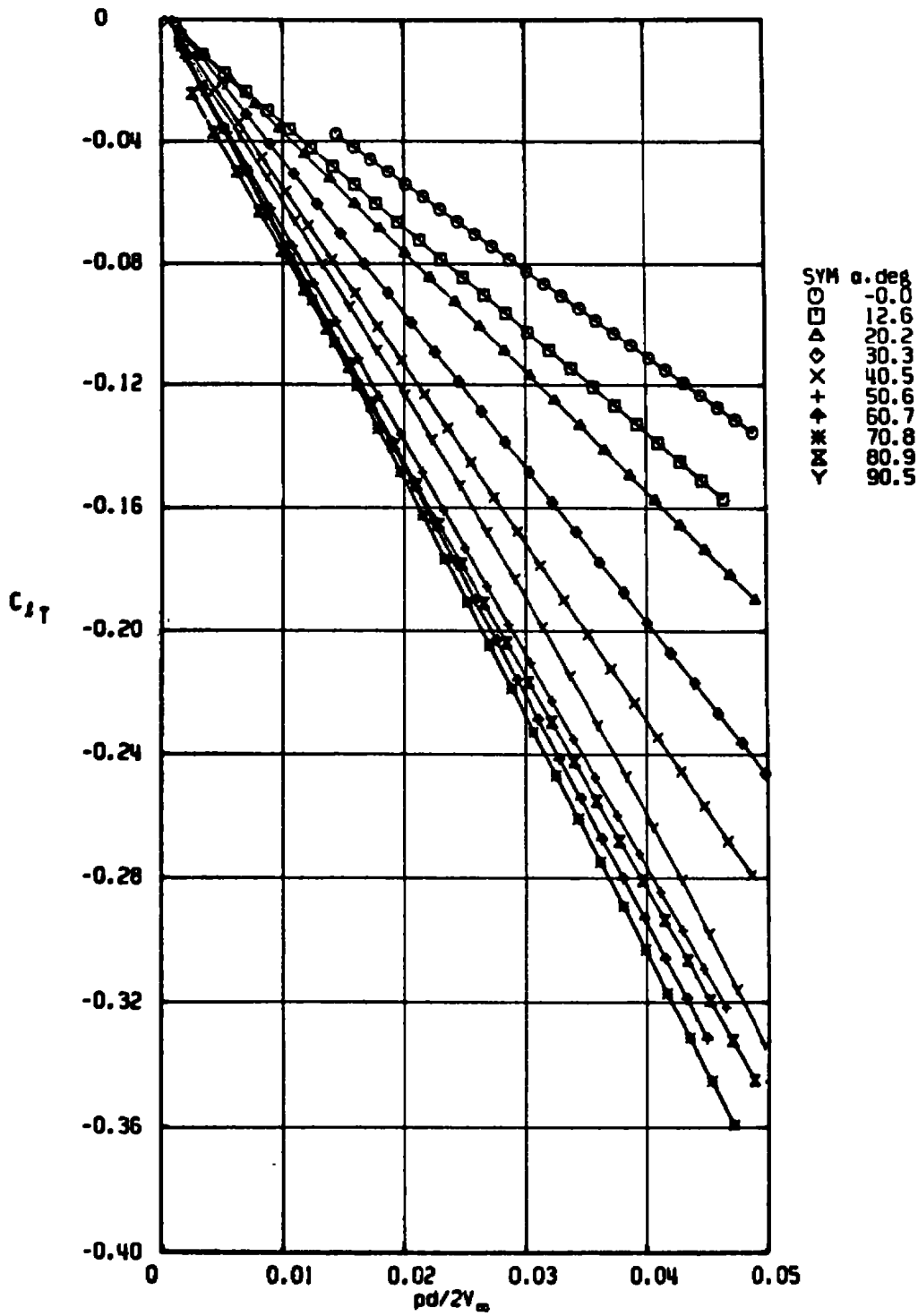

m. $M_\infty = 2.49$, $Re_d = 2.57 \times 10^5$

Figure 10. Continued.

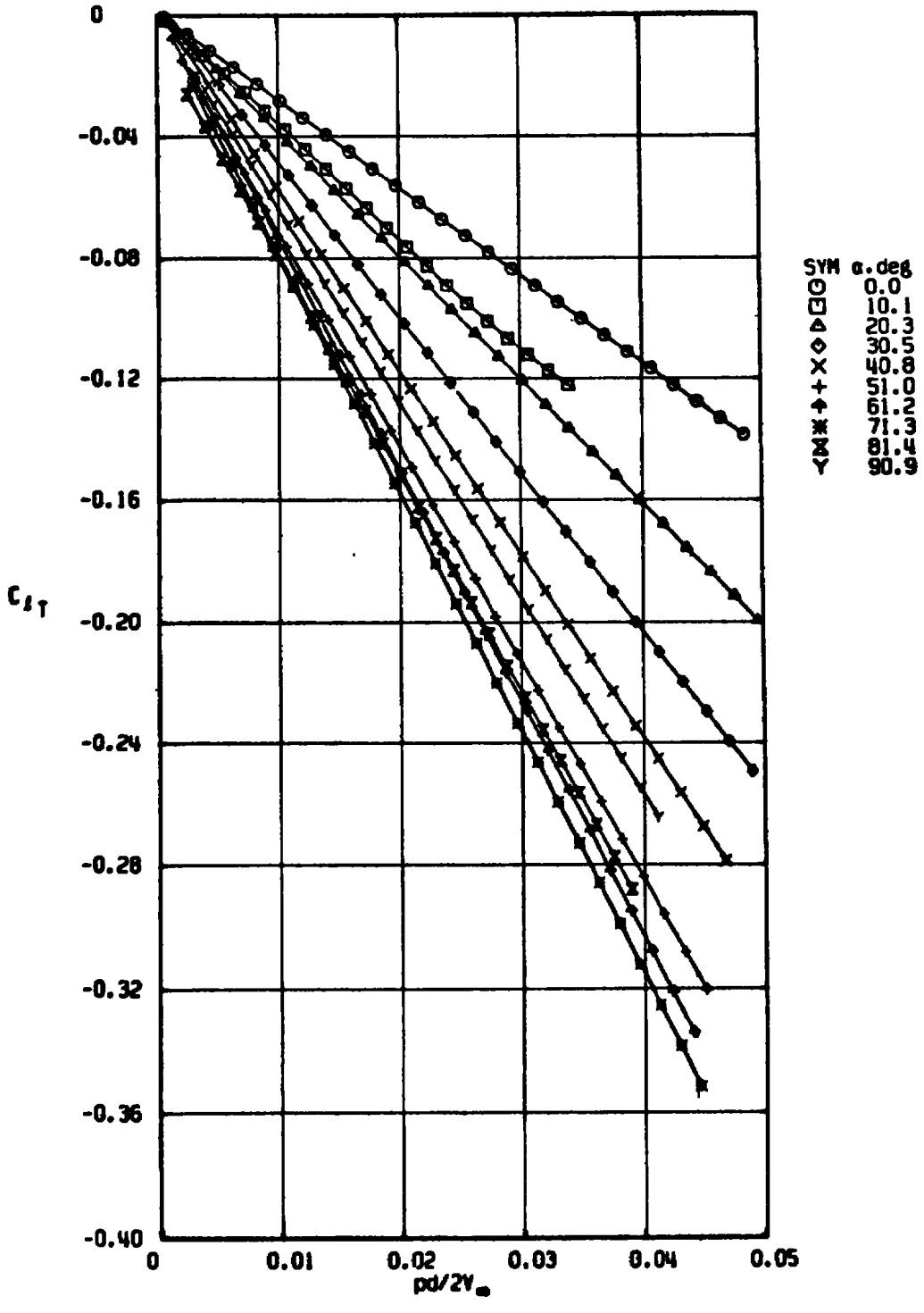

n. $M_\infty = 2.50$, $Re_d = 4.10 \times 10^5$

Figure 10. Concluded.

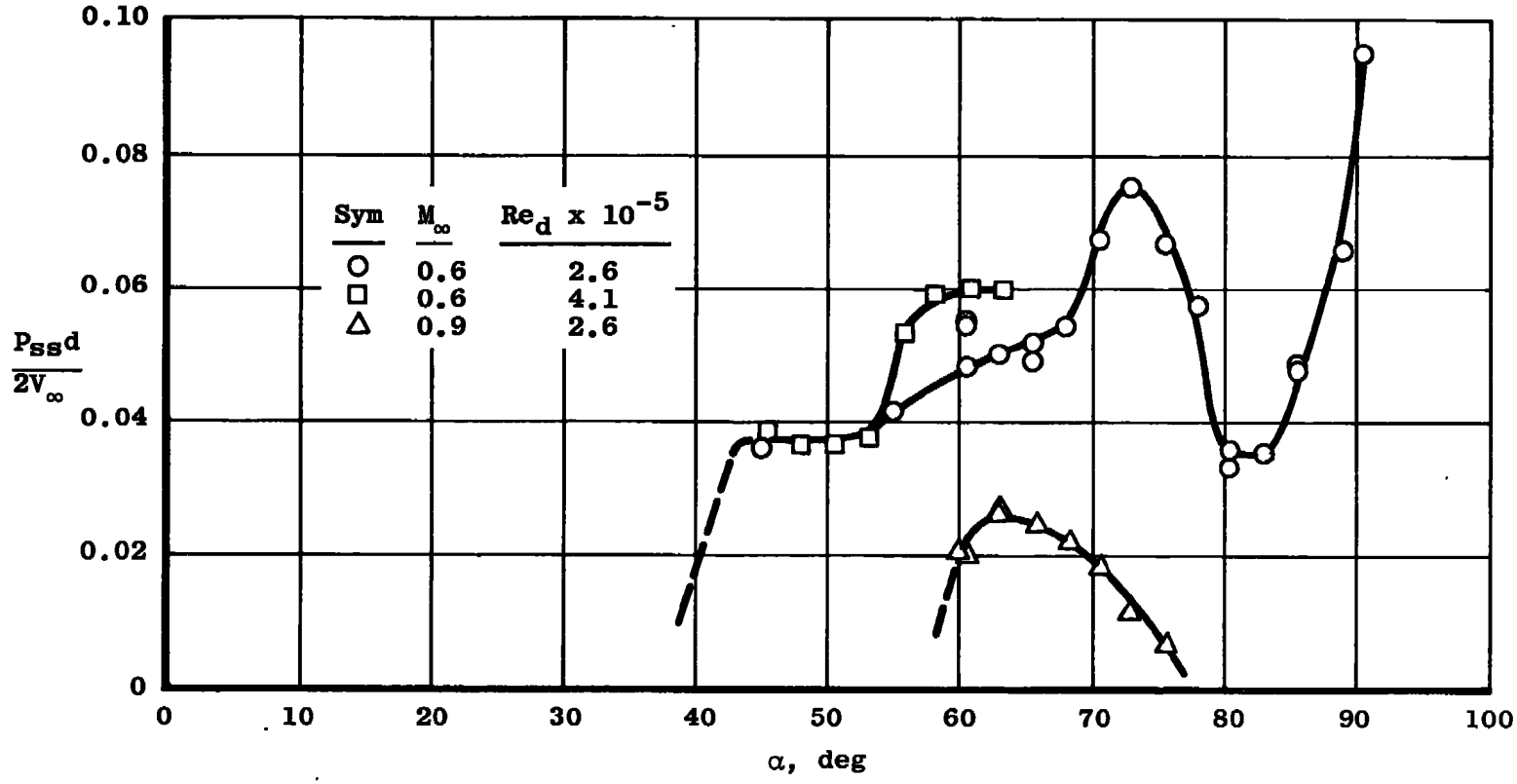

Figure 11. Autorotation characteristics of the Modified Basic Finner Model.

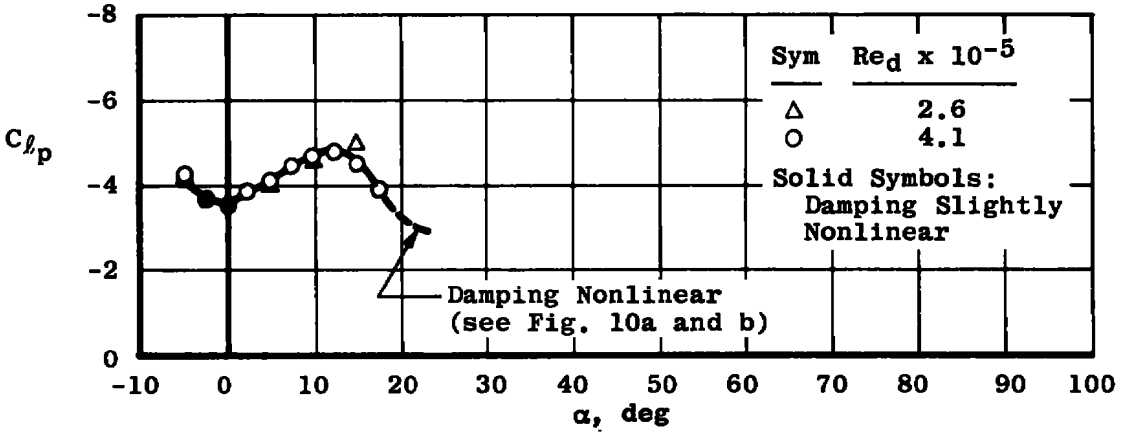

a. $M_\infty = 0.60$

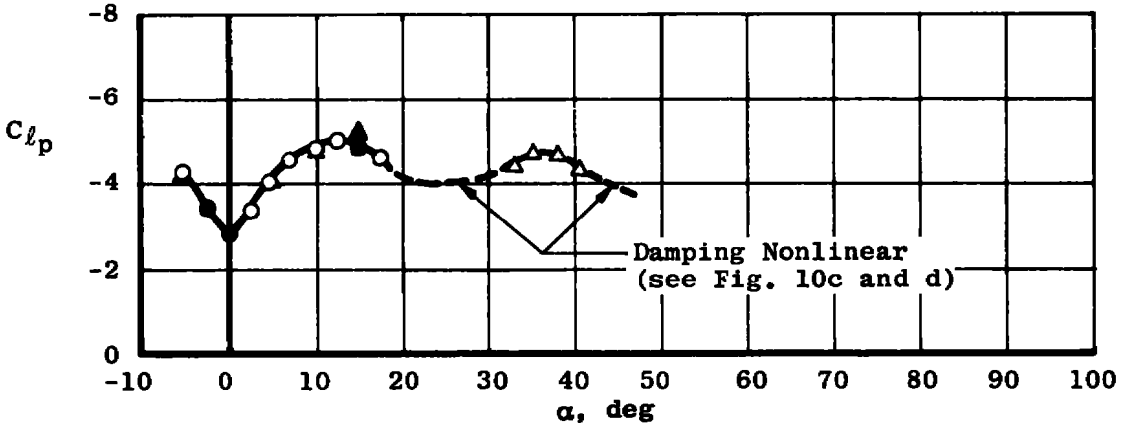

b. $M_\infty = 0.90$

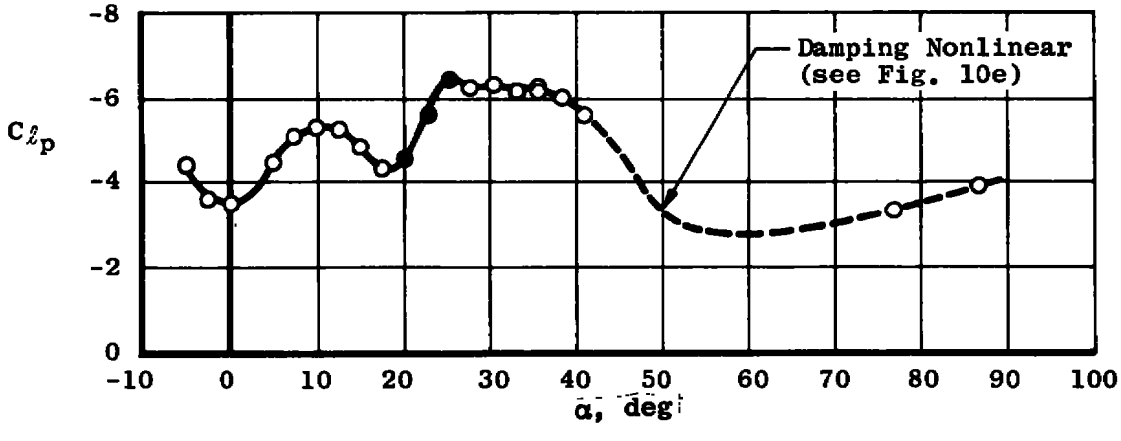

c. $M_\infty = 1.15$

Figure 12. Variation of C_{ℓ_p} with angle of attack for the Modified Basic Finner, linear damping.

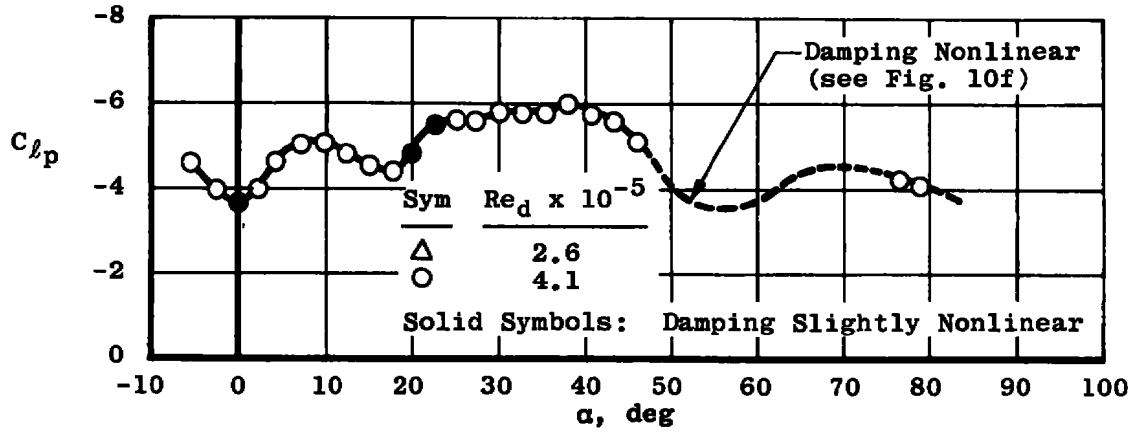

d. $M_\infty = 1.30$

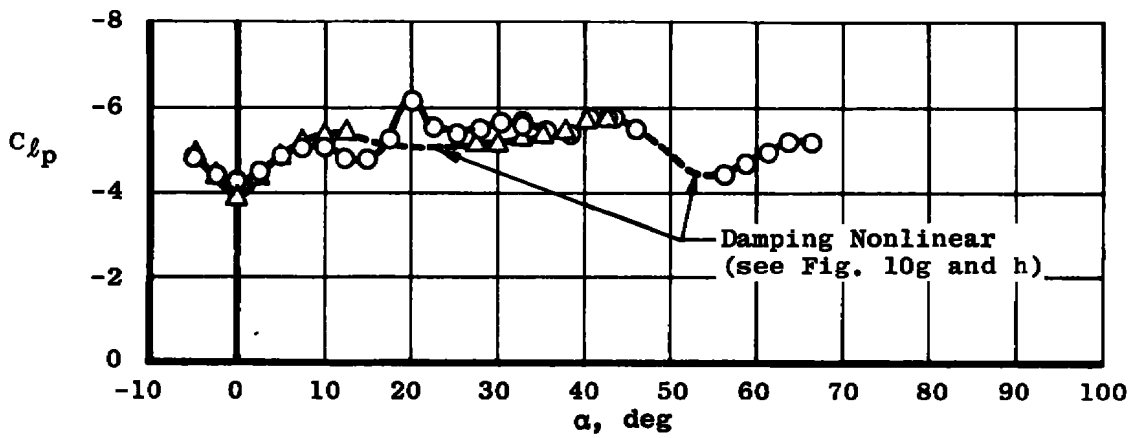

e. $M_\infty = 1.50$

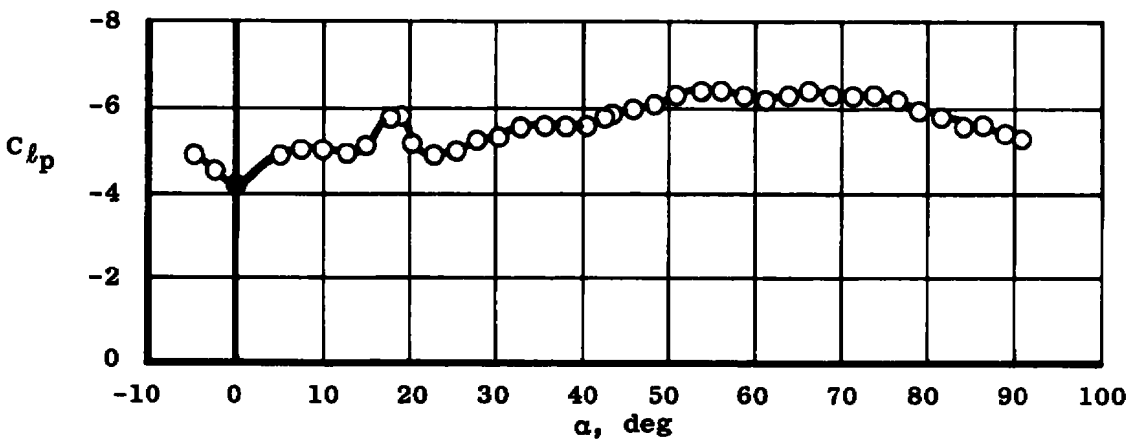

f. $M_\infty = 1.76$

Figure 12. Continued.

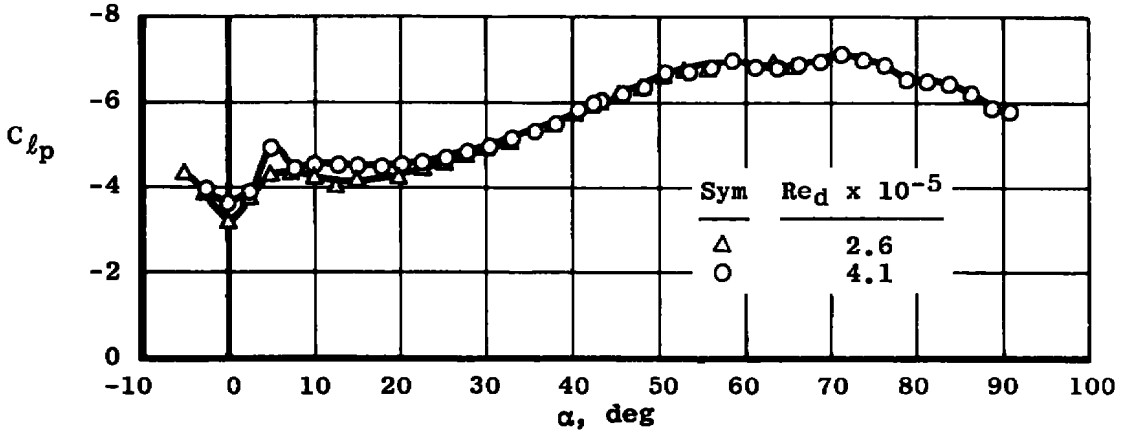

g. $M_\infty = 2.00$

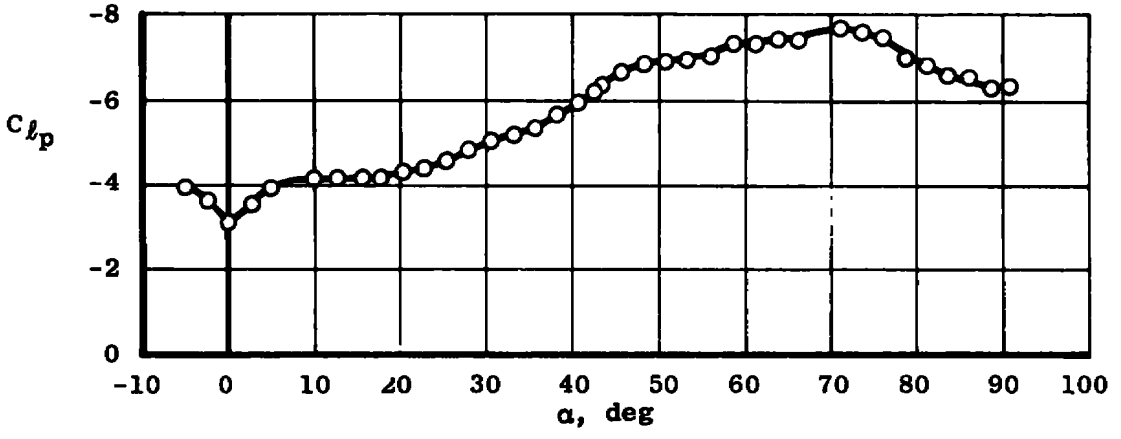

h. $M_\infty = 2.25$

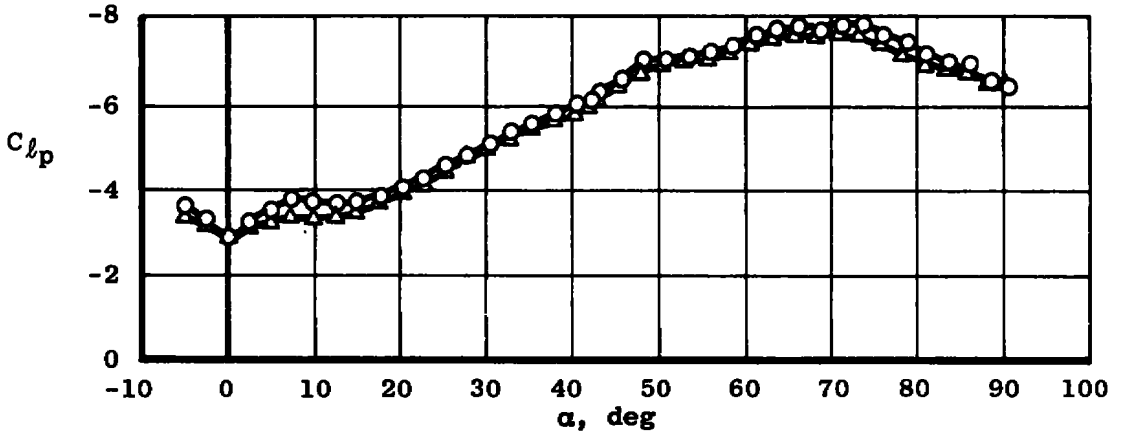

i. $M_\infty = 2.50$

Figure 12. Concluded.

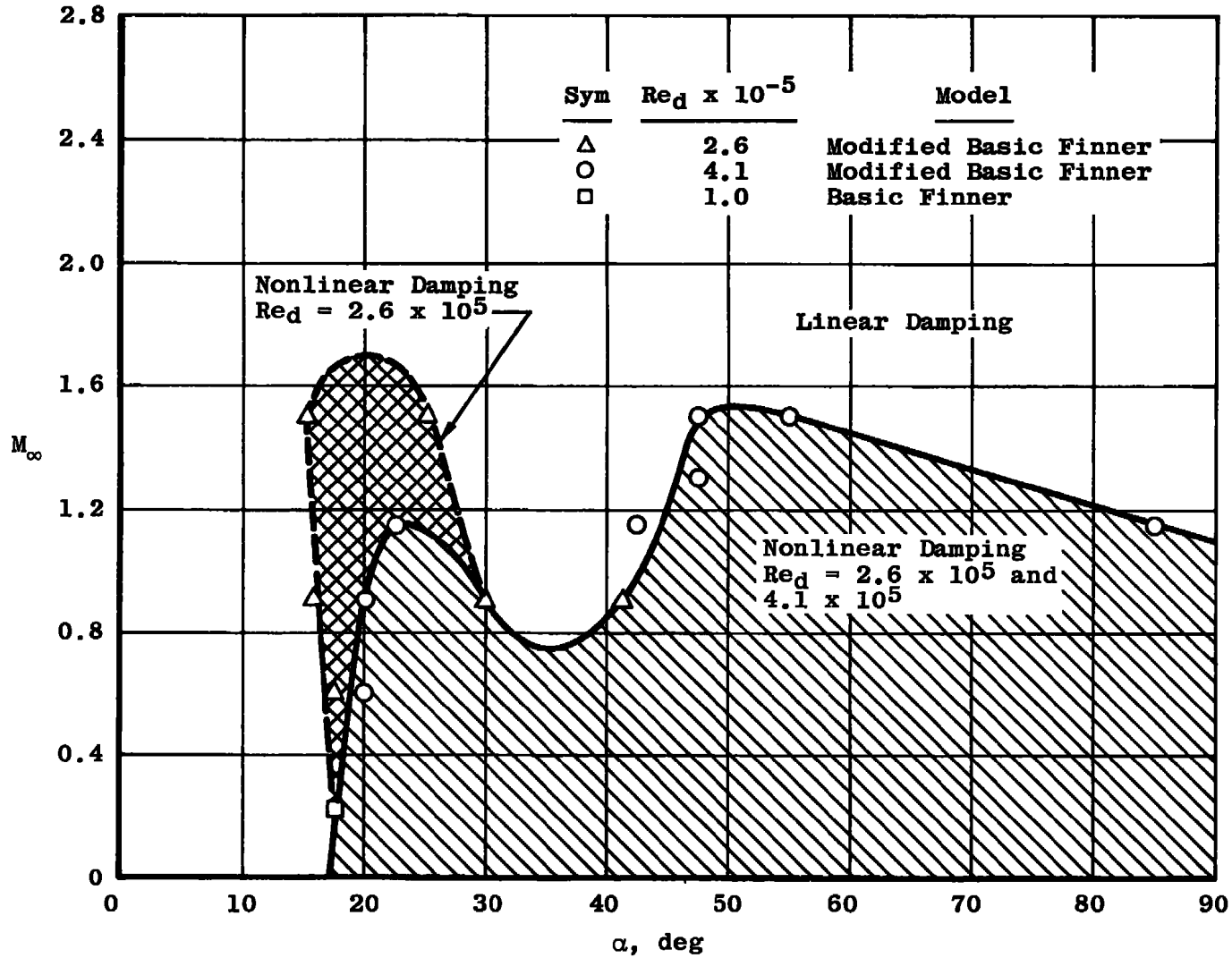

Figure 13. Approximate region of nonlinear damping.

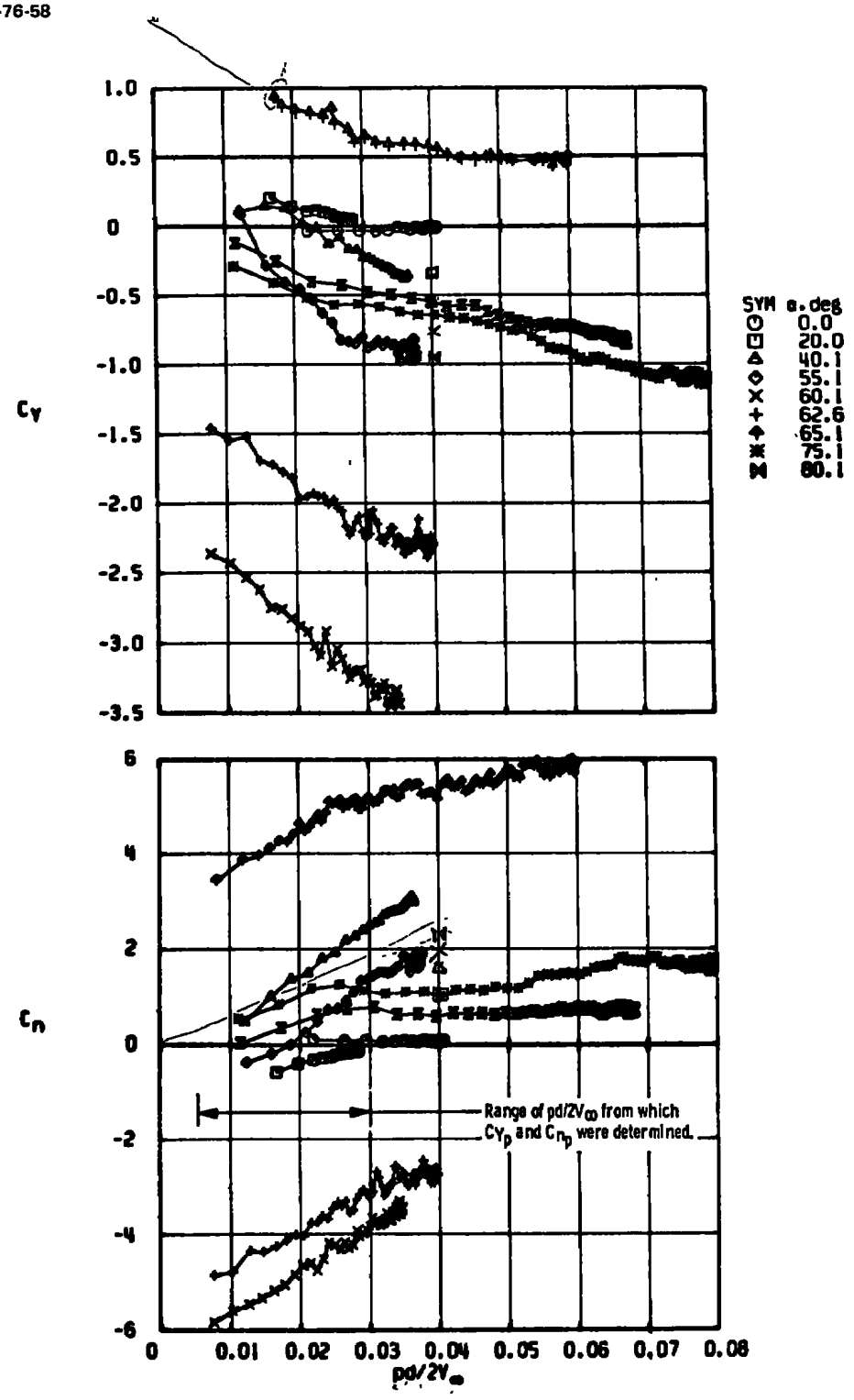

a. $M_\infty = 0.22$, $Re_d = 1.05 \times 10^5$

Figure 14. Magnus-force and moment characteristics of the Basic Finner Model.

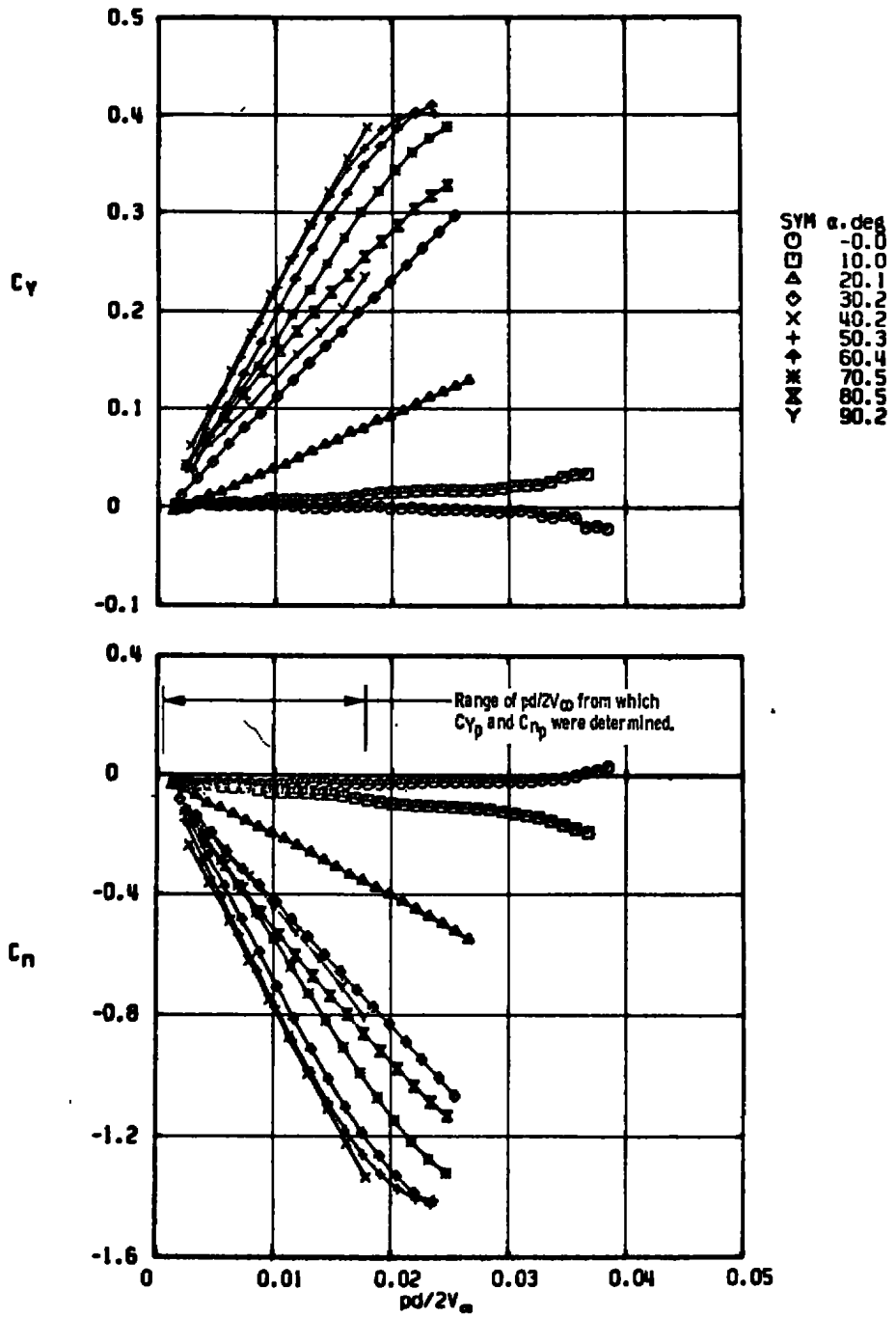

b. $M_\infty = 2.50$, $Re_d = 1.86 \times 10^5$

Figure 14. Concluded.

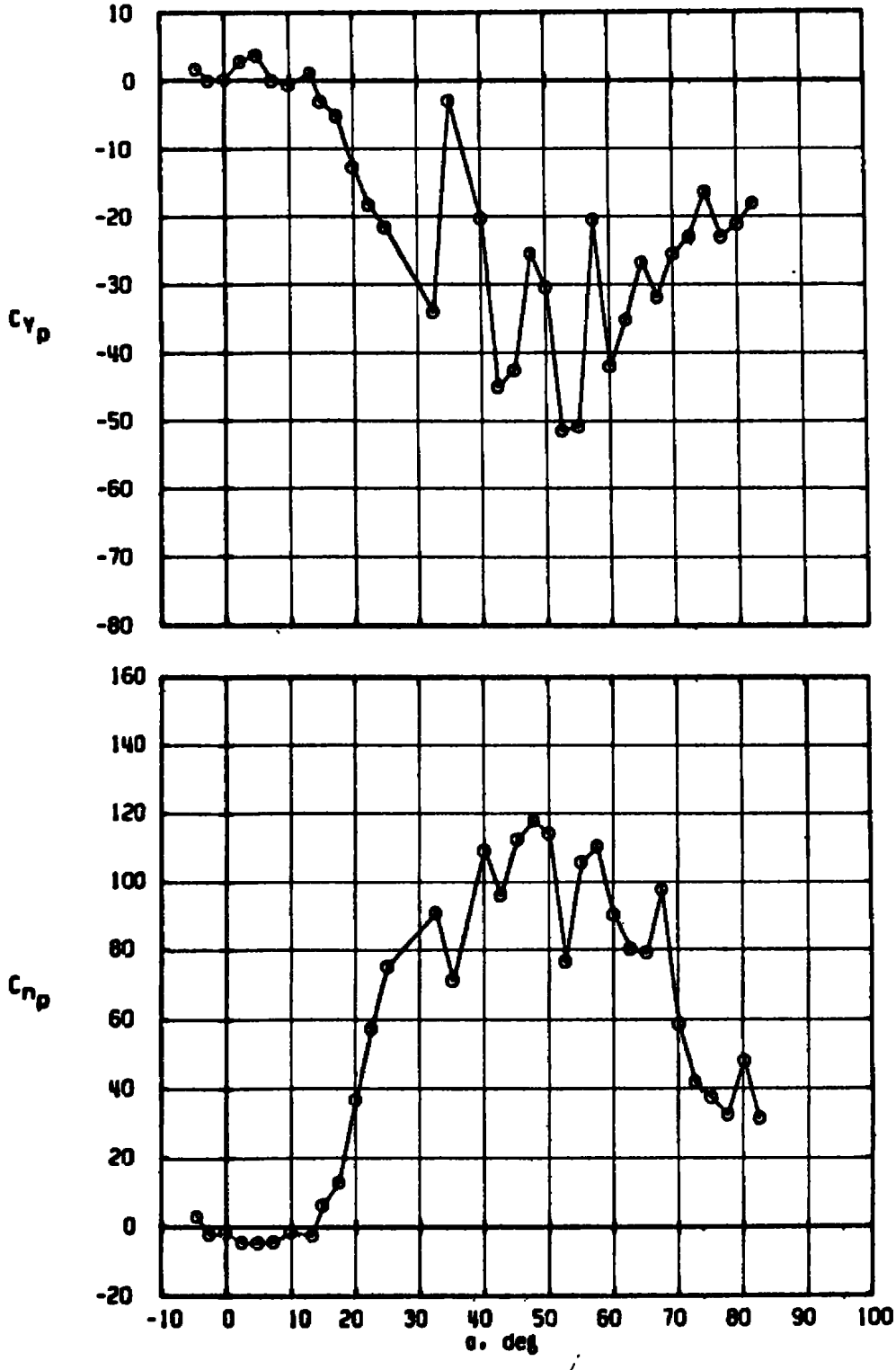

a. $M_\infty = 0.22$, $Re_d = 1.05 \times 10^5$

Figure 15. Variation of C_{Y_p} and C_{n_p} with angle of attack for the Basic Finner Model.

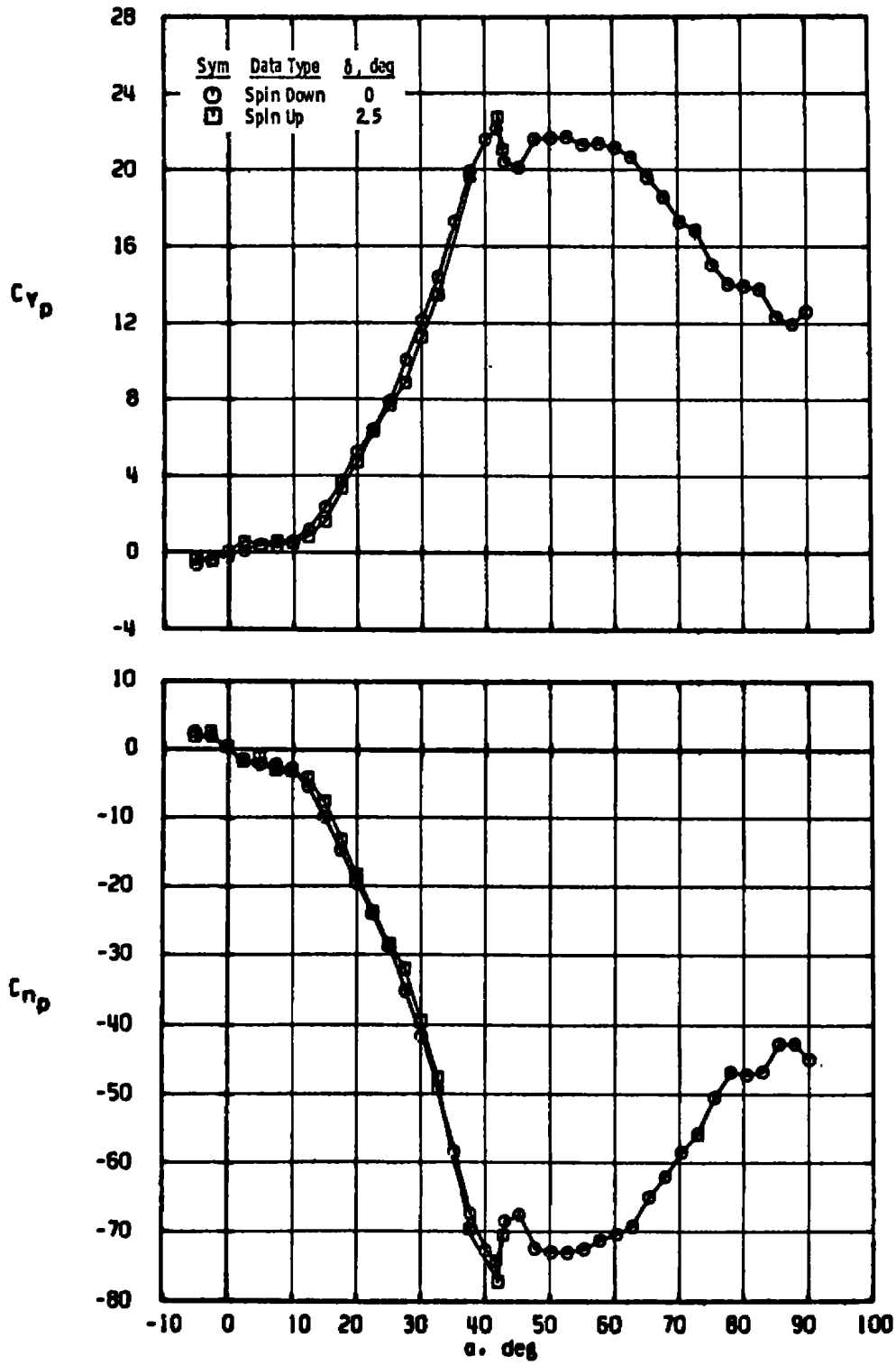

b. $M_\infty = 2.50$, $Re_d = 1.86 \times 10^5$

Figure 15. Continued.

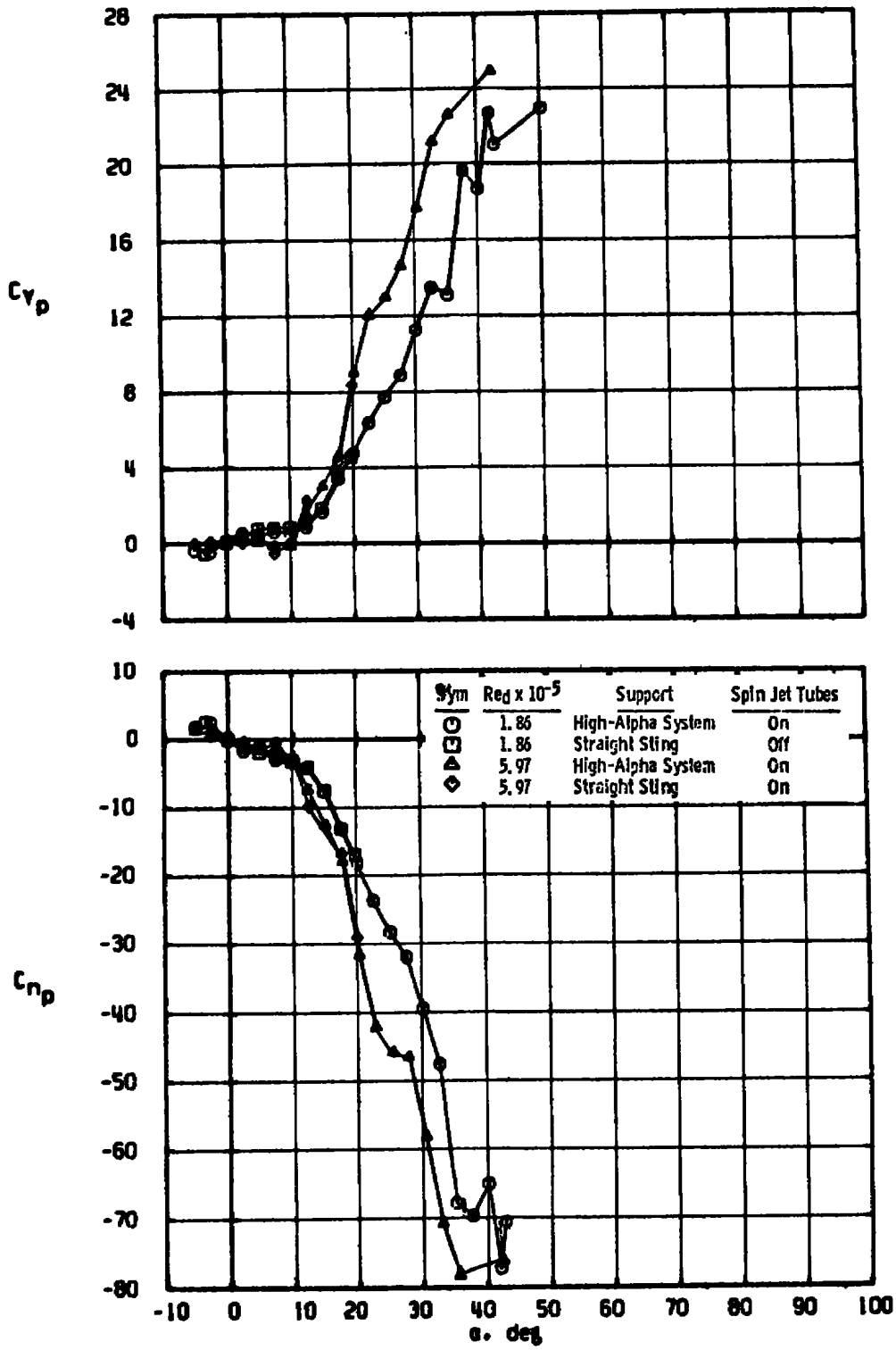

c. Effect of support system and Reynolds number, $M_\infty = 2.5$

Figure 15. Concluded.

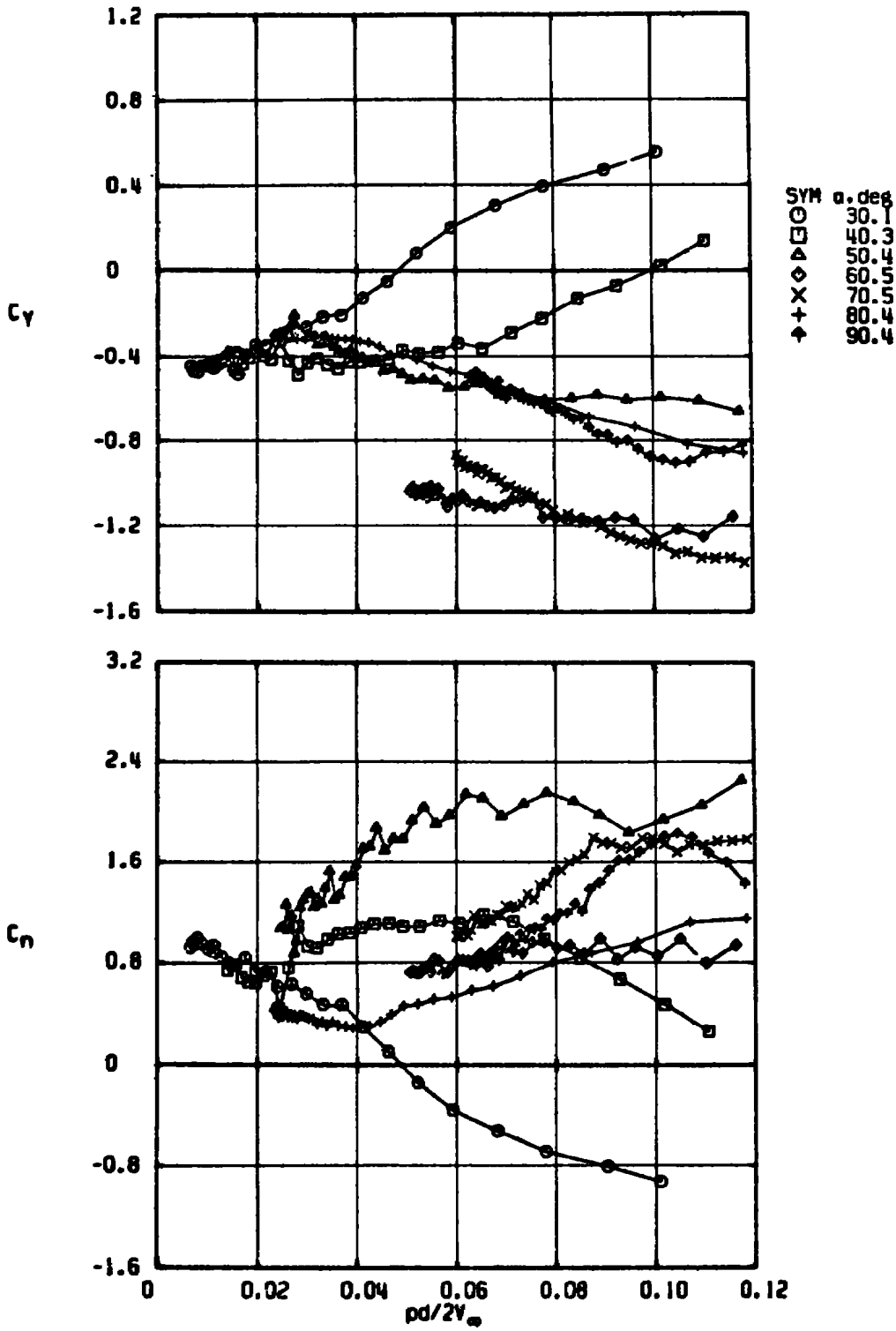

a. $M_\infty = 0.60$, $Re_d = 2.60 \times 10^5$

Figure 16. Magnus-force and moment characteristics of the Modified Basic Finner Model.

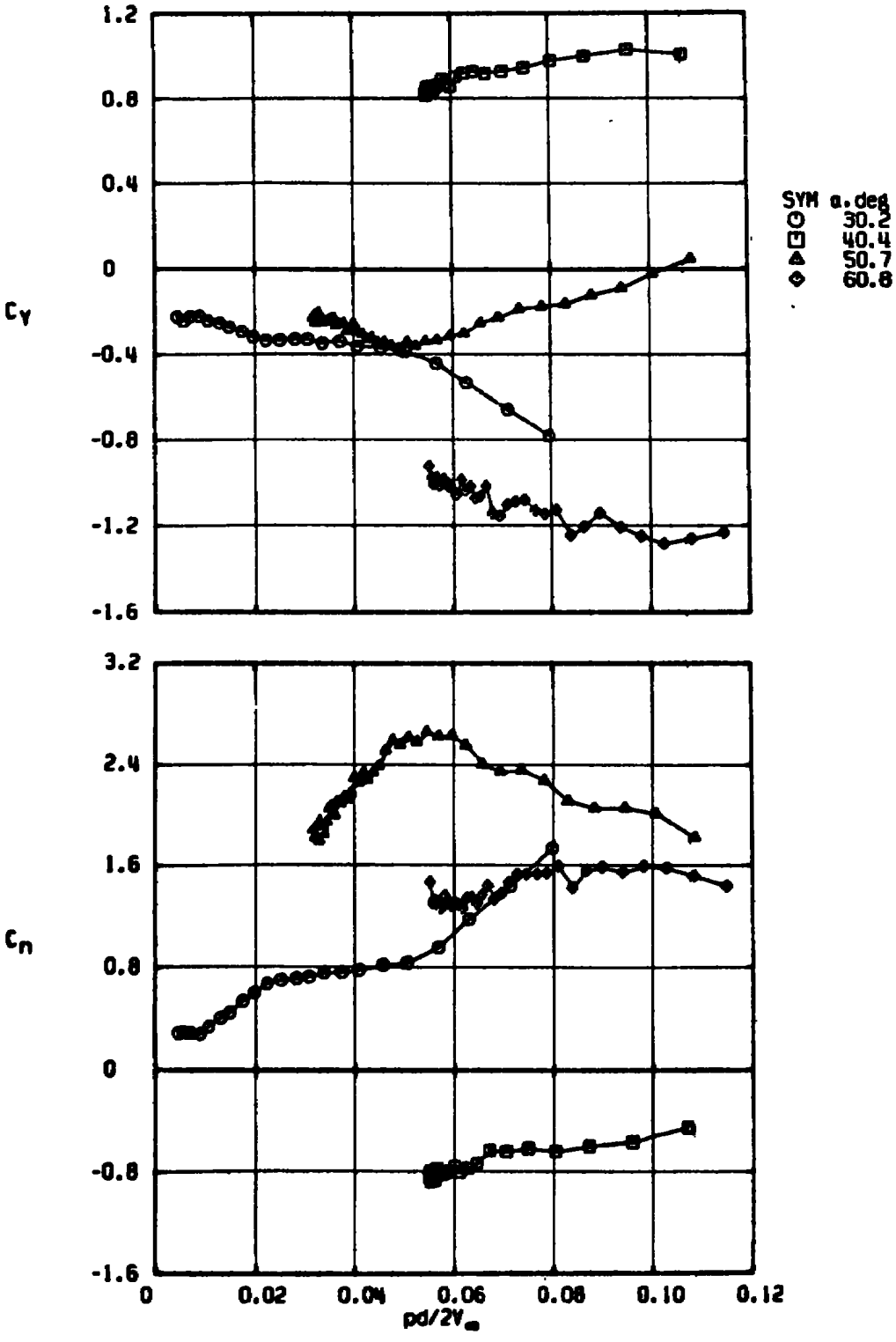

b. $M_\infty = 0.60$, $Re_d = 4.17 \times 10^5$

Figure 16. Continued.

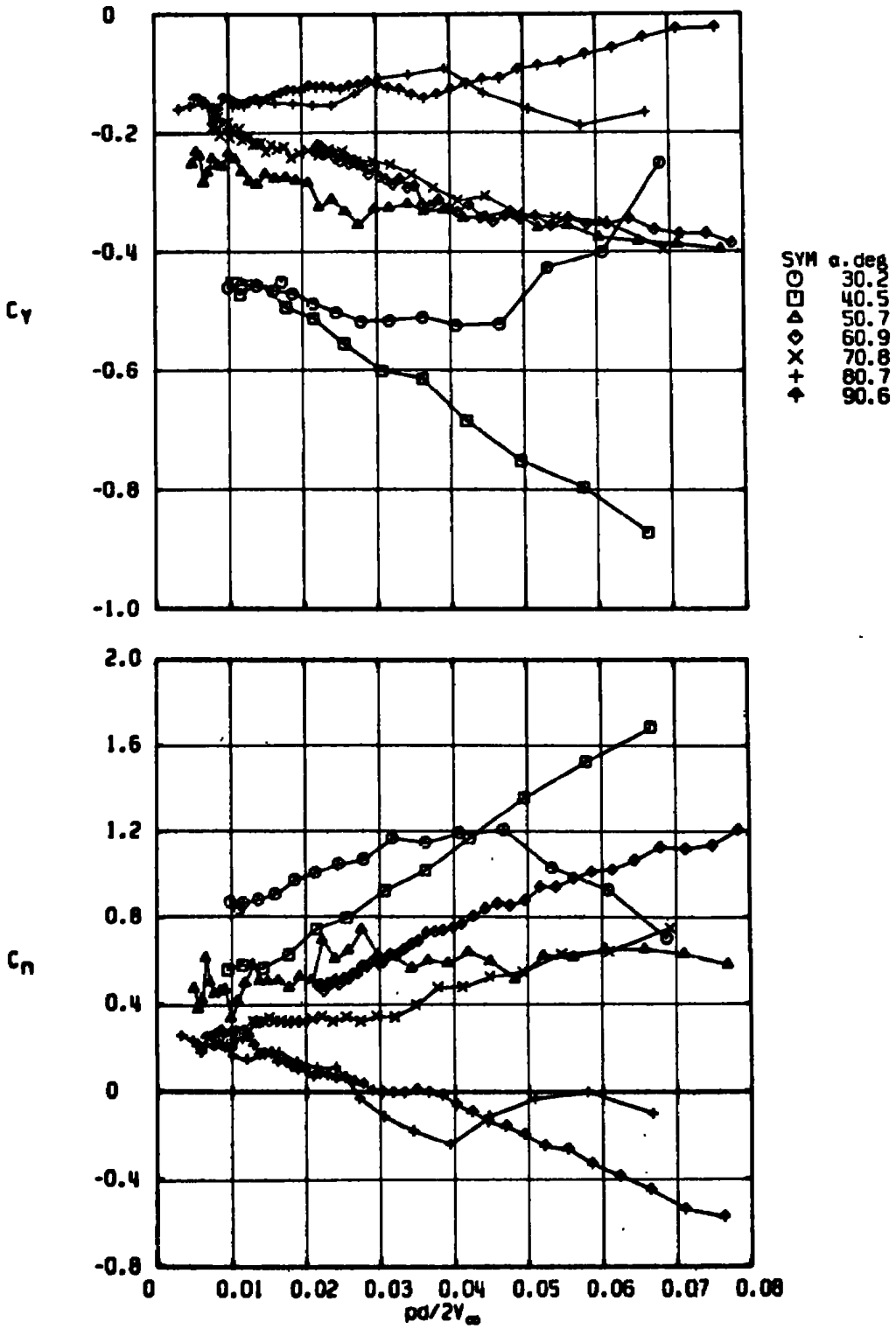

c. $M_\infty = 0.90$, $Re_d = 2.60 \times 10^5$

Figure 16. Continued.

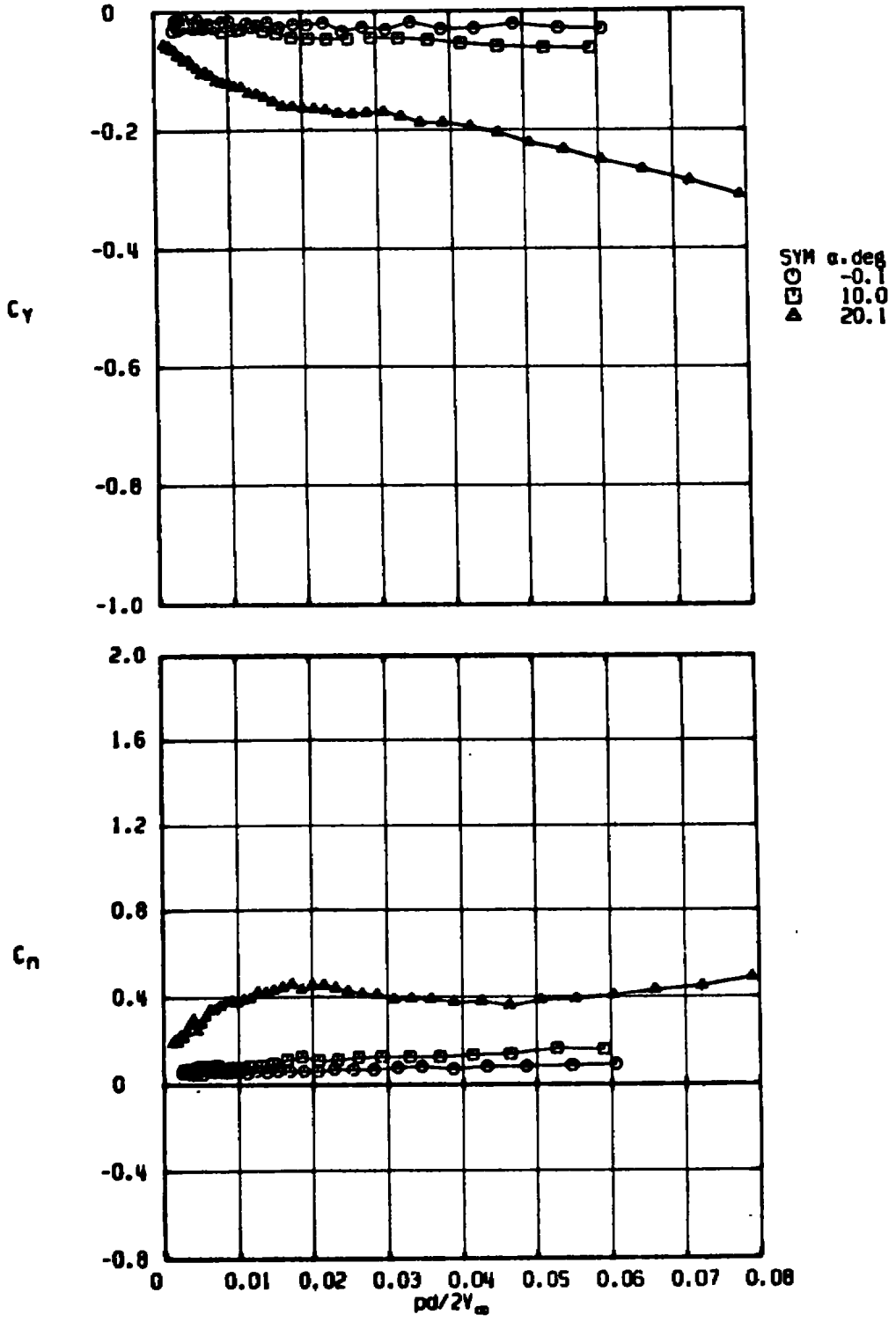

d. $M_\infty = 0.90$, $Re_d = 4.17 \times 10^5$

Figure 16. Continued.

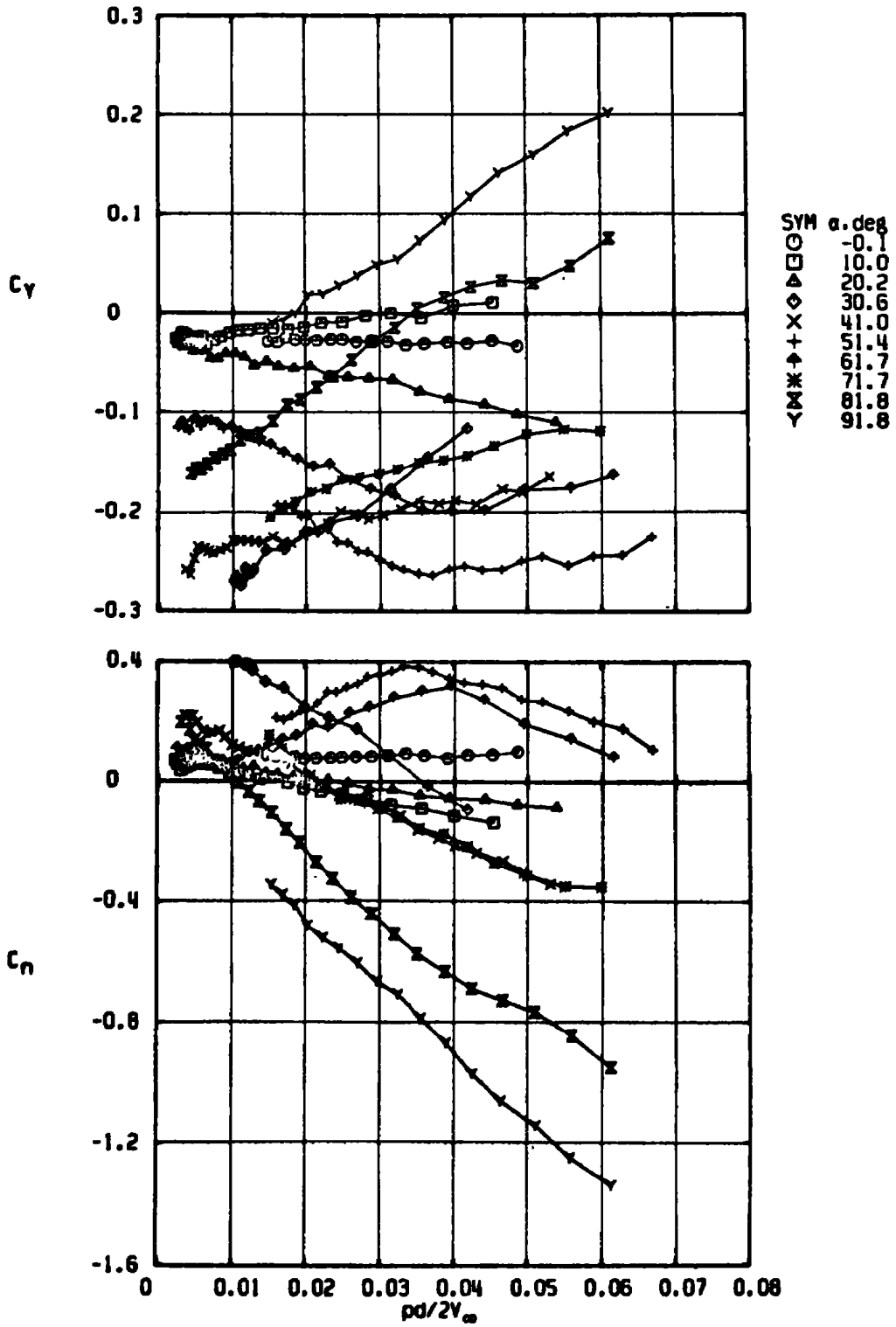

e. $M_\infty = 1.15$, $Re_d = 4.17 \times 10^5$

Figure 16. Continued.

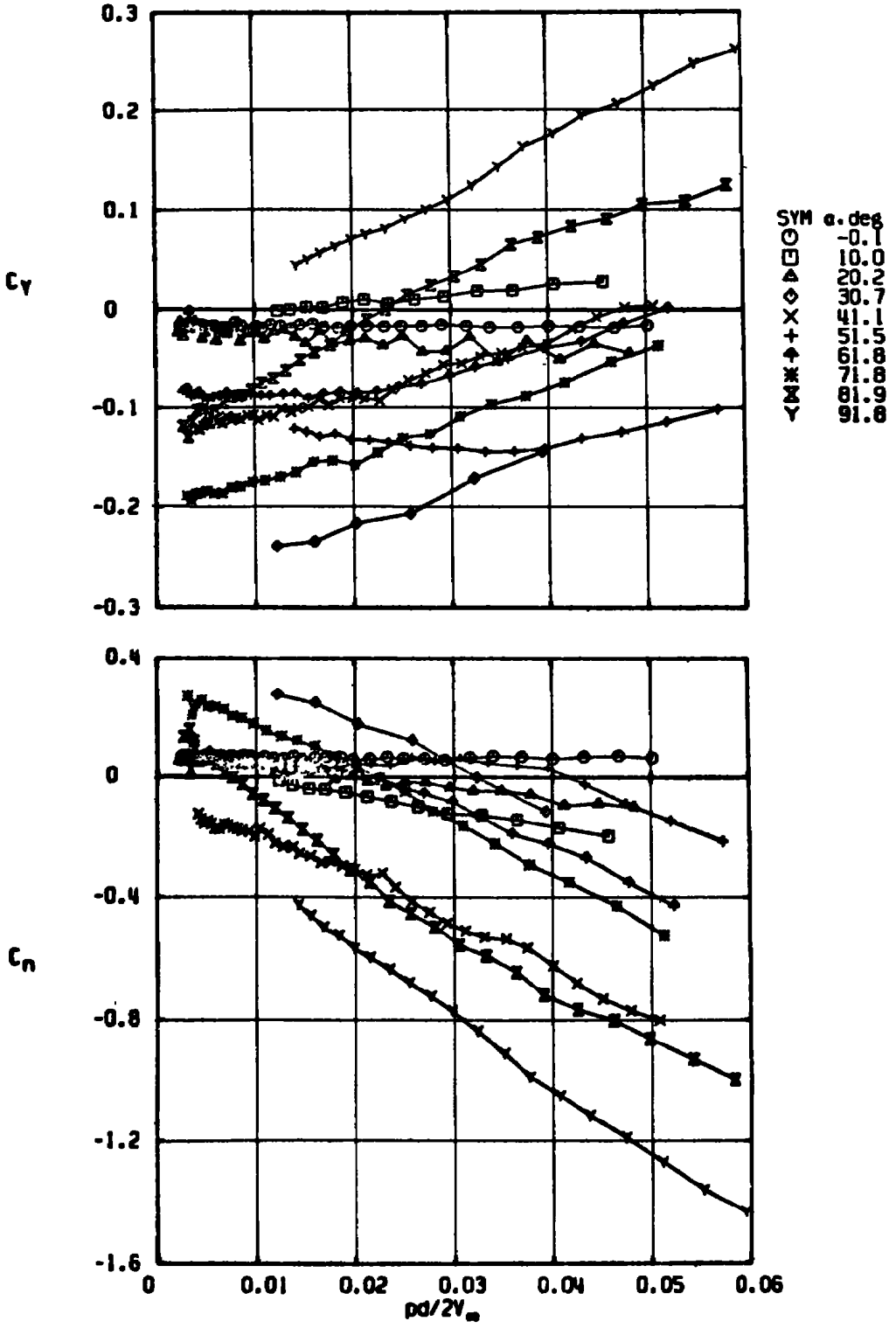

f. $M_\infty = 1.30$, $Re_d = 4.17 \times 10^5$

Figure 16. Continued.

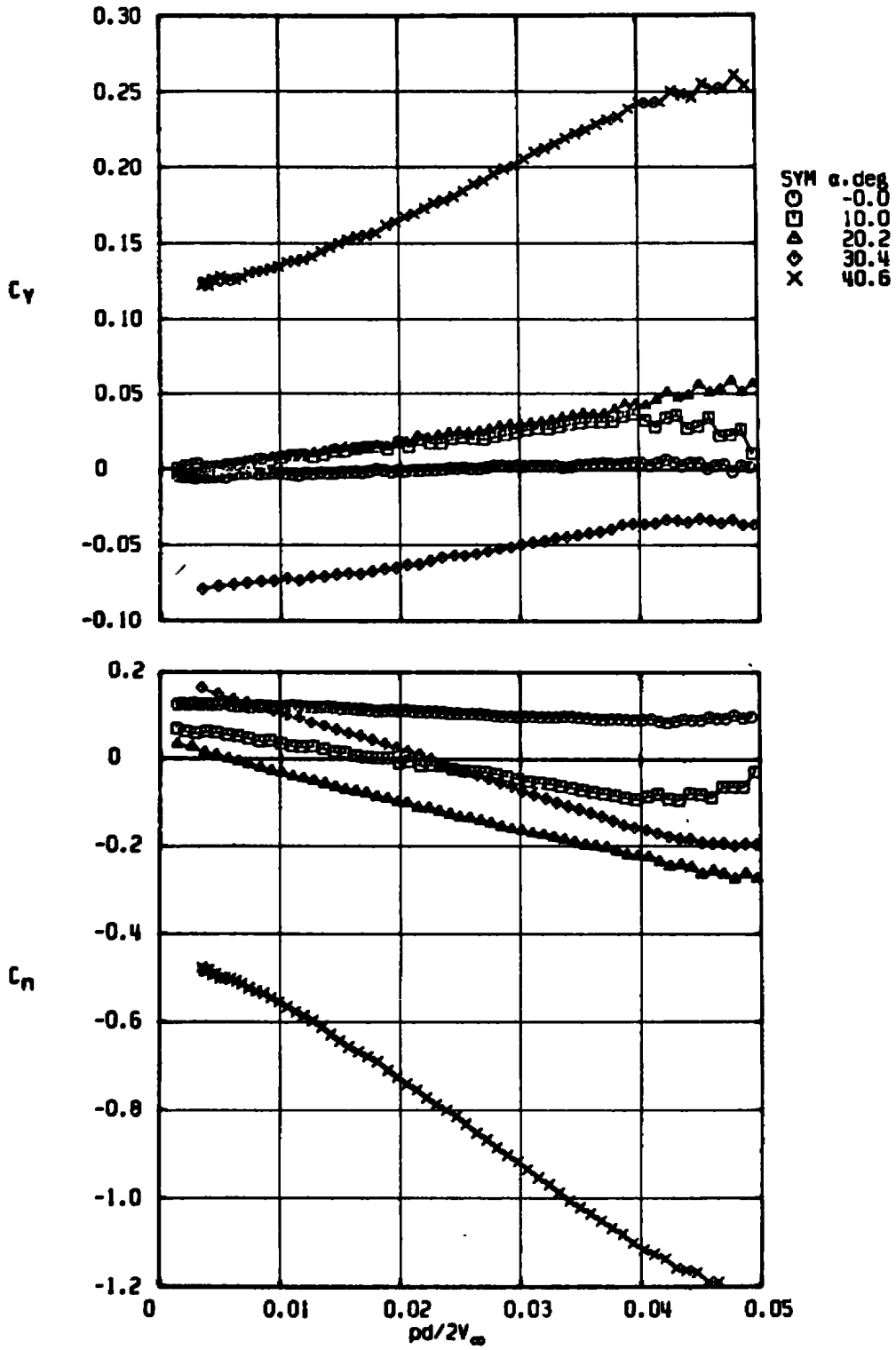

g. $M_\infty = 1.50$, $Re_d = 2.58 \times 10^5$

Figure 16. Continued.

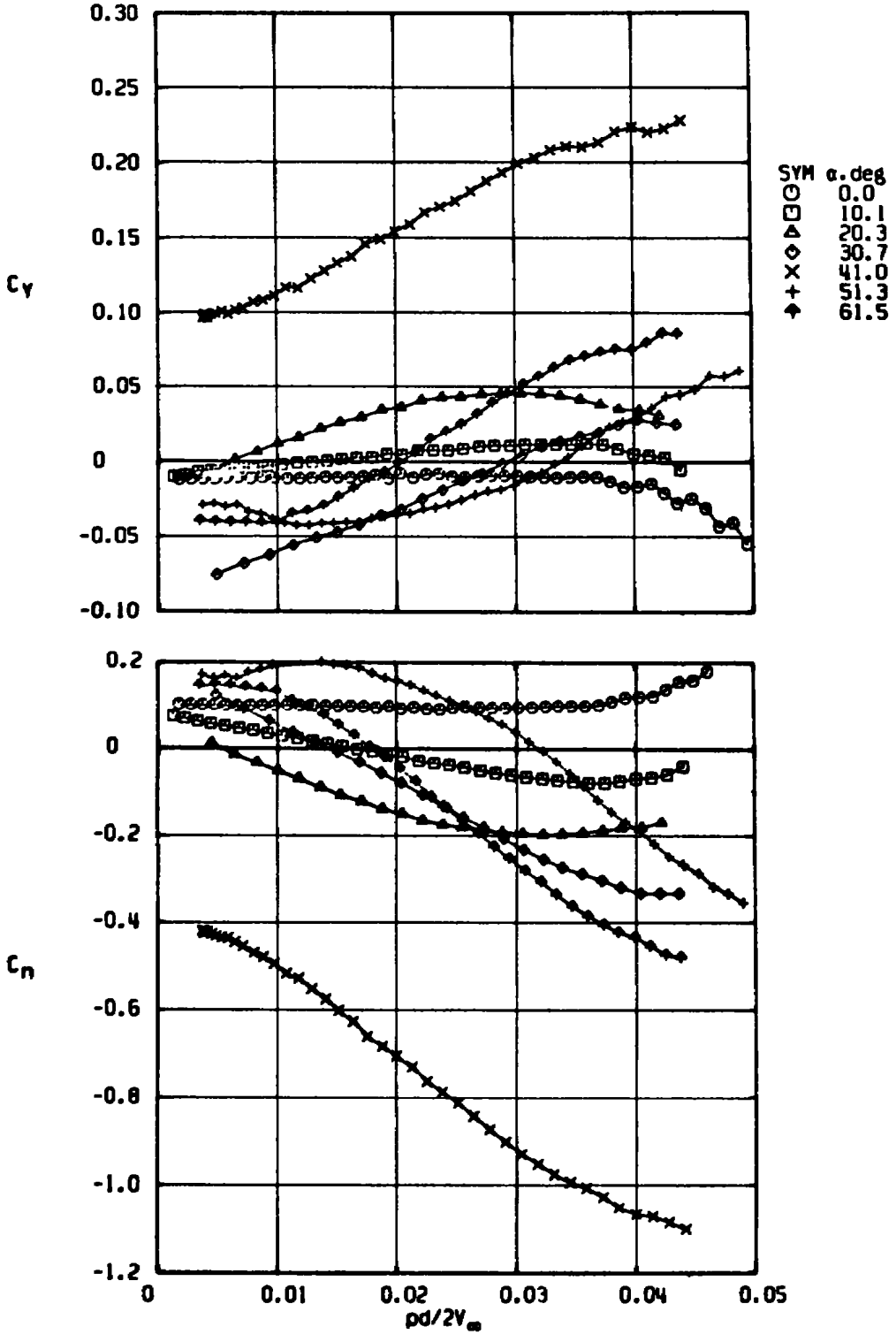

h. $M_\infty = 1.50$, $Re_d = 4.13 \times 10^5$

Figure 16. Continued.

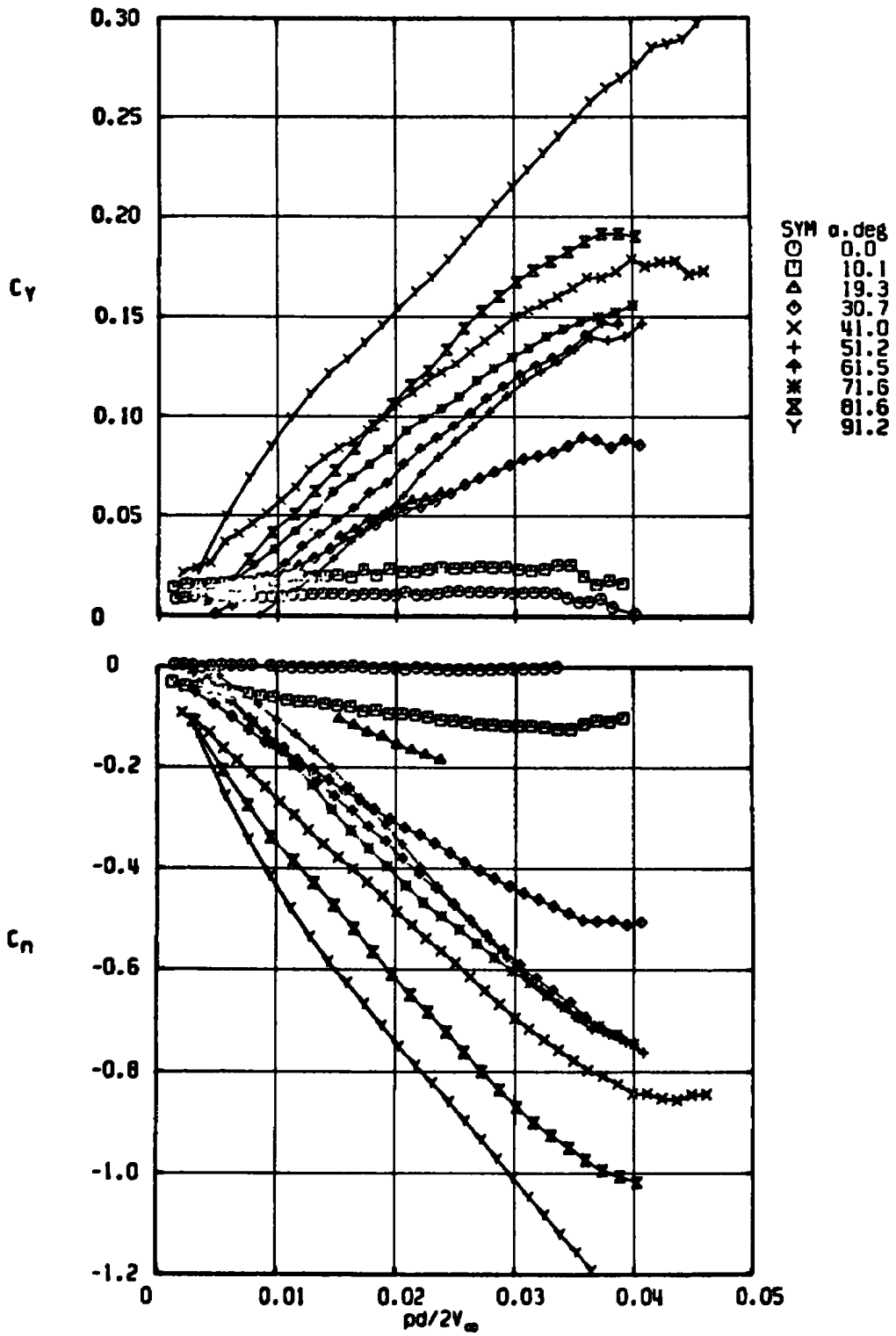

i. $M_\infty = 1.76$, $Re_d = 4.13 \times 10^5$

Figure 16. Continued.

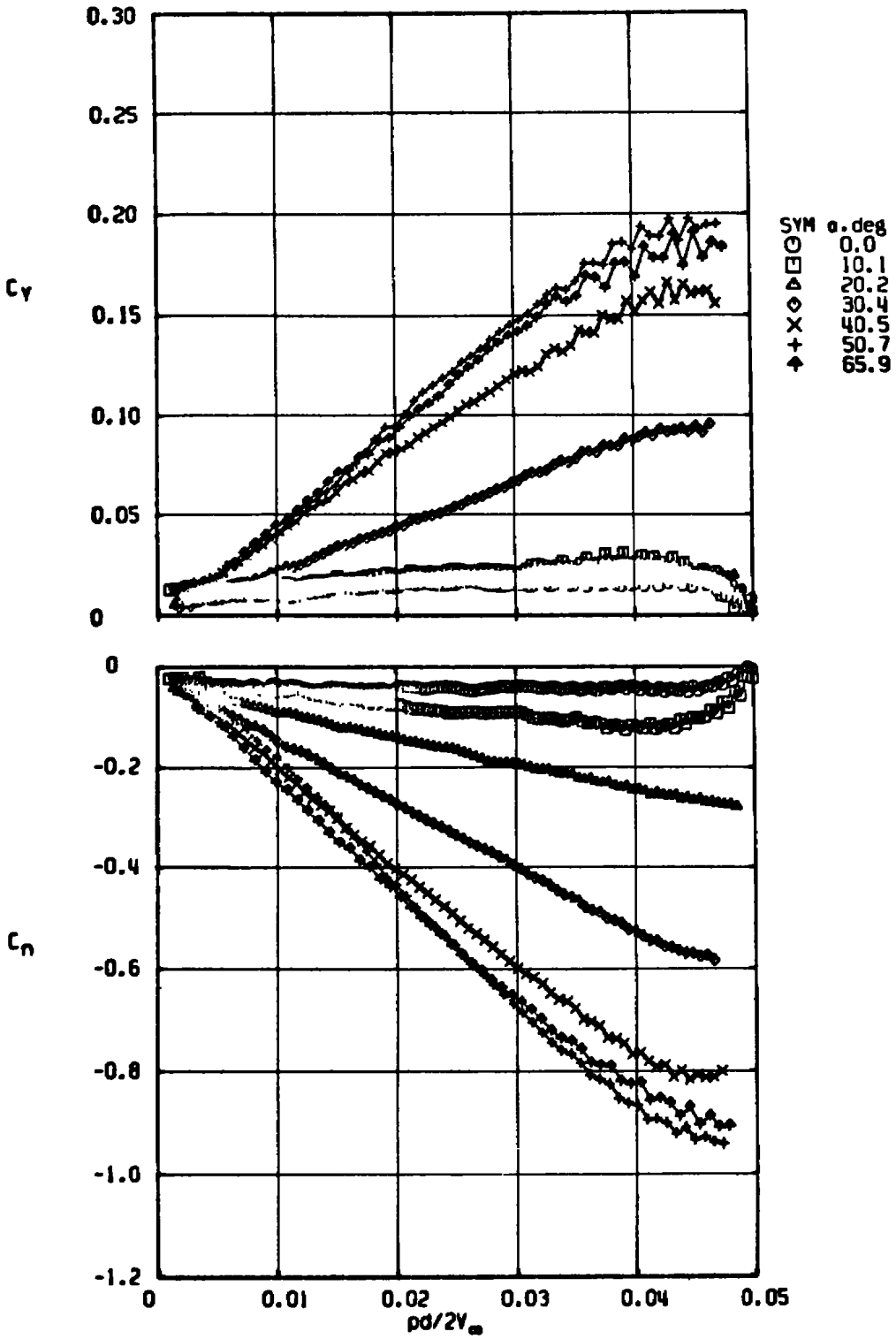

j. $M_\infty = 2.00$, $Re_d = 2.57 \times 10^5$

Figure 16. Continued.

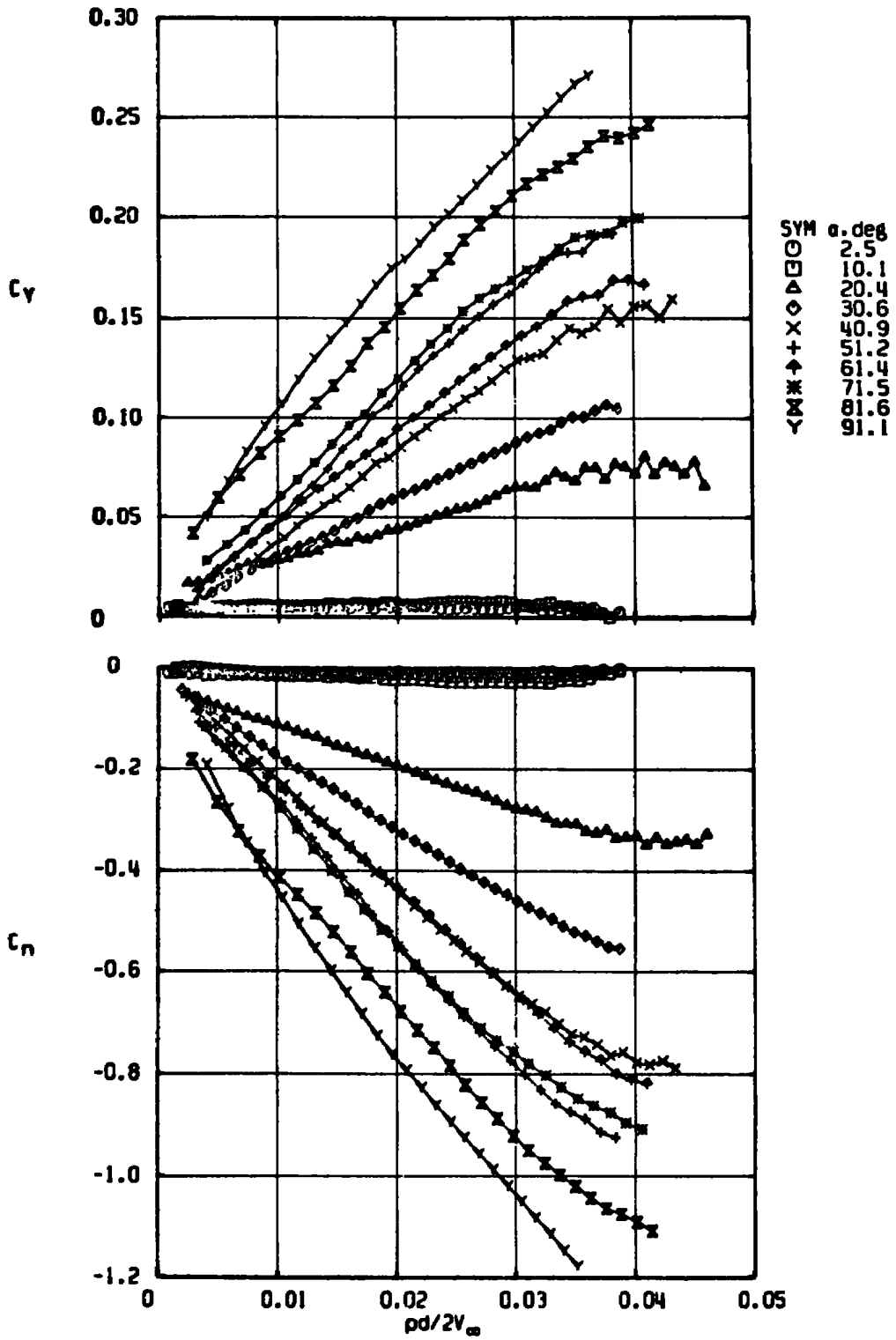

k. $M_\infty = 2.00$, $Re_d = 4.10 \times 10^5$

Figure 16. Continued.

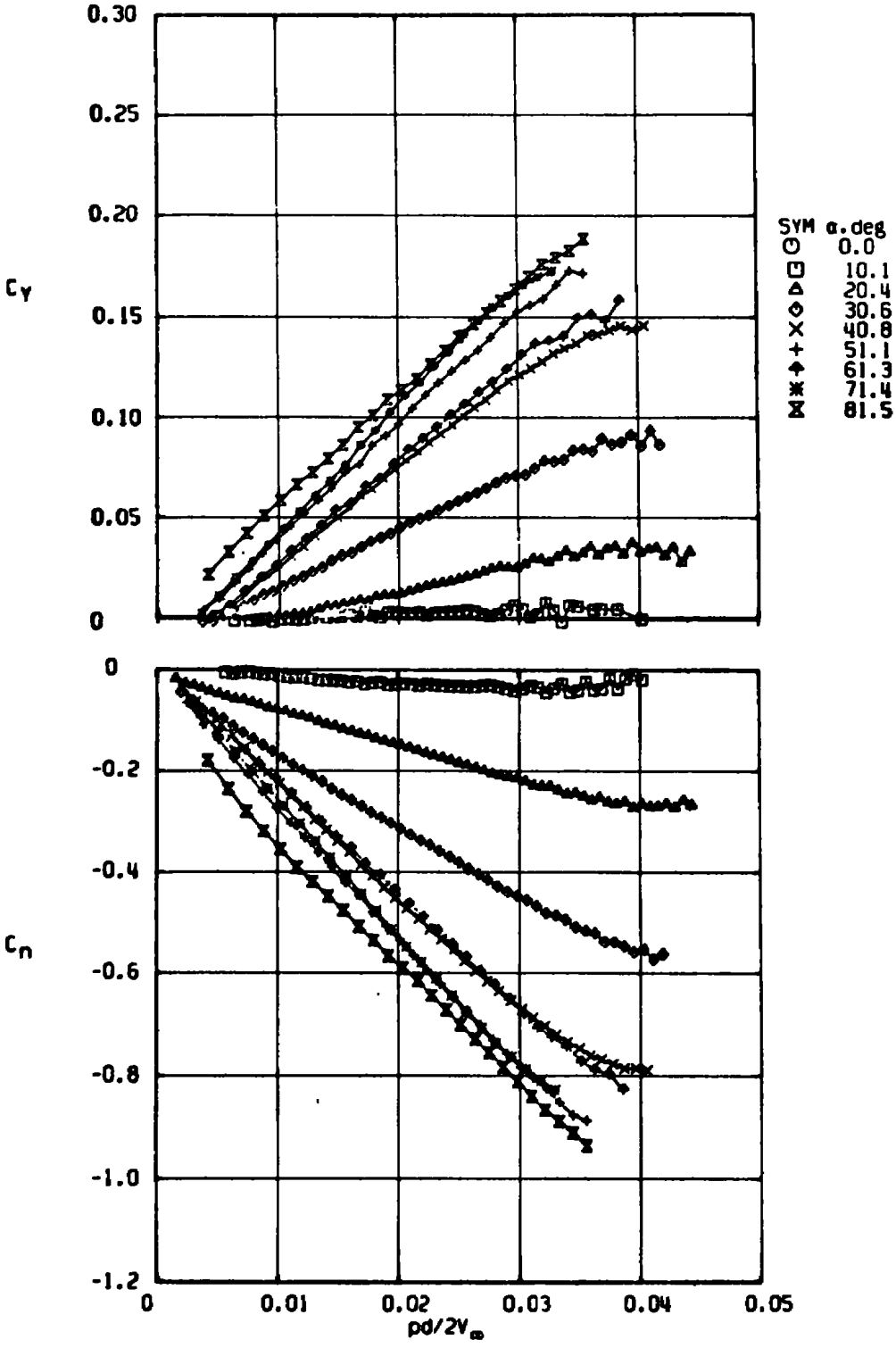

l. $M_\infty = 2.25$, $Re_d = 4.10 \times 10^5$

Figure 16. Continued.

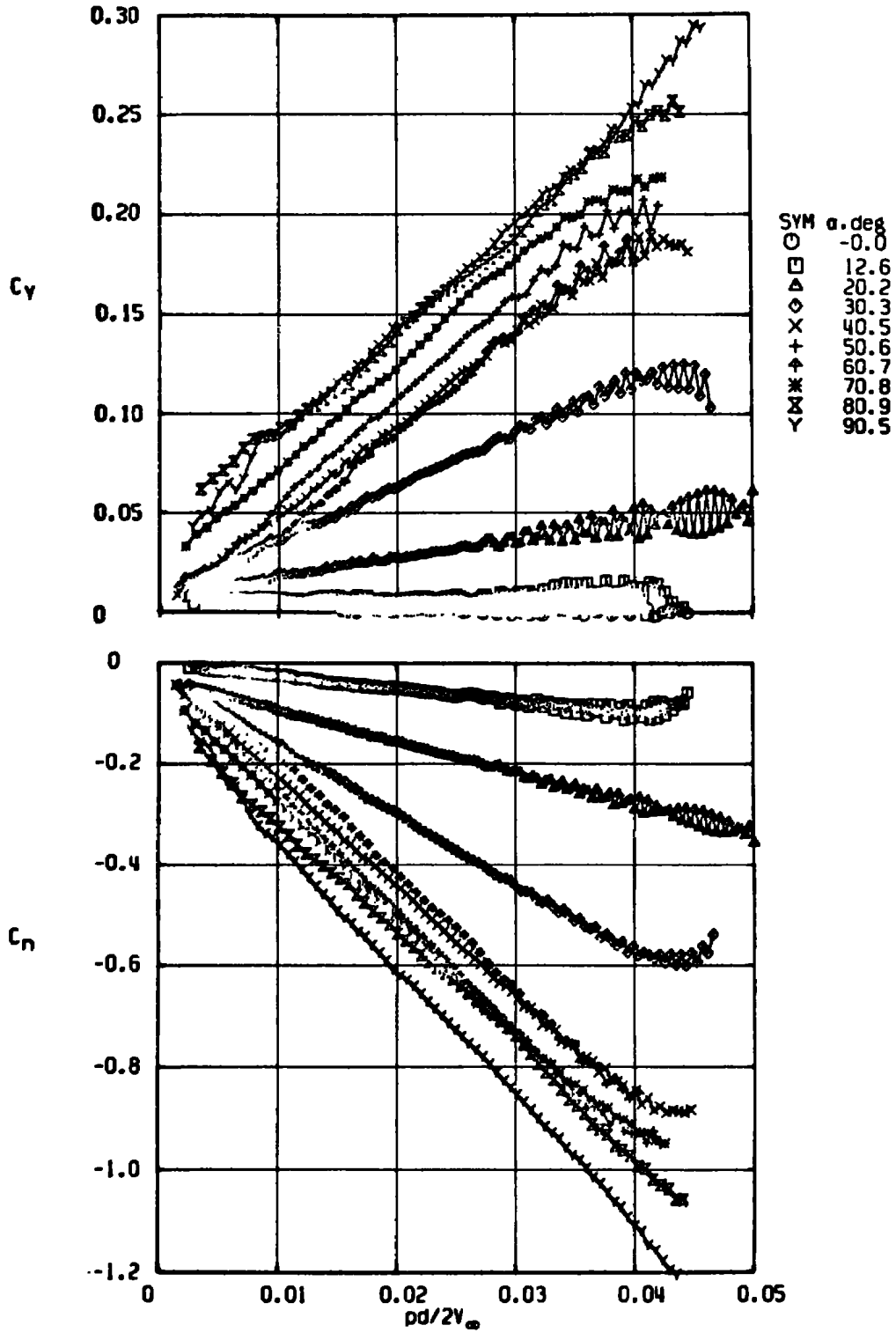

m. $M_\infty = 2.49$, $Re_d = 2.57 \times 10^5$

Figure 16. Continued.

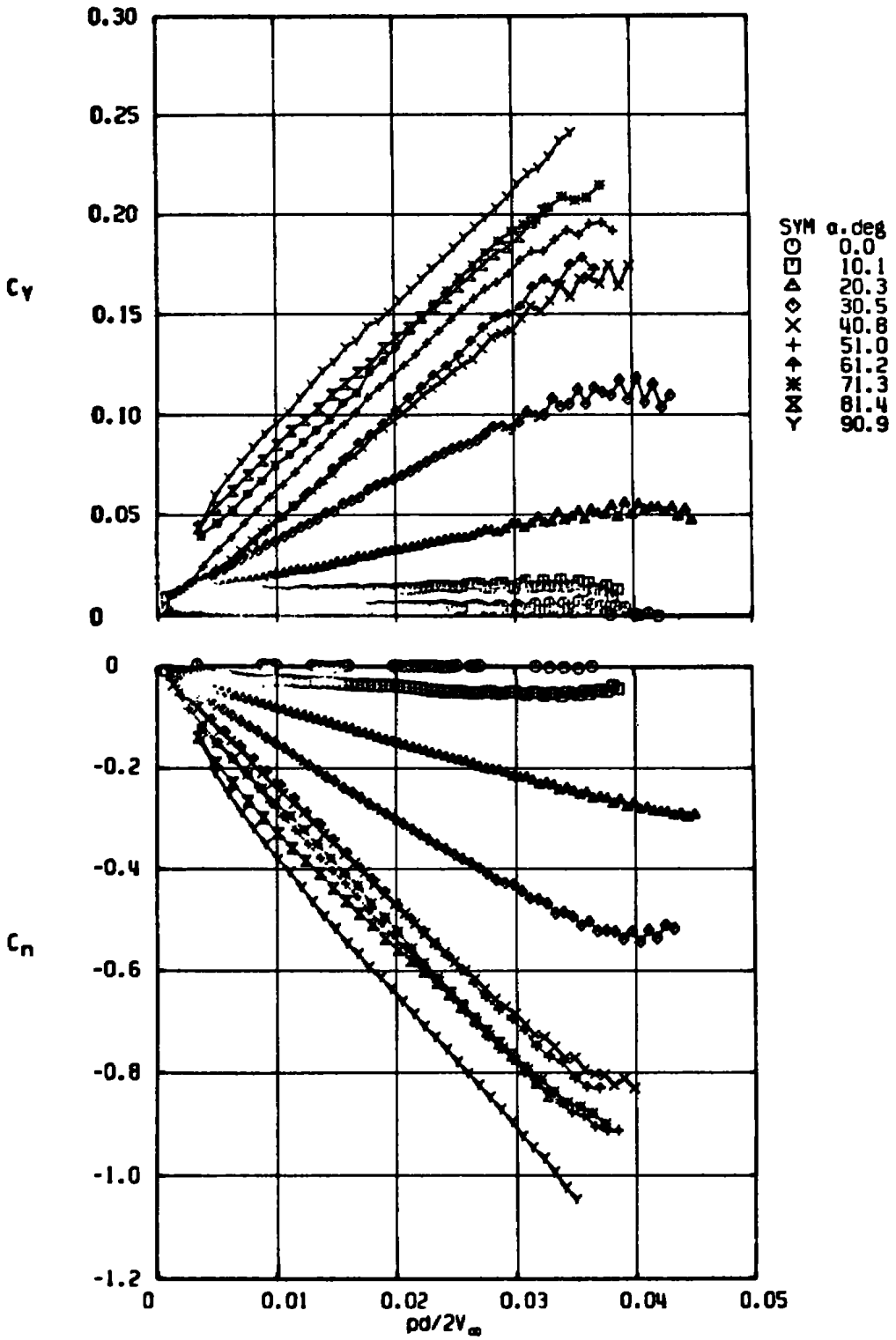

n. $M_\infty = 2.50$, $Re_d = 4.10 \times 10^5$

Figure 16. Concluded.

a. $M_\infty = 0.90$

Figure 17. Variation of C_{Y_p} and C_{n_p} with angle of attack for the Modified Basic Finner Model.

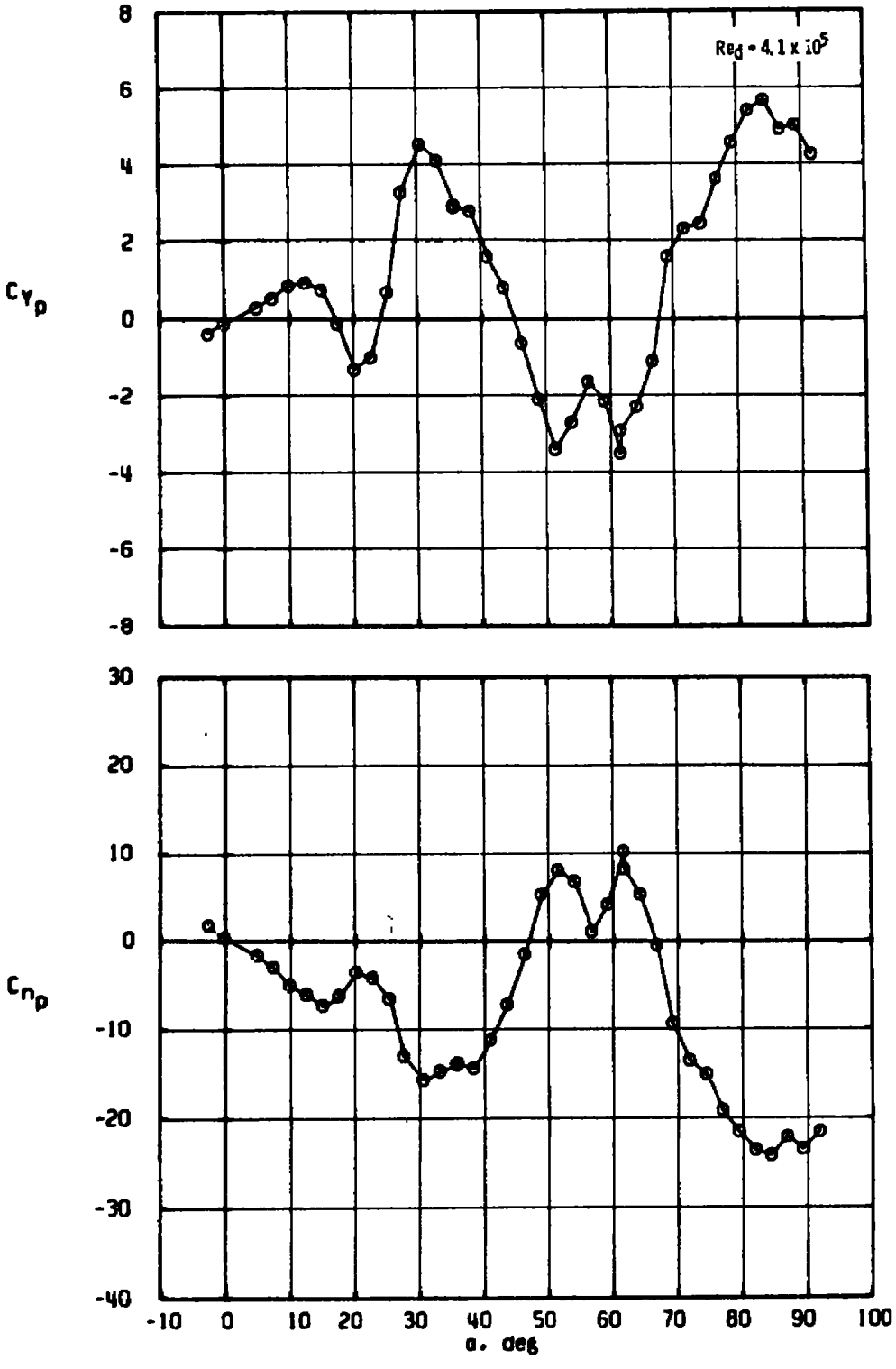

b. $M_\infty = 1.15$

Figure 17. Continued.

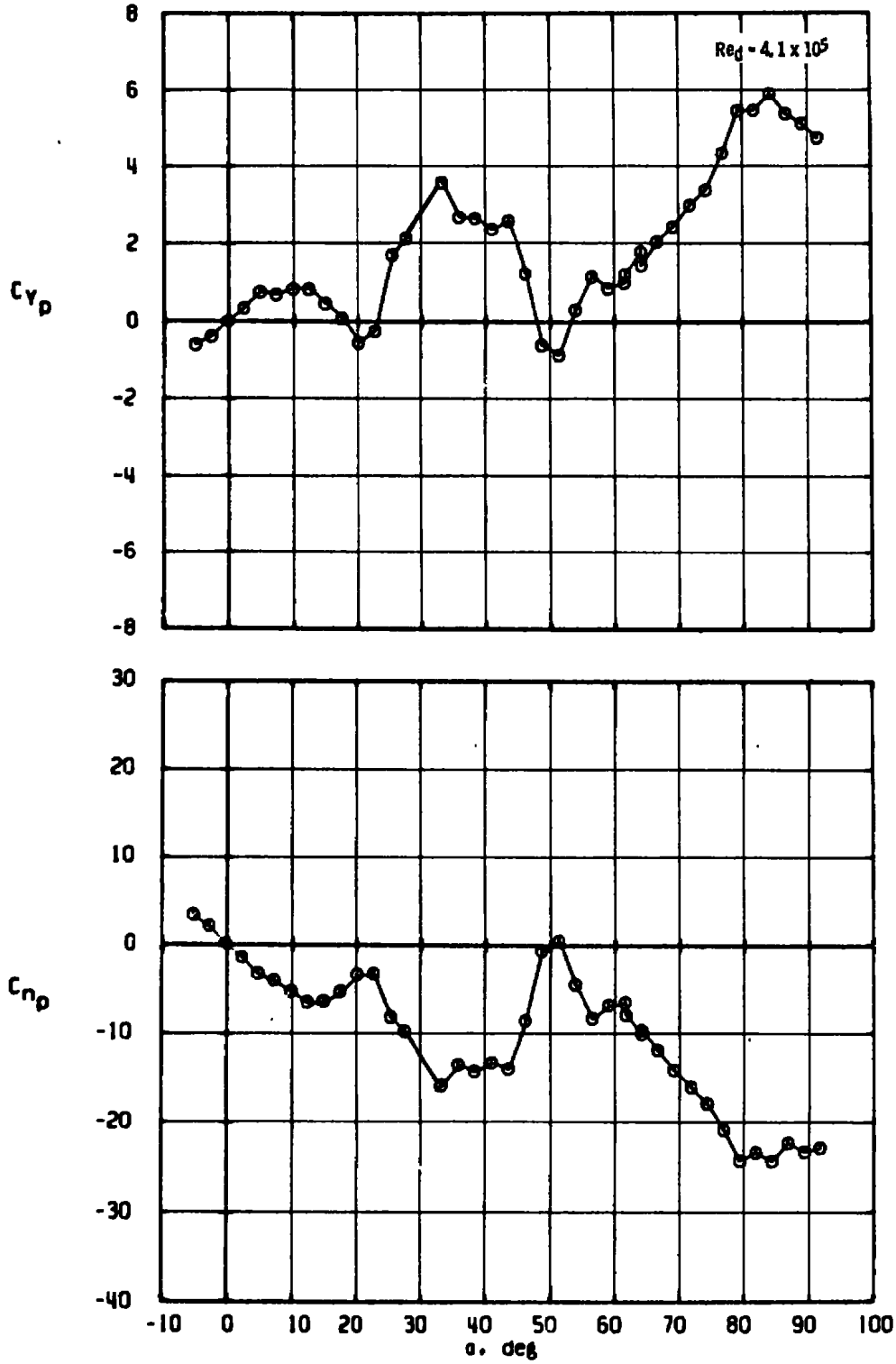

c. $M_\infty = 1.30$

Figure 17. Continued.

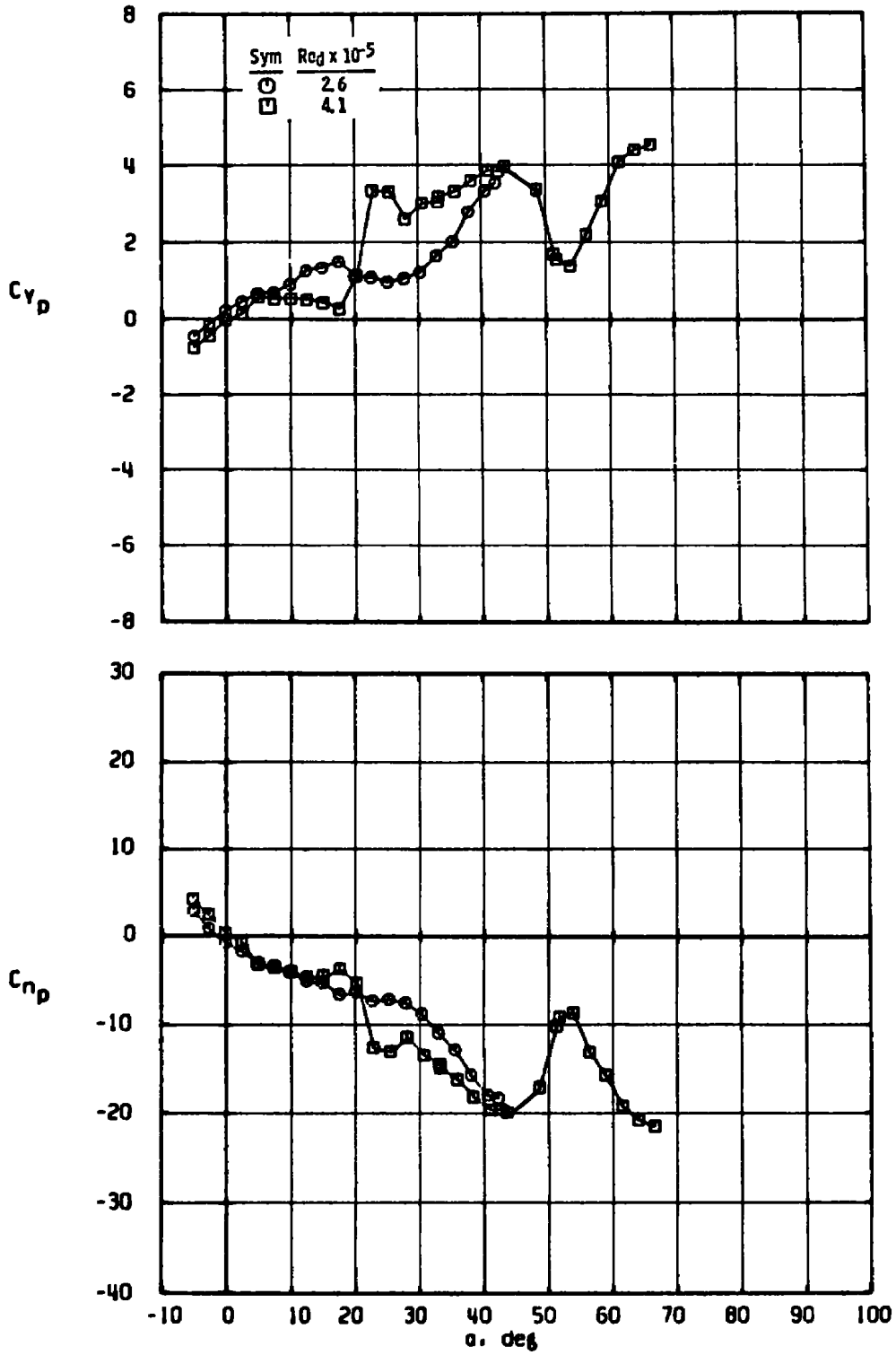

d. $M_\infty = 1.50$

Figure 17. Continued

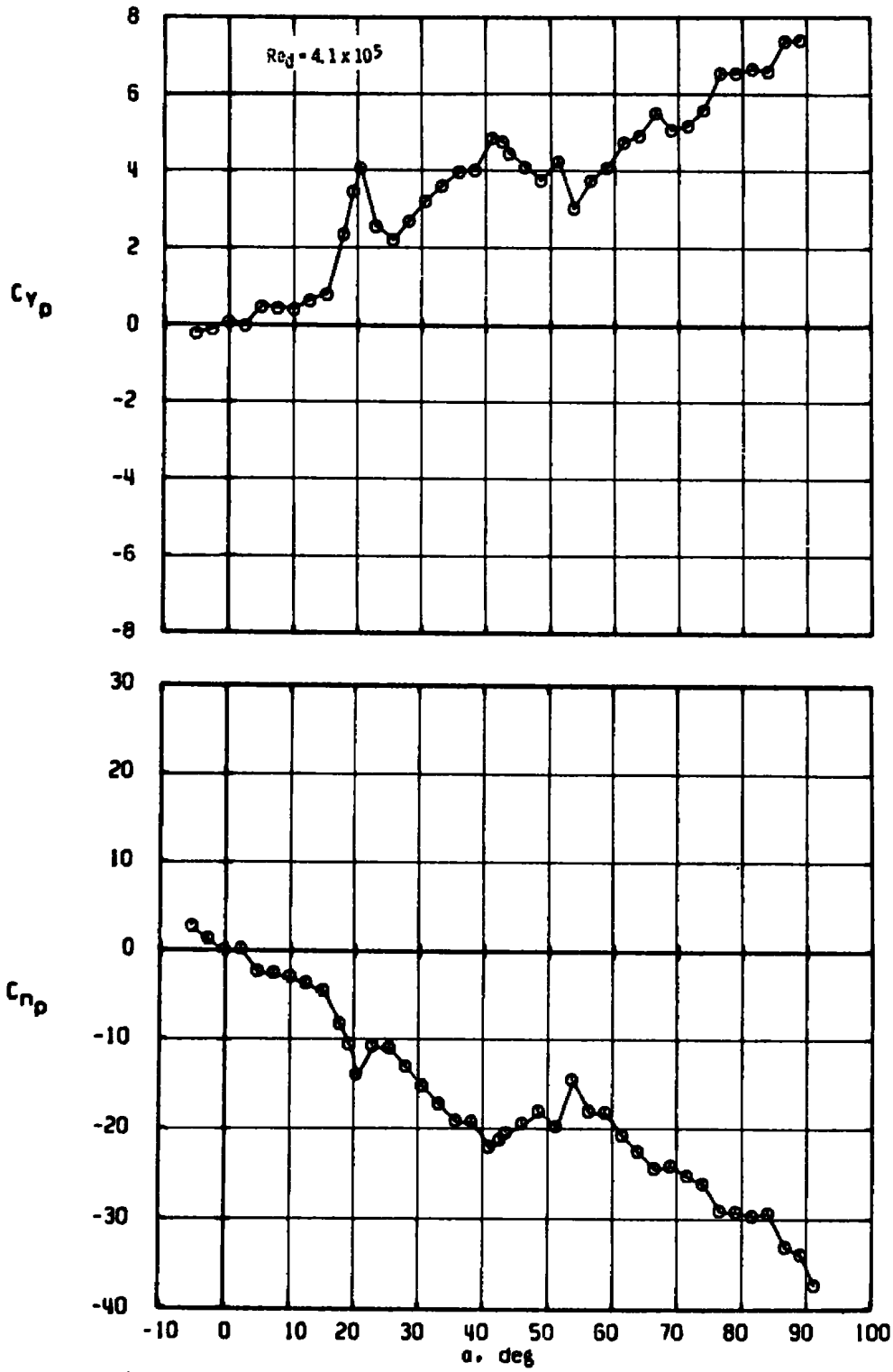

e. $M_\infty = 1.76$

Figure 17. Continued.

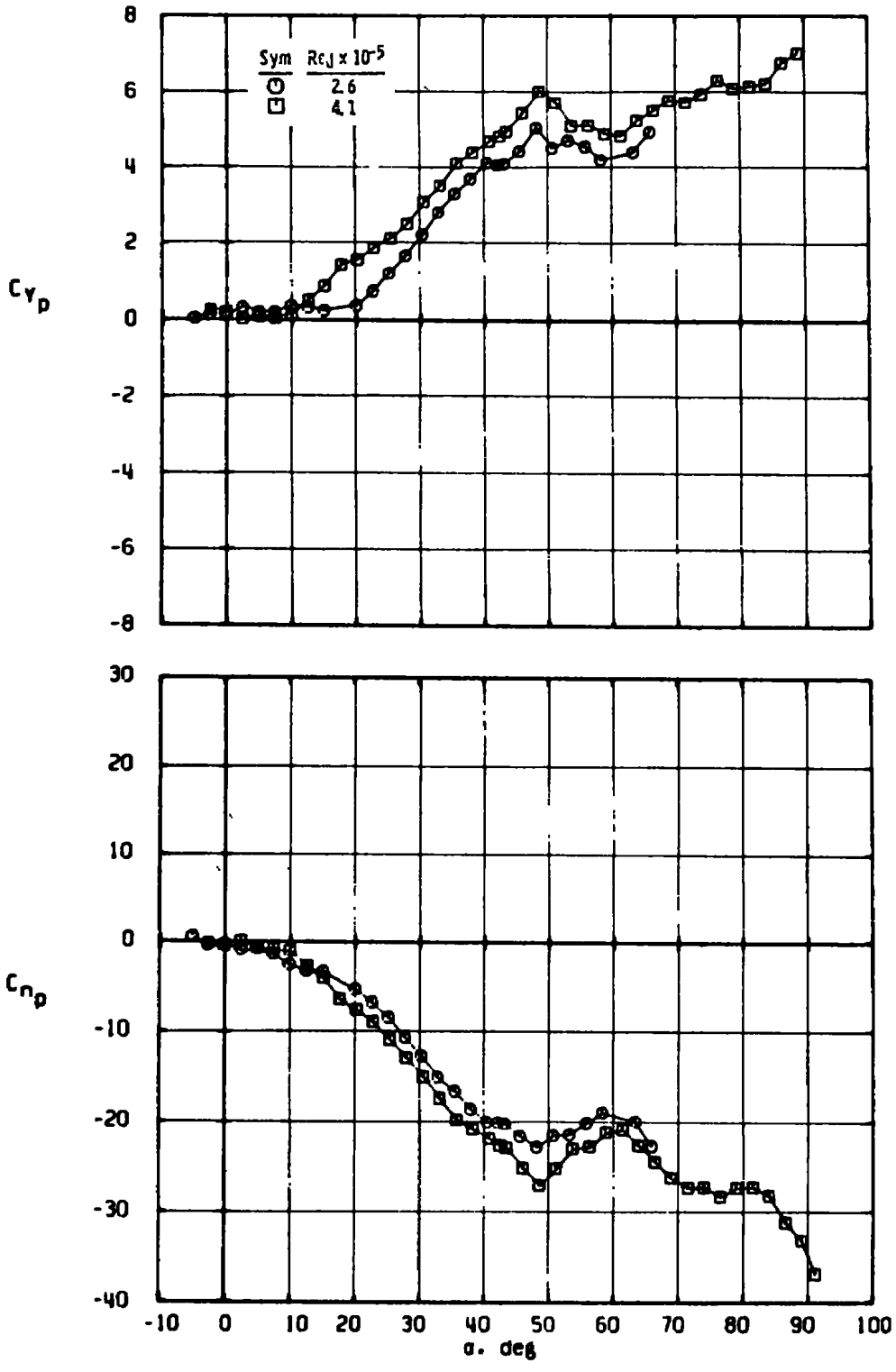

f. M_∞ = 2.00

Figure 17. Continued.

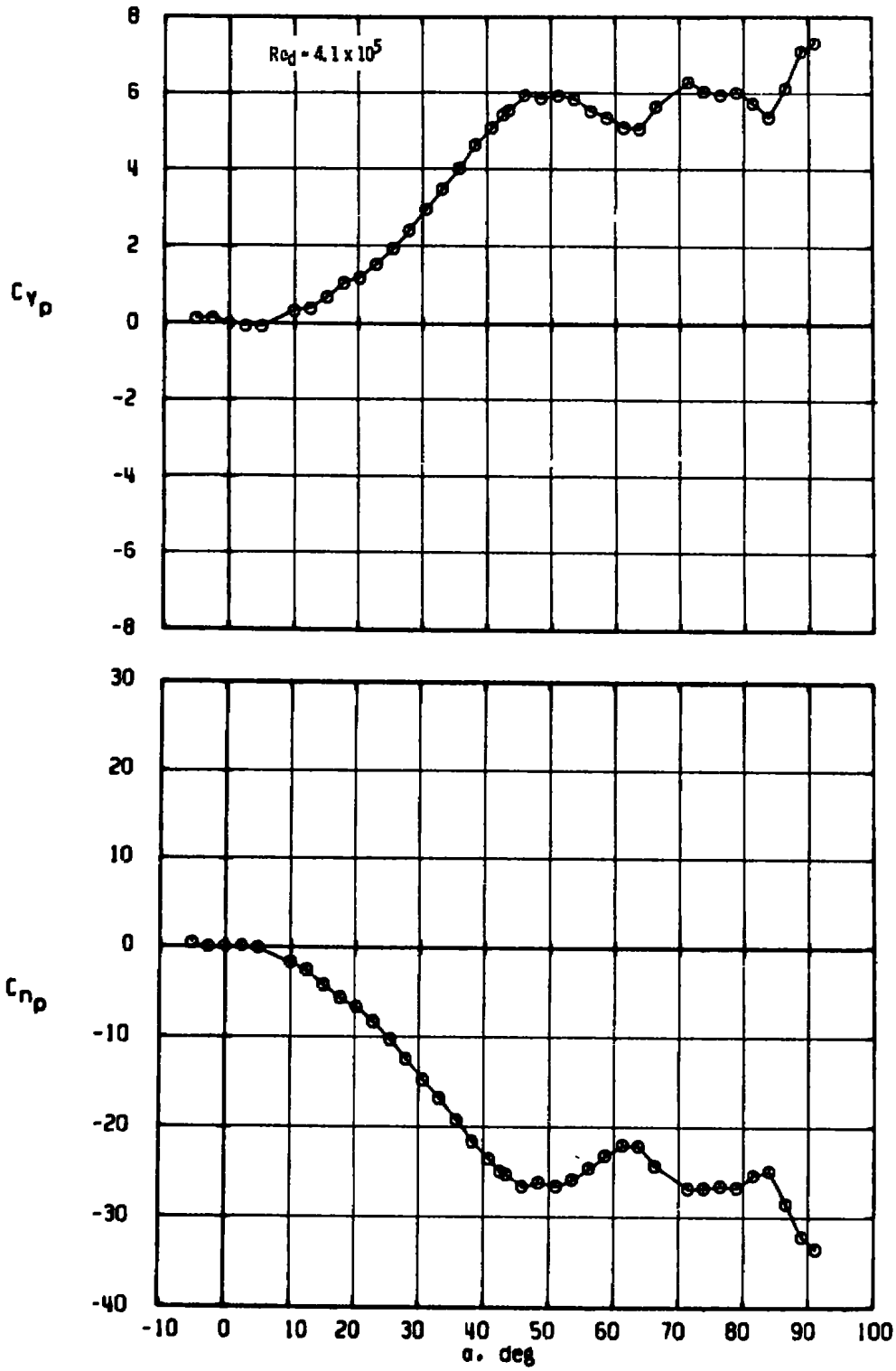

g. $M_\infty = 2.25$

Figure 17. Continued.

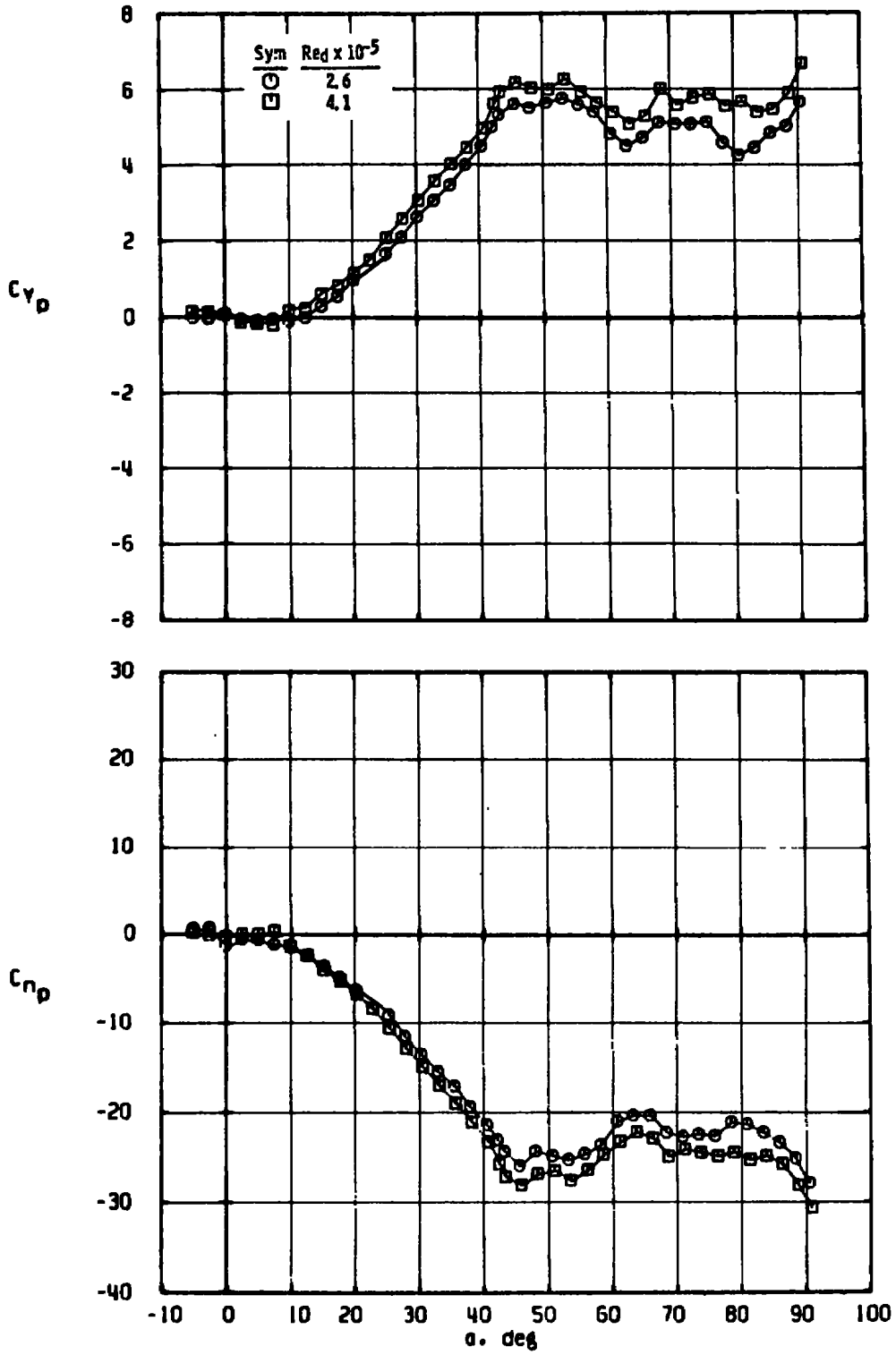

h. $M_\infty = 2.50$

Figure 17. Concluded.

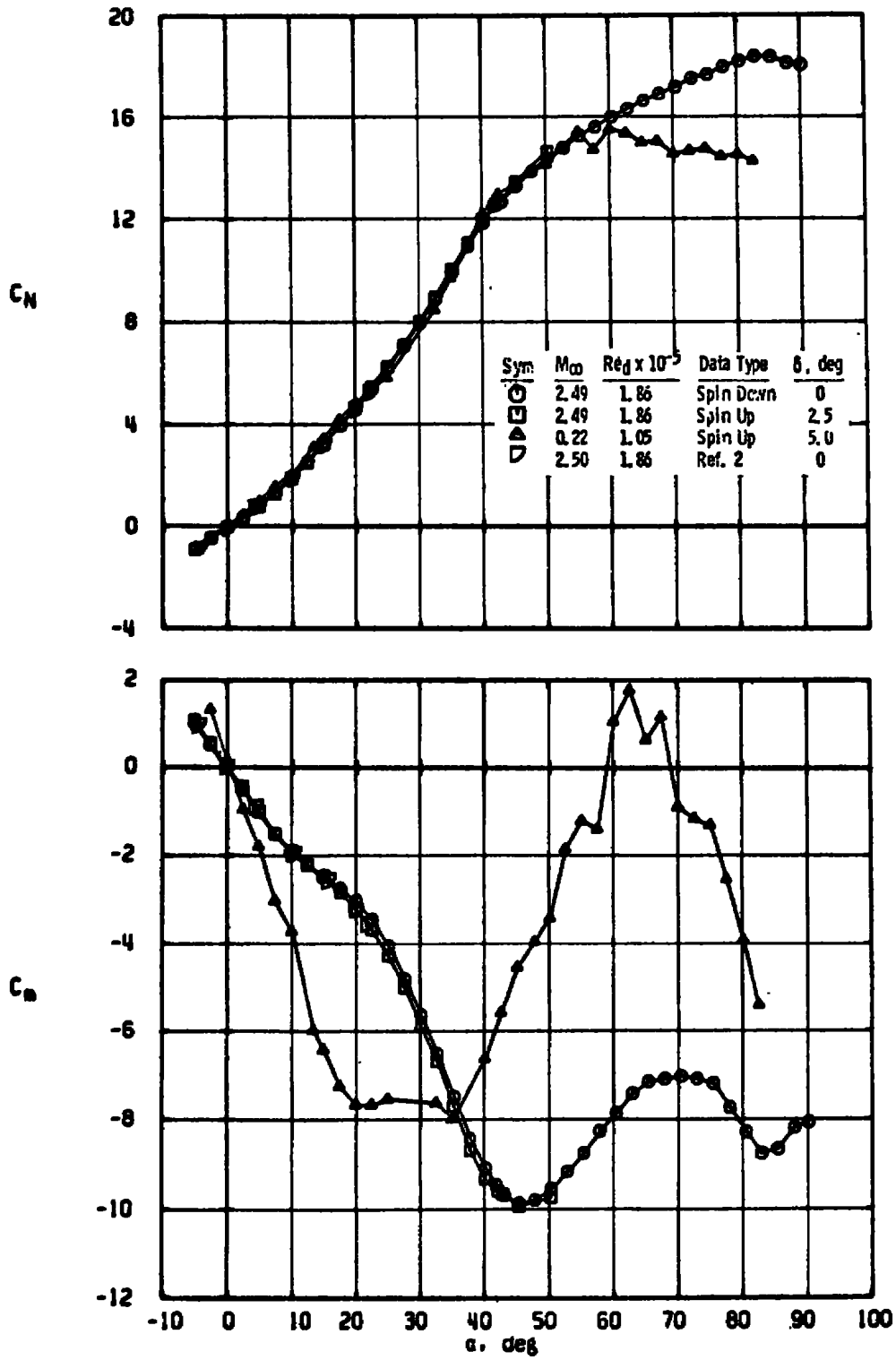

a. Effect of Mach number

Figure 18. Static longitudinal stability characteristics of the Basic Finner Model, p ≈ 100 radians/sec.

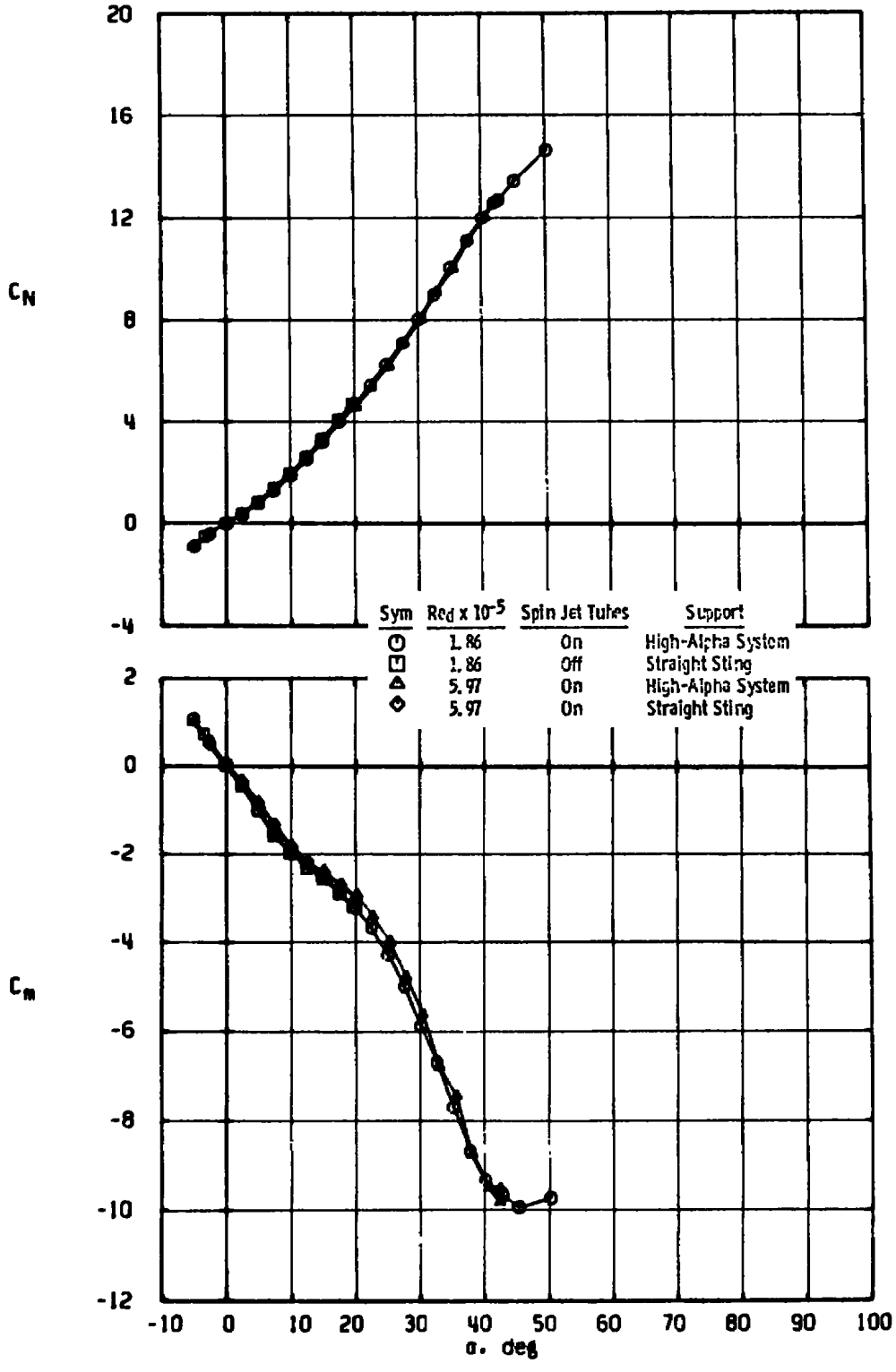

b. Effects of support system and Reynolds number, M_∞ = 2.5

Figure 18. Concluded.

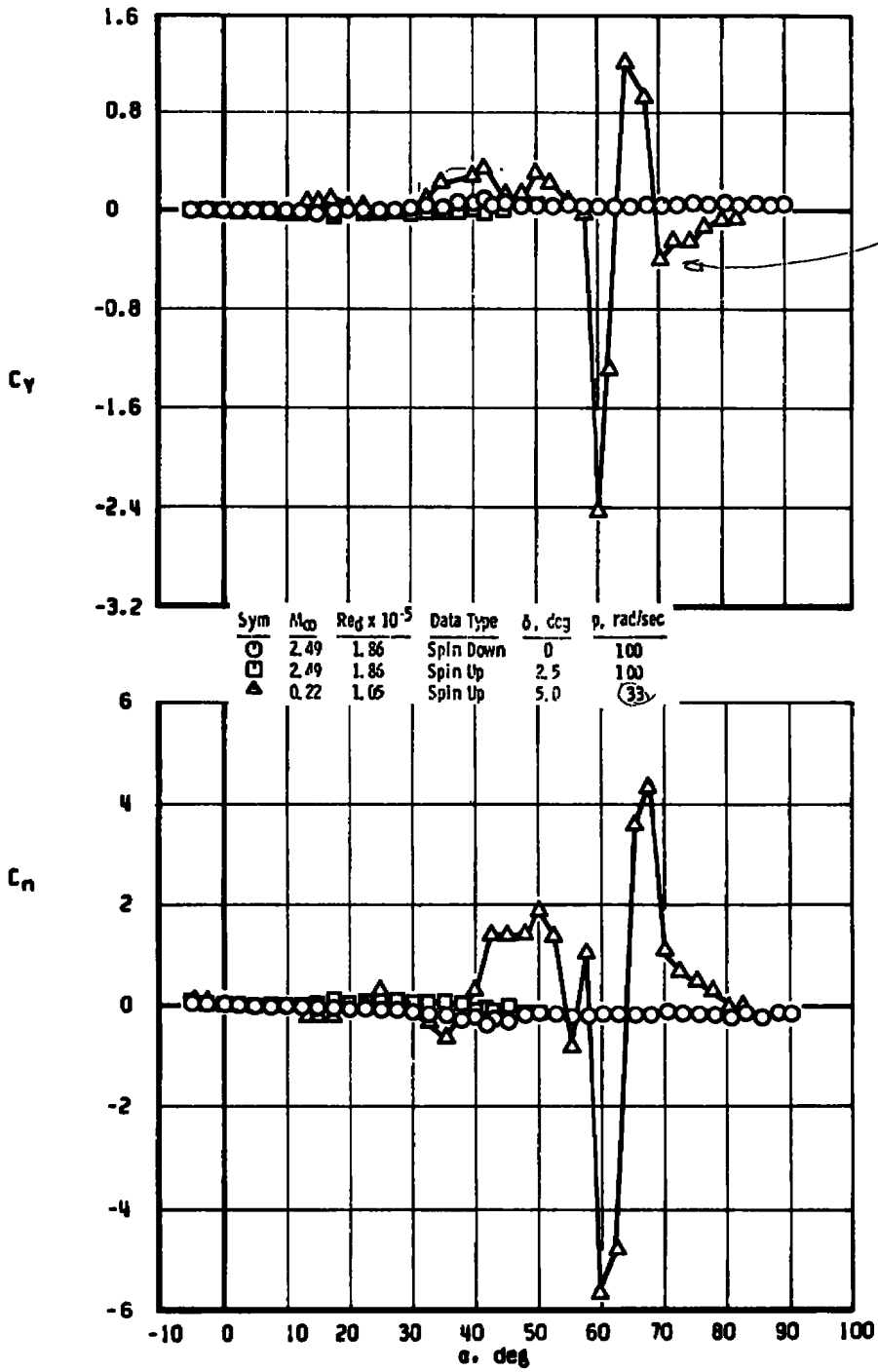

a. Effect of Mach number

Figure 19. Variation in directional stability with angle of attack for the Basic Finner Model.

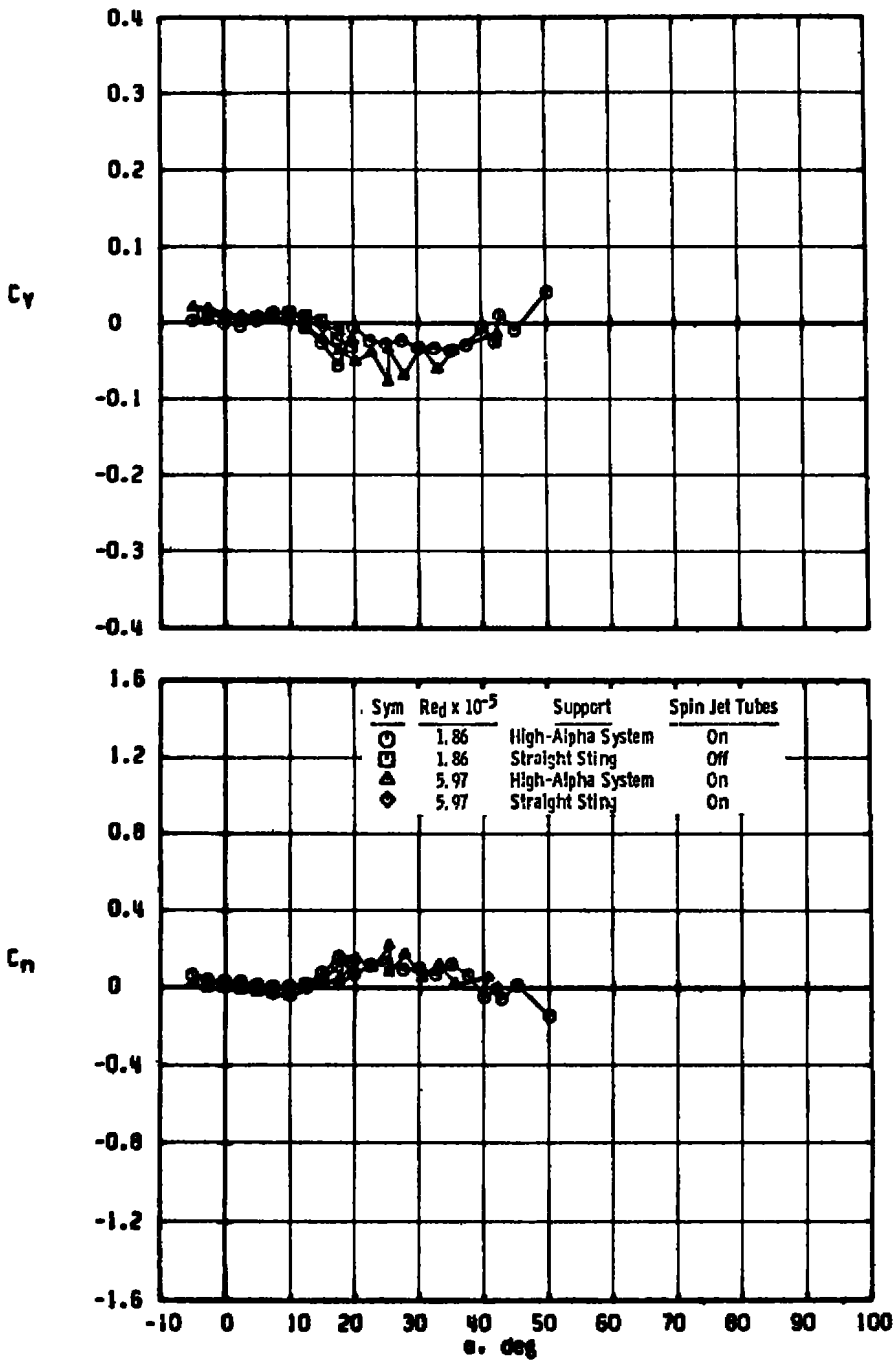

b. Effects of support system and Reynolds number, $M_\infty = 2.5$
Figure 19. Concluded.

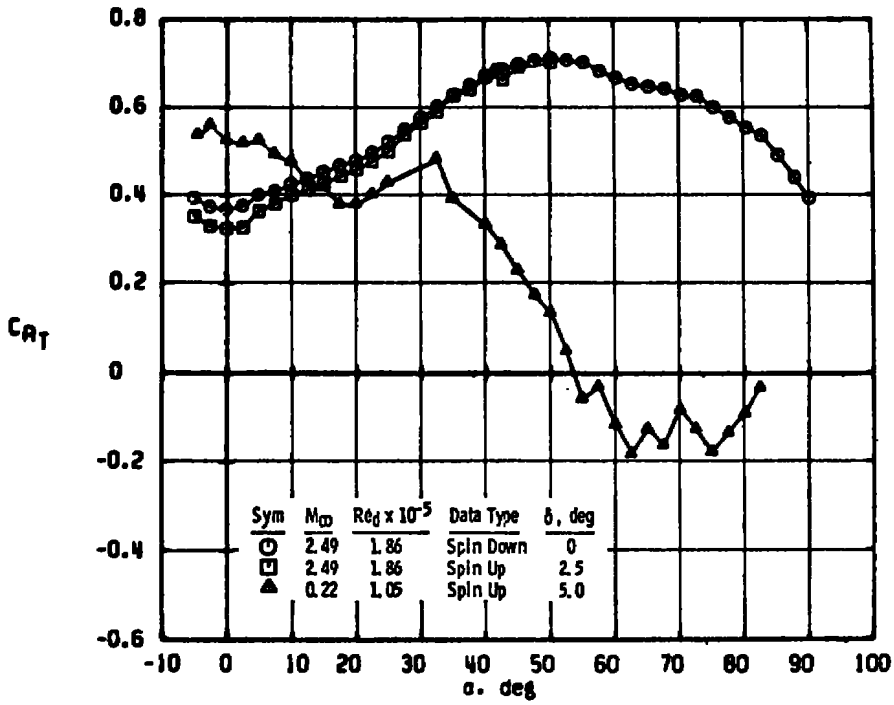

a. Effect of Mach number

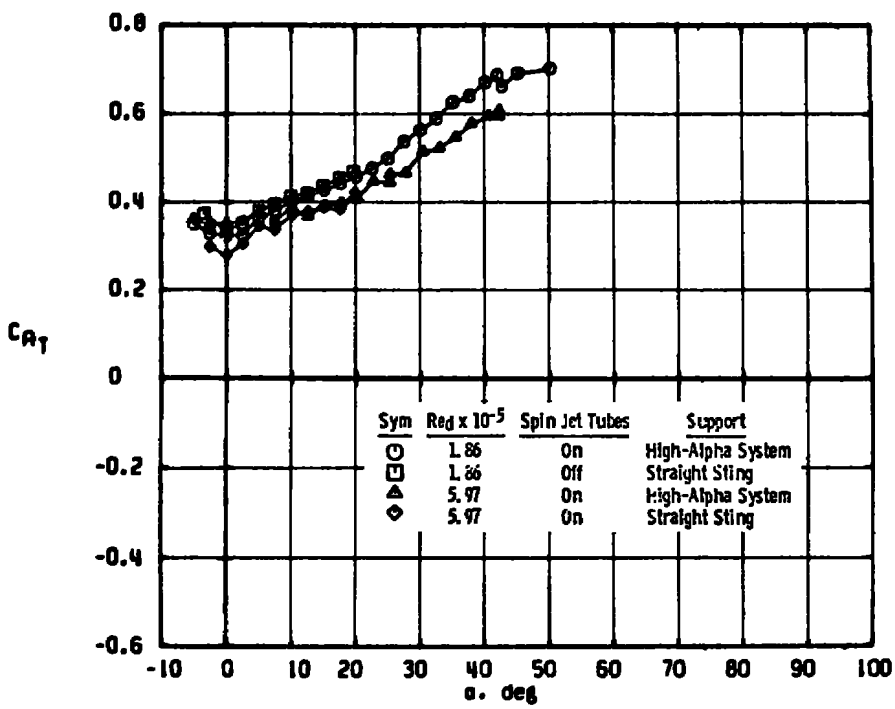

b. Effect of support system and Reynolds number, $M_\infty = 2.5$

Figure 20. Axial force characteristics of the Basic Finner Model, $p \approx 100$ radians/sec.

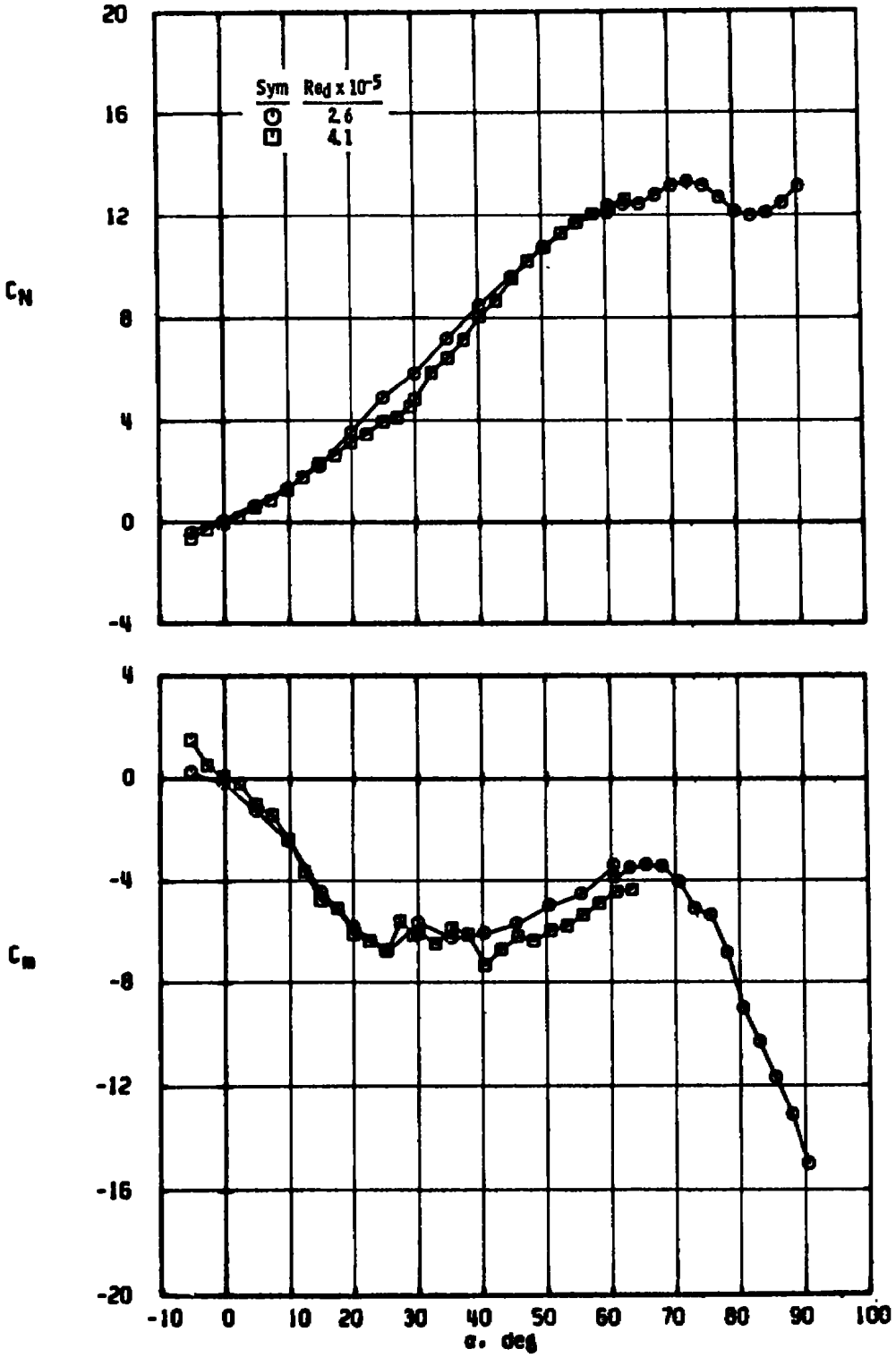

a. $M_\infty = 0.60$

Figure 21. Static longitudinal stability characteristics of the Modified Basic Finner Model, p ≈ 100 radians/sec.

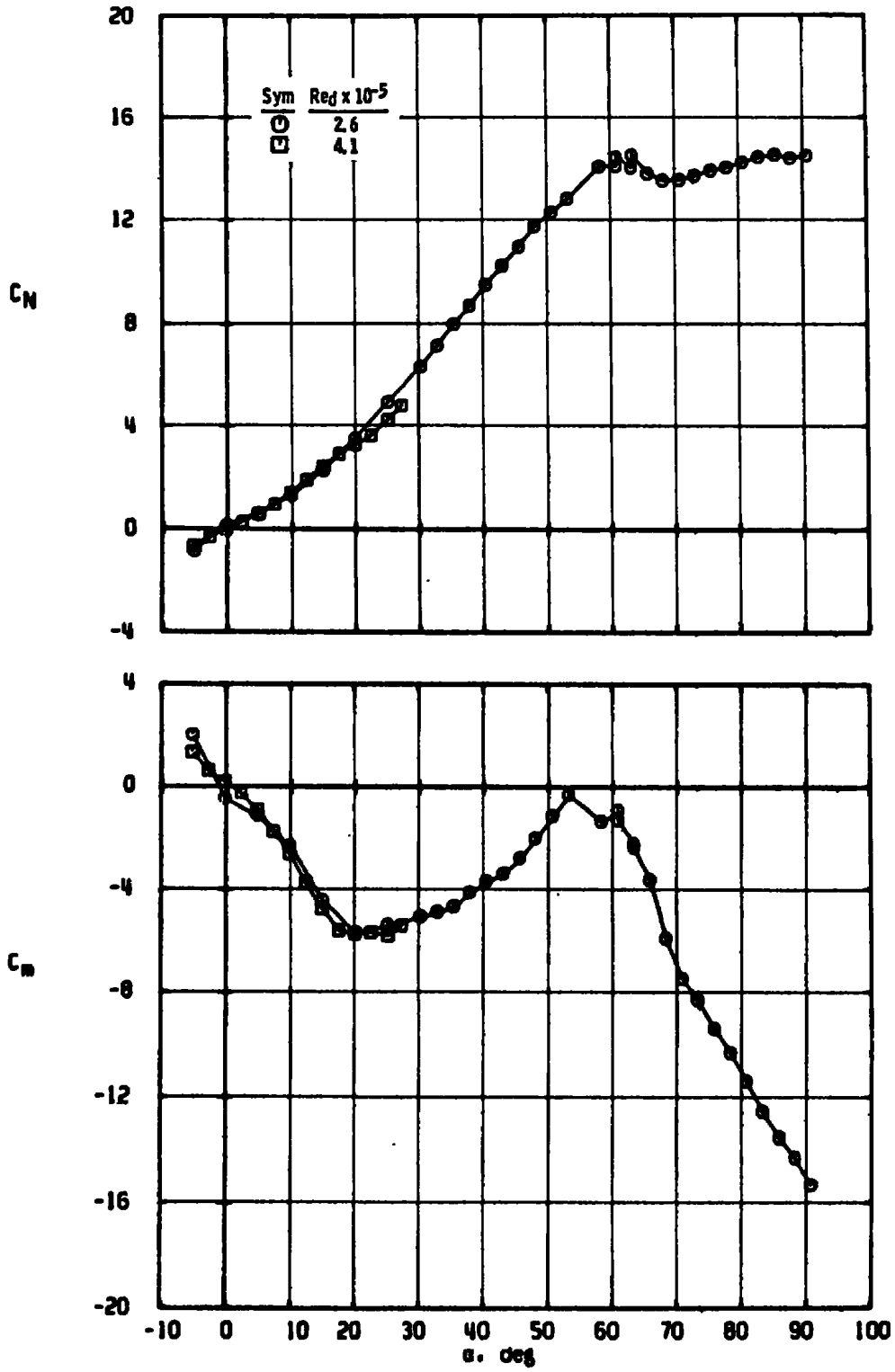

b. $M_\infty = 0.90$

Figure 21. Continued.

c. M_∞ = 1.15

Figure 21. Continued.

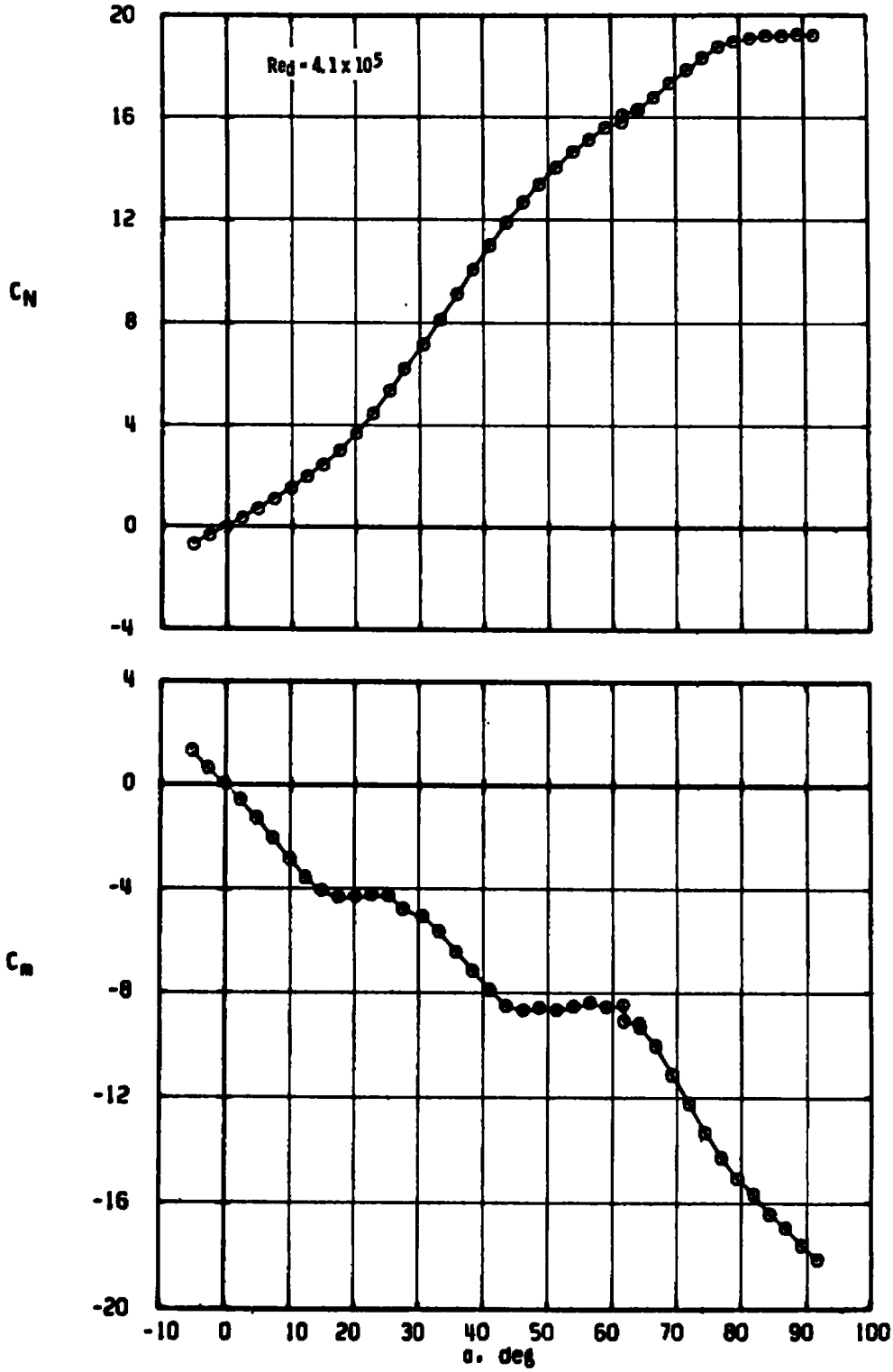

d. $M_\infty = 1.30$

Figure 21. Continued.

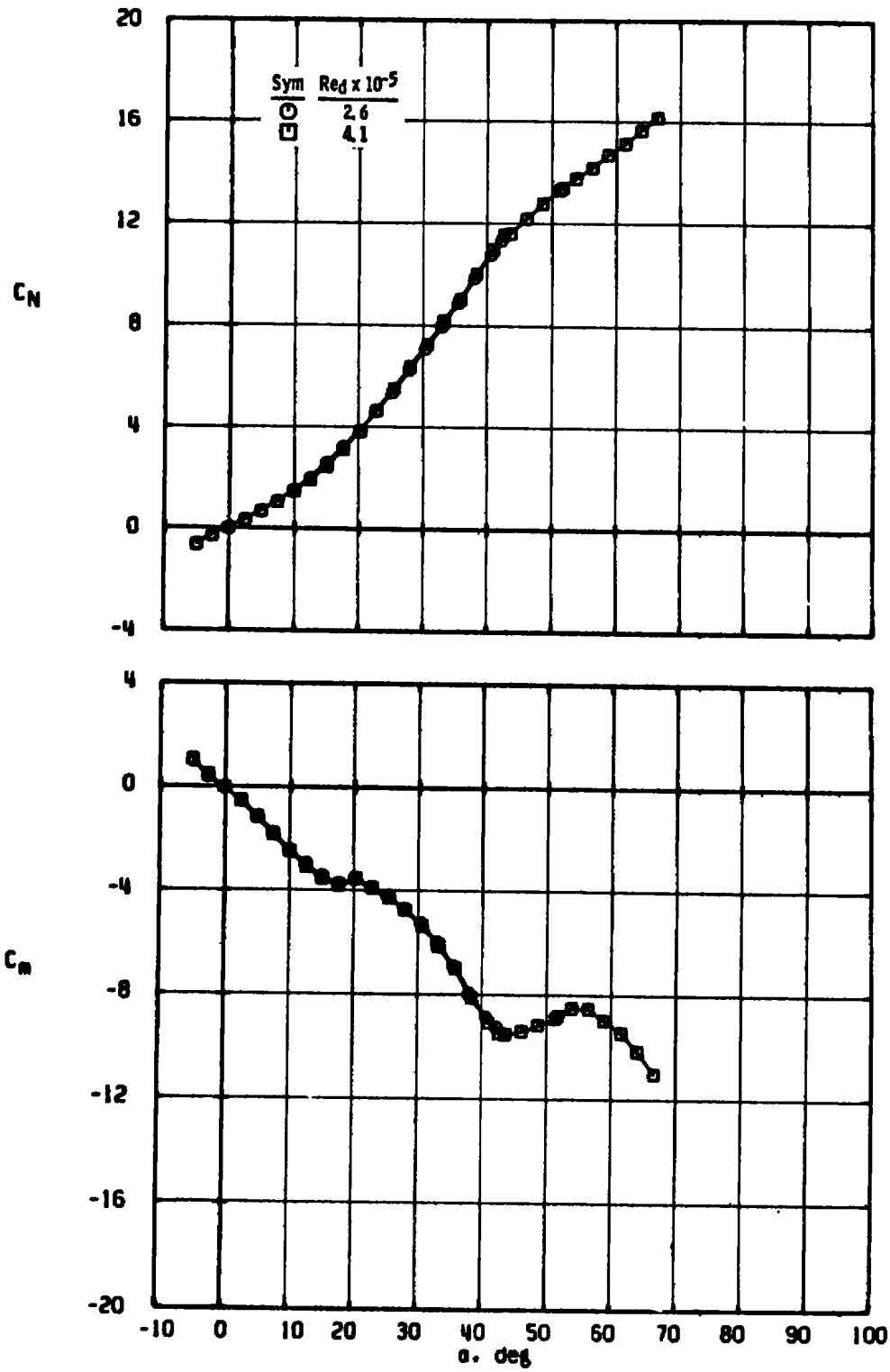

e. $M_\infty = 1.50$

Figure 21. Continued.

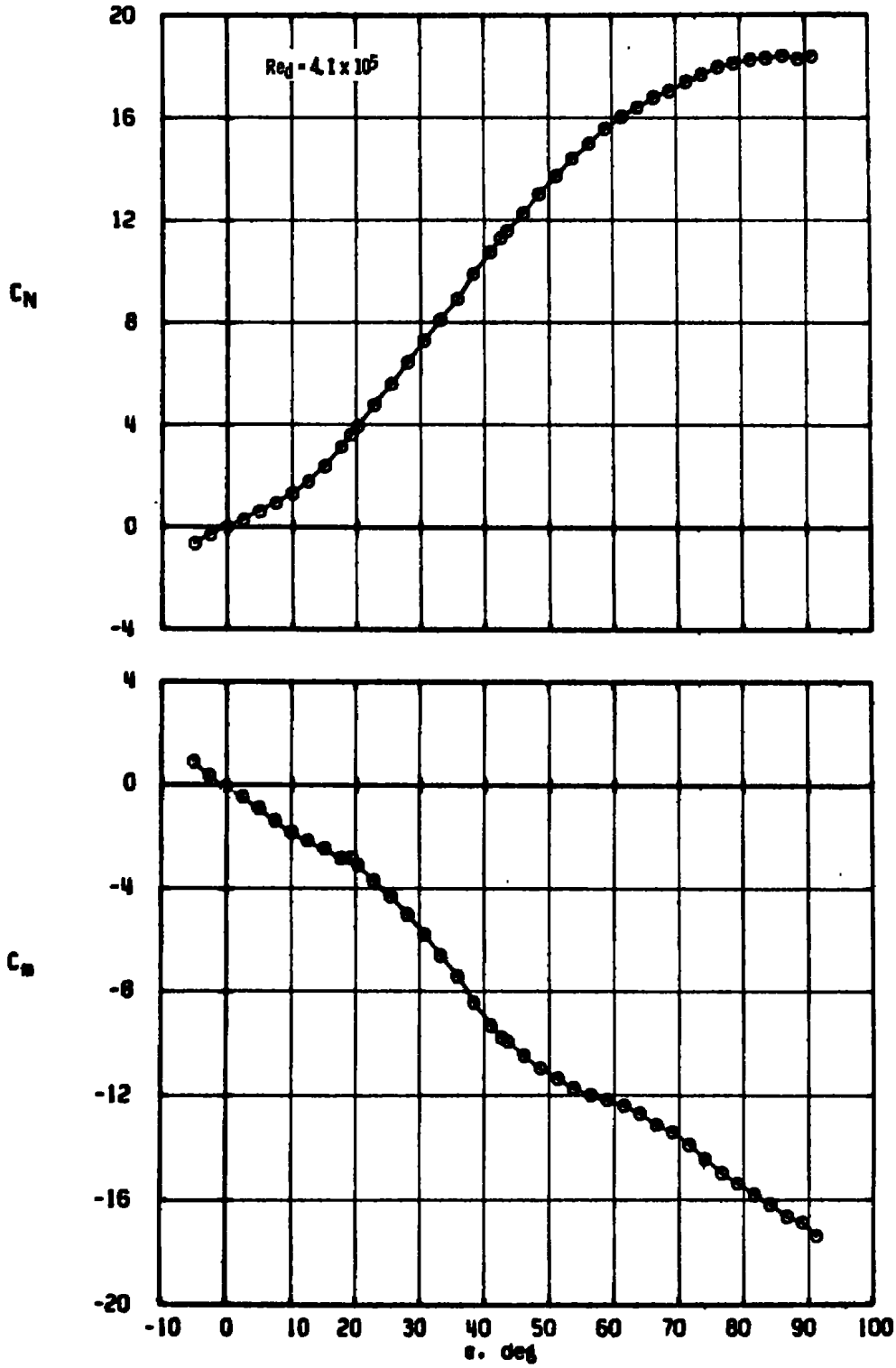

f. M_∞ = 1.76
Figure 21. Continued.

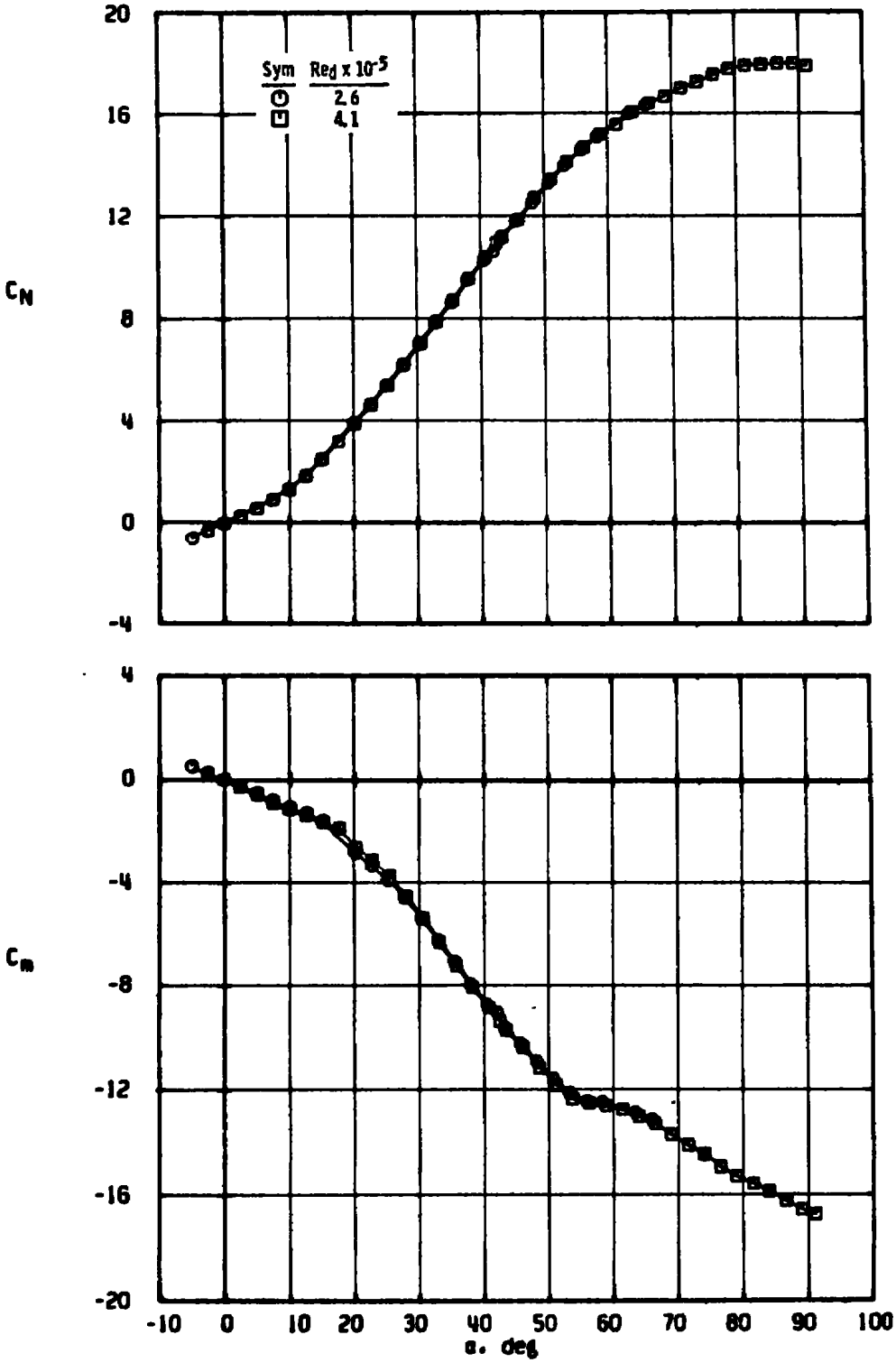

g. $M_\infty = 2.00$

Figure 21. Continued.

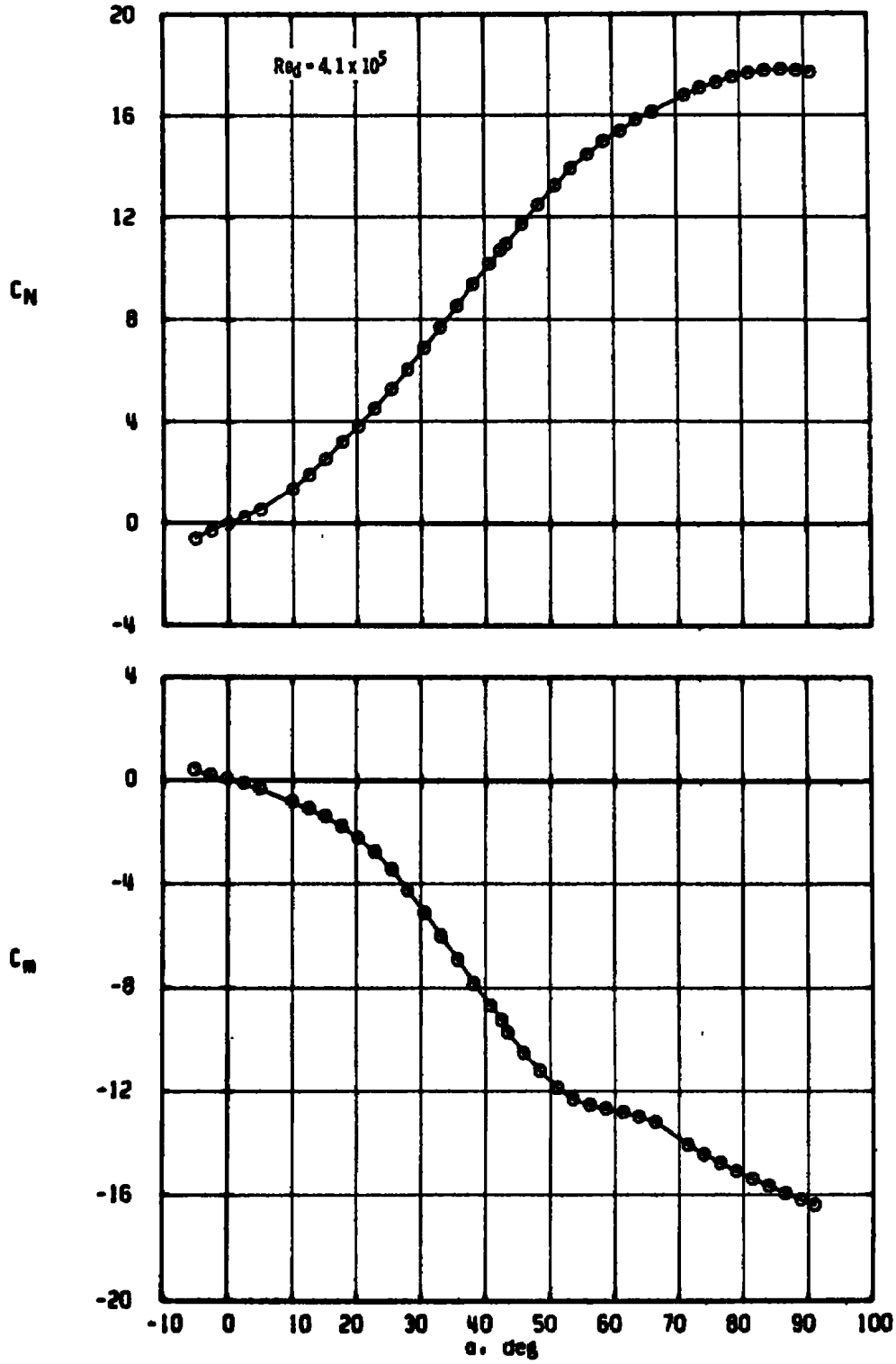

h. $M_\infty = 2.25$

Figure 21. Continued.

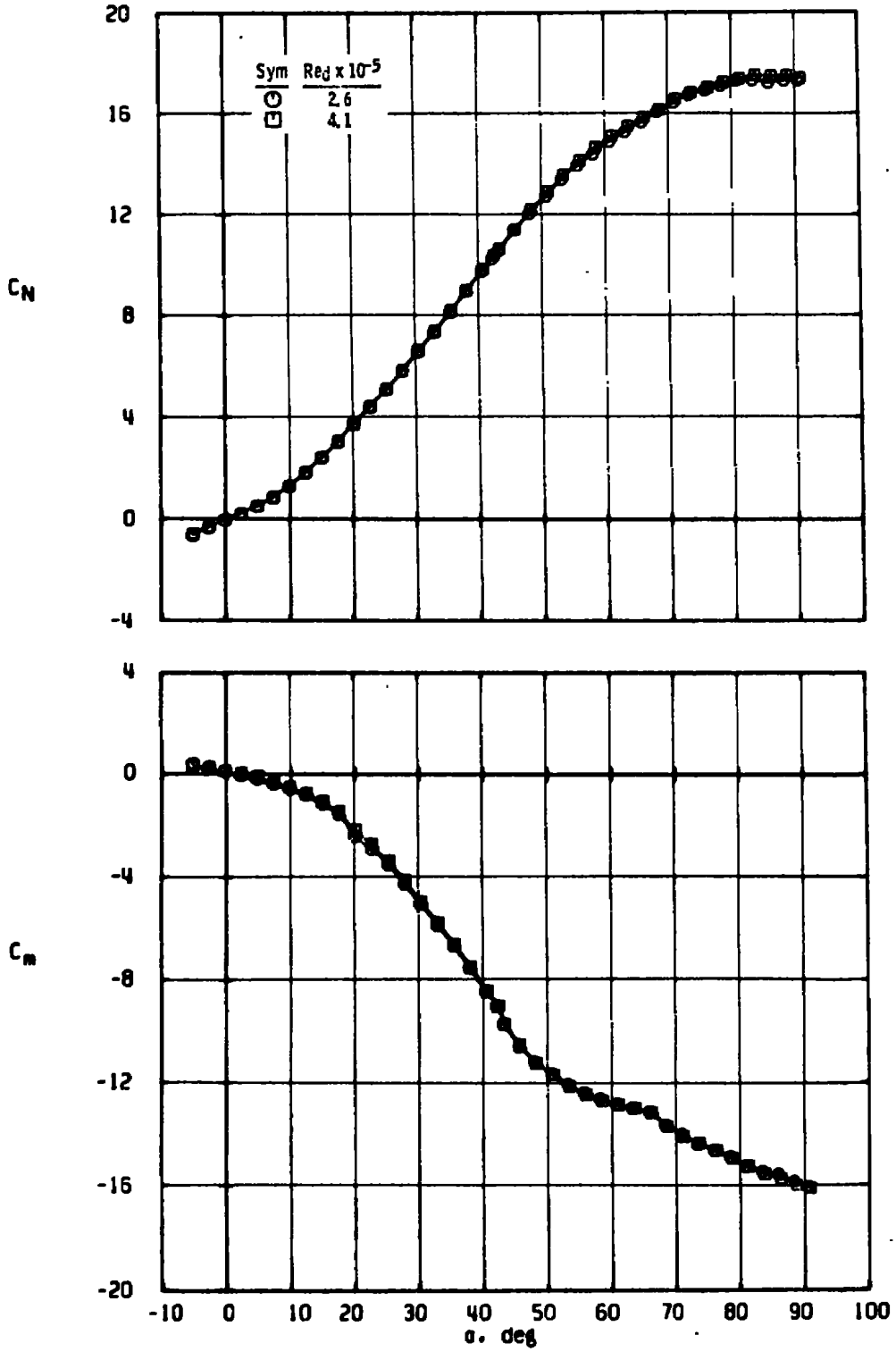

i. $M_\infty = 2.50$

Figure 21. Concluded.

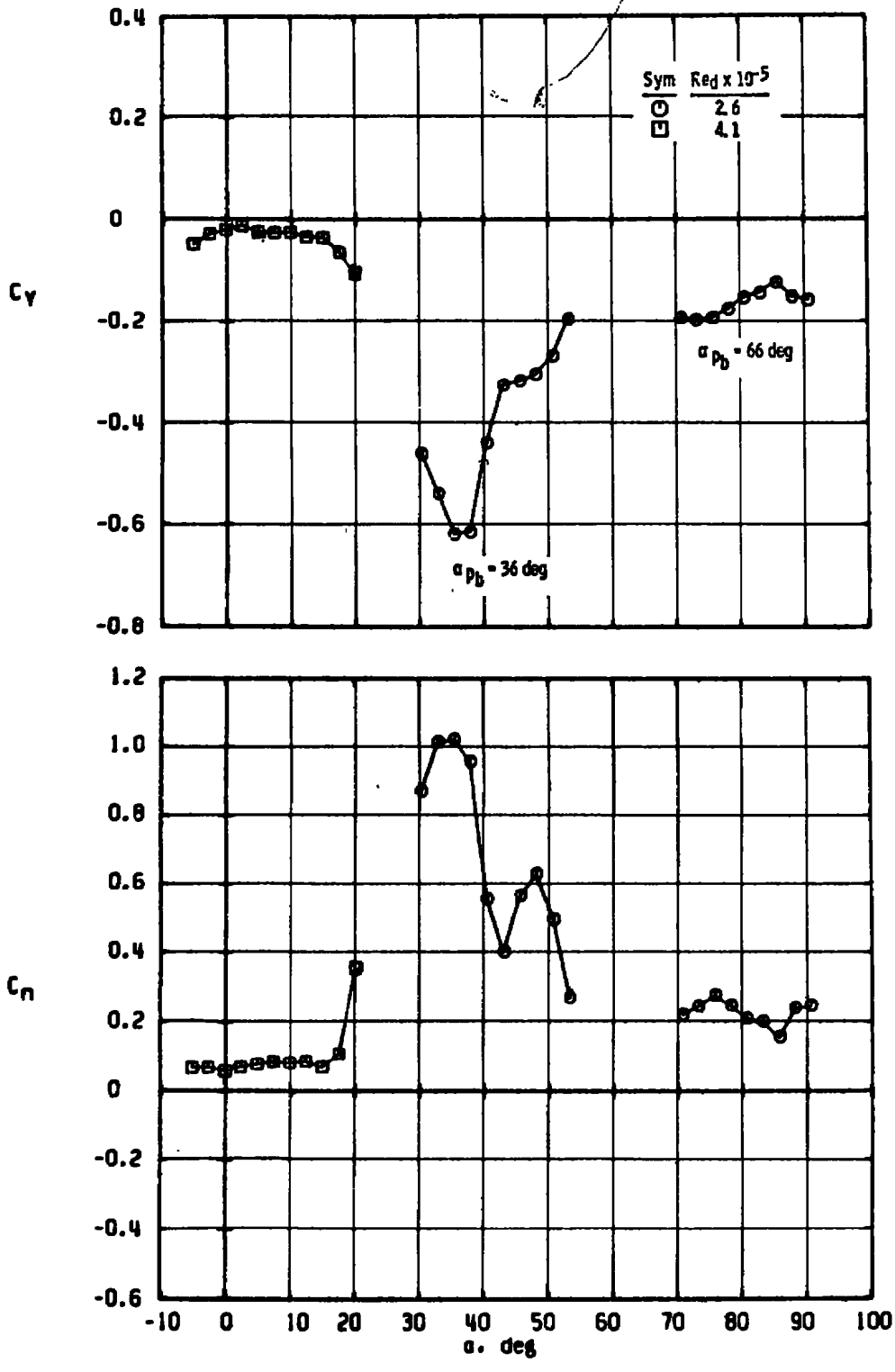

a. $M_\infty = 0.90$

Figure 22. Variation of directional stability with angle of attack for the Modified Basic Finner Model, p ≈ 100 radian/sec.

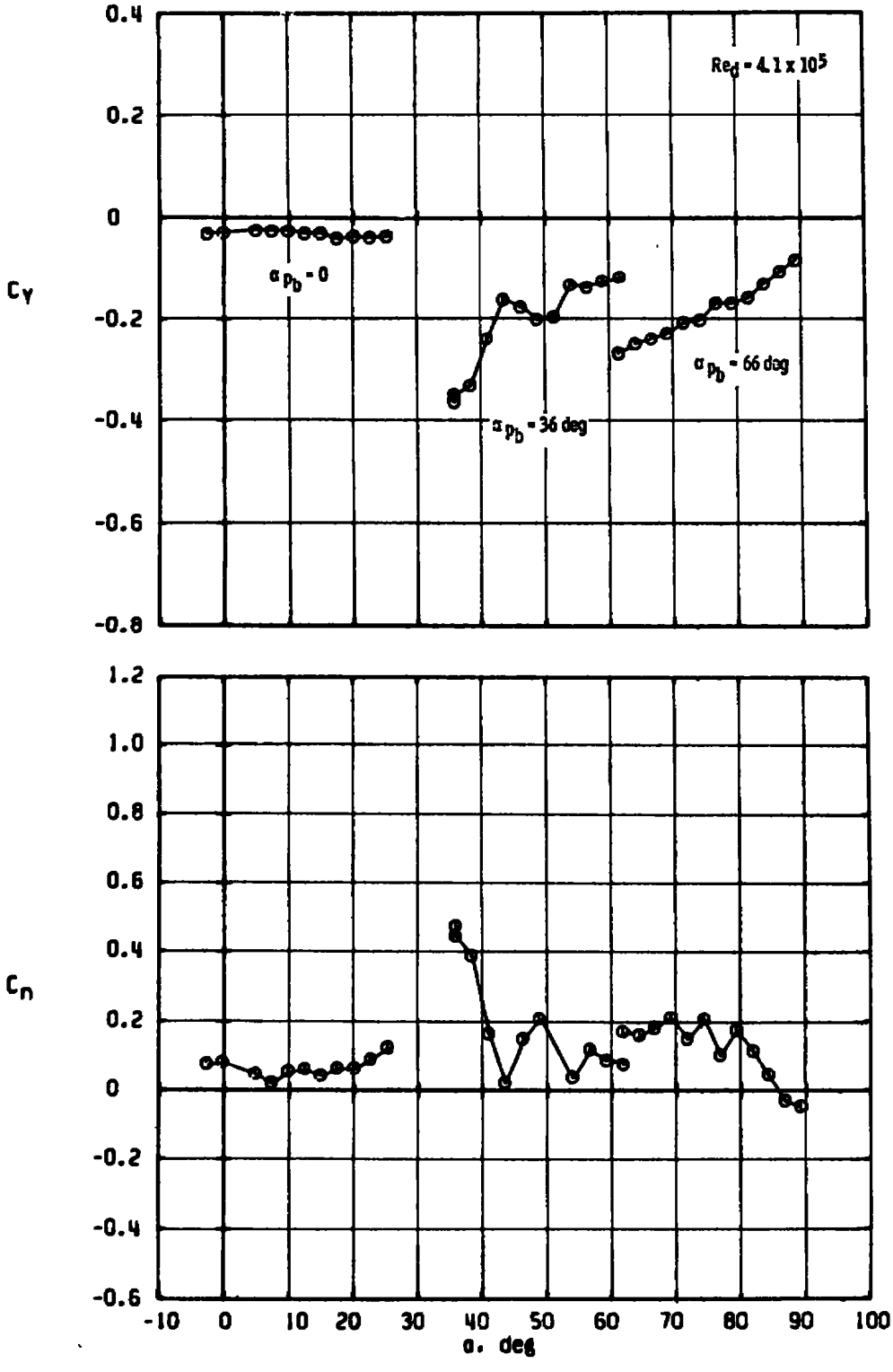

b. $M_\infty = 1.15$

Figure 22. Continued.

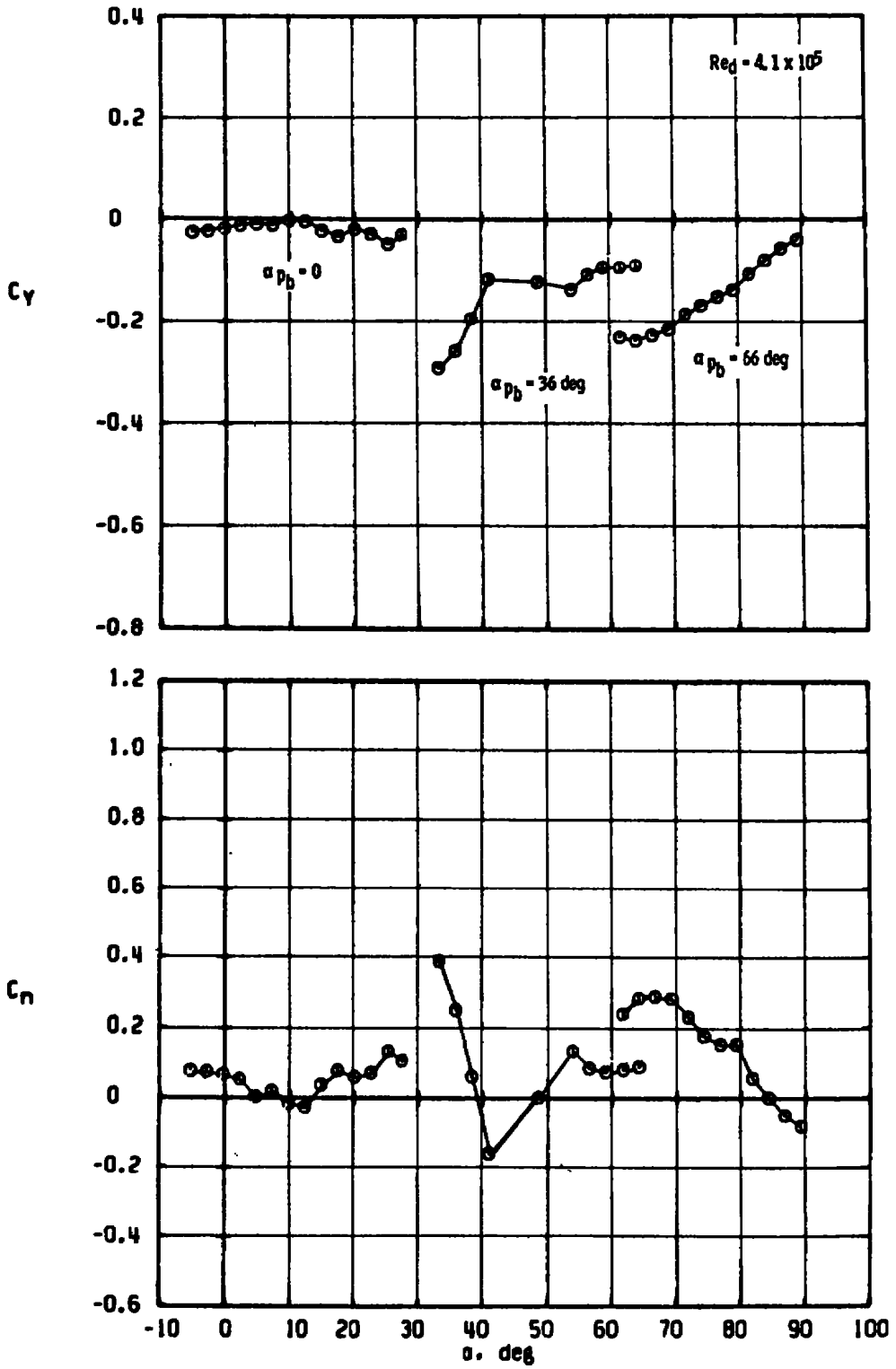

c. $M_\infty = 1.30$

Figure 22. Continued.

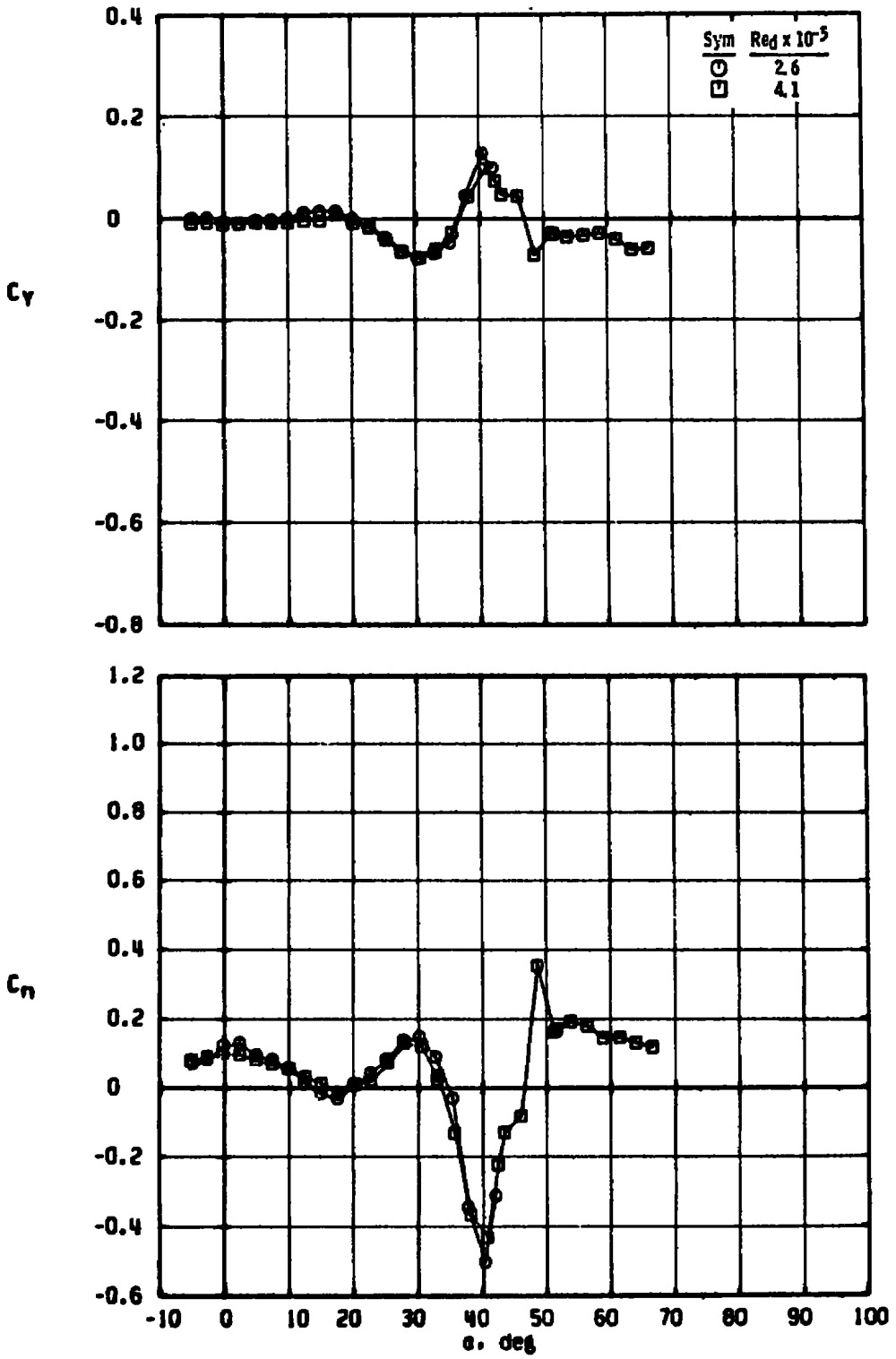

d. $M_\infty = 1.50$

Figure 22. Continued.

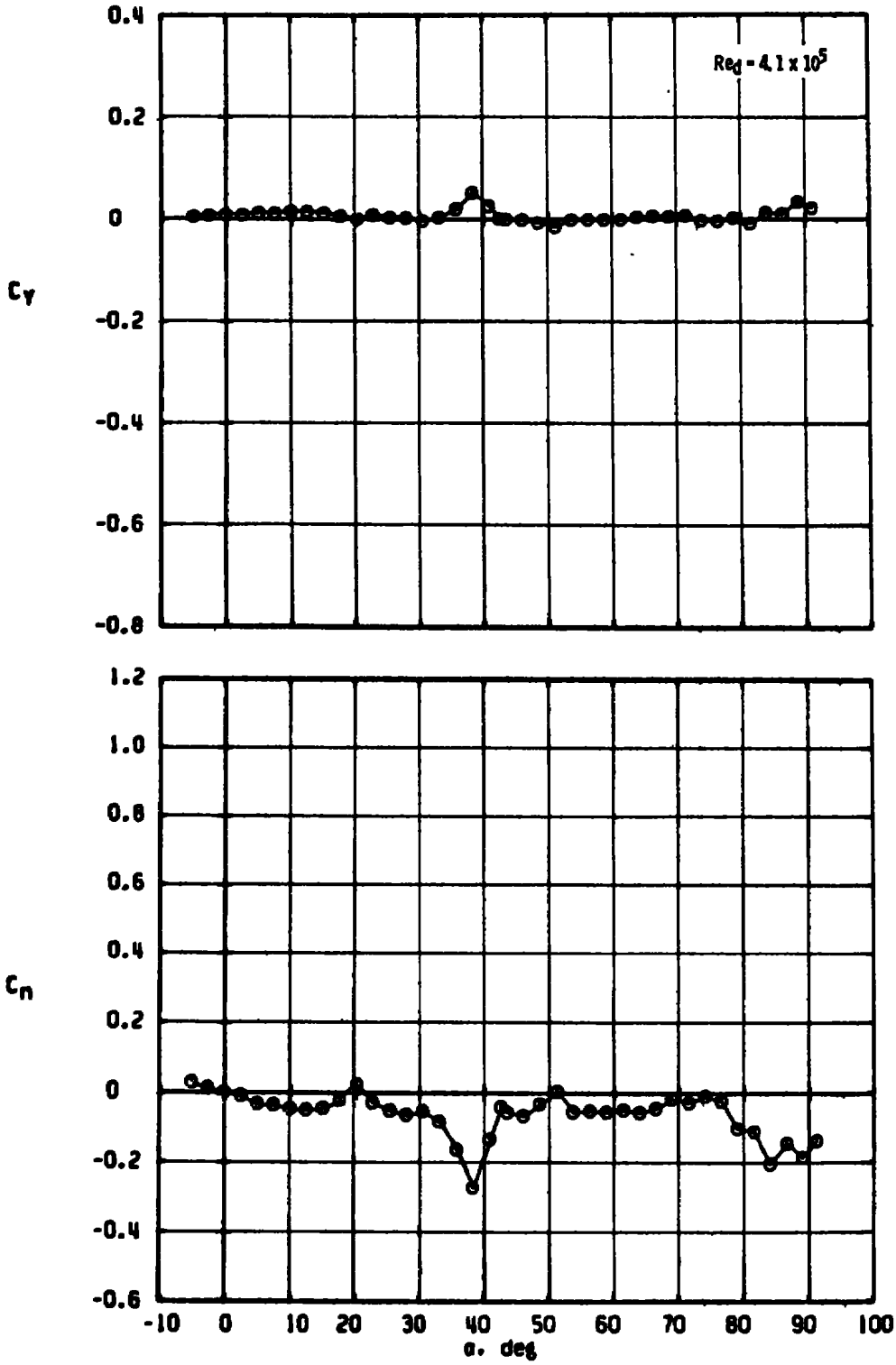

e. $M_\infty = 1.76$

Figure 22. Continued.

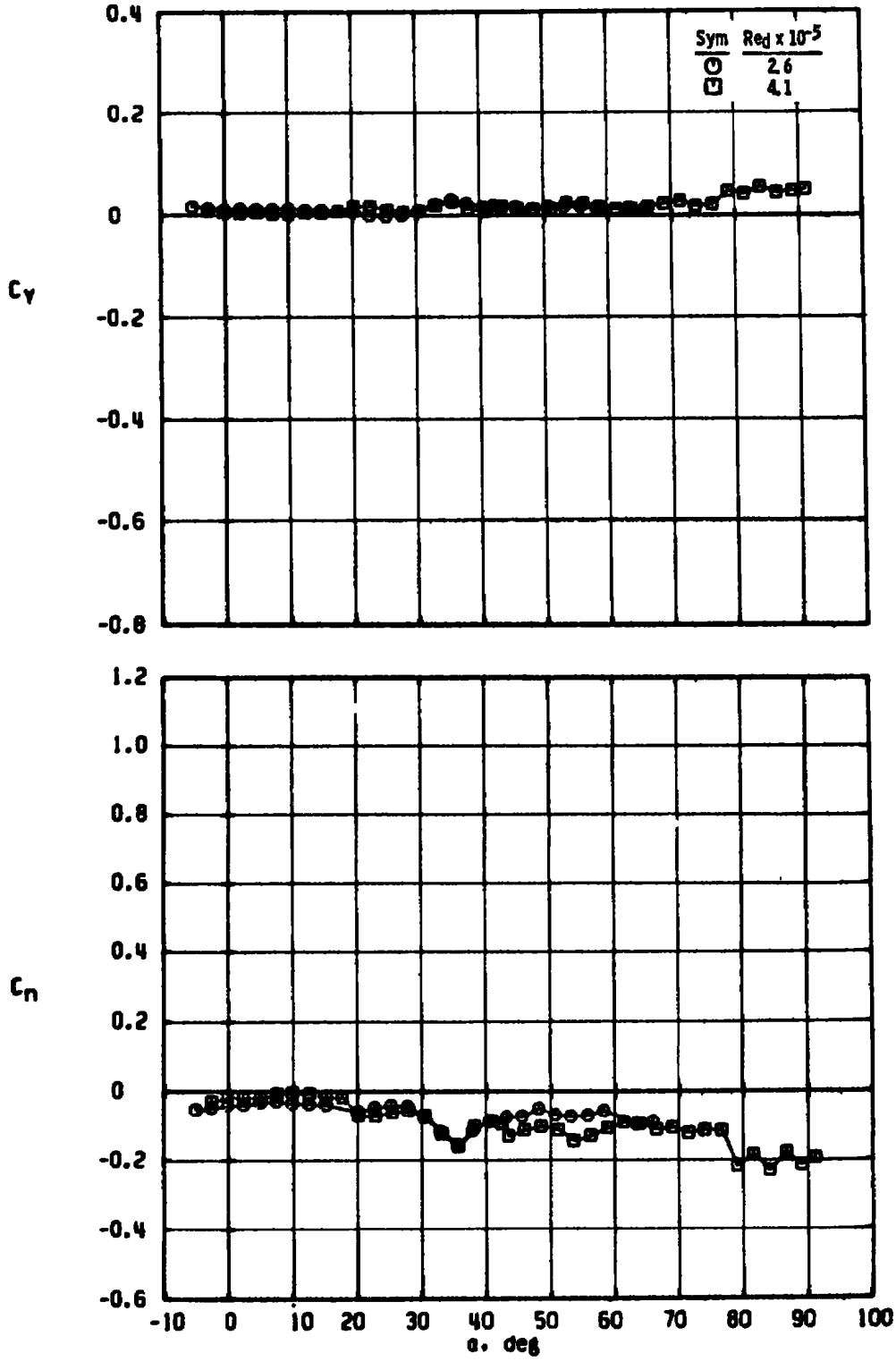

f. $M_\infty = 2.00$

Figure 22. Continued.

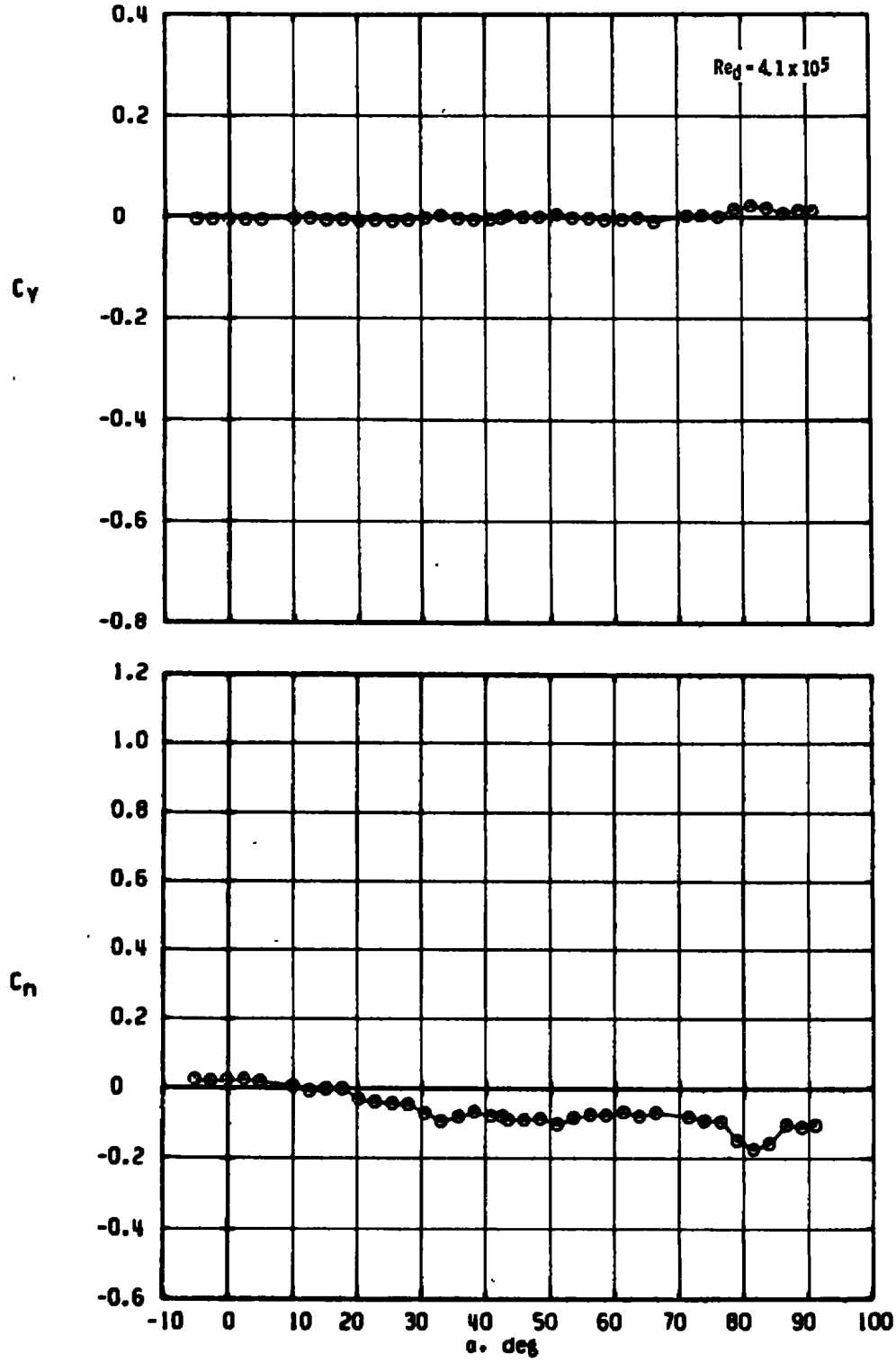

g. $M_\infty = 2.25$

Figure 22. Continued.

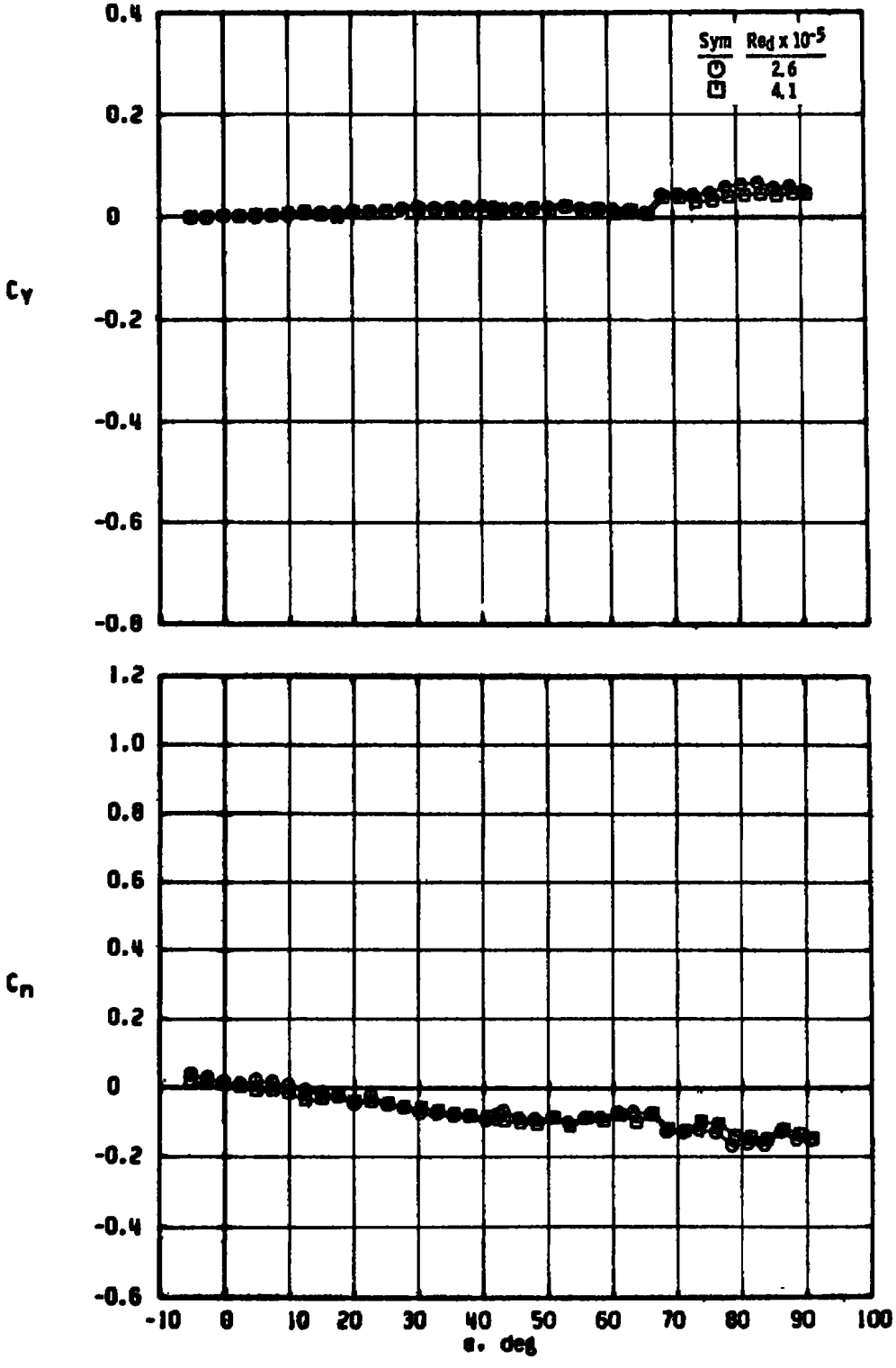

h. $M_\infty = 2.50$

Figure 22. Concluded.

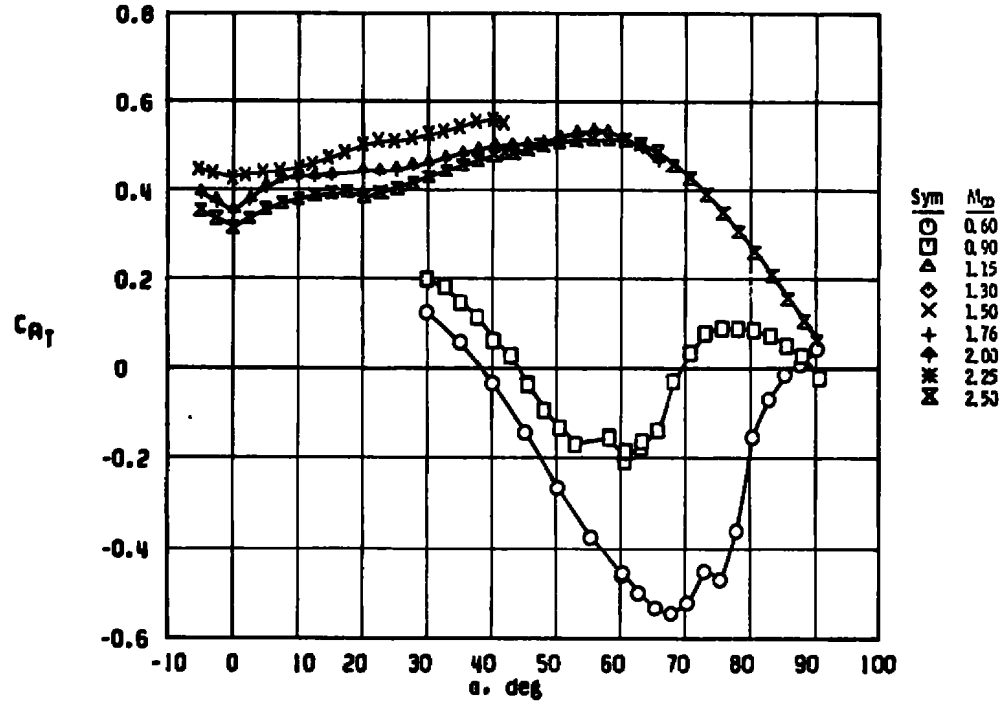

a. $Re_d = 2.6 \times 10^5$

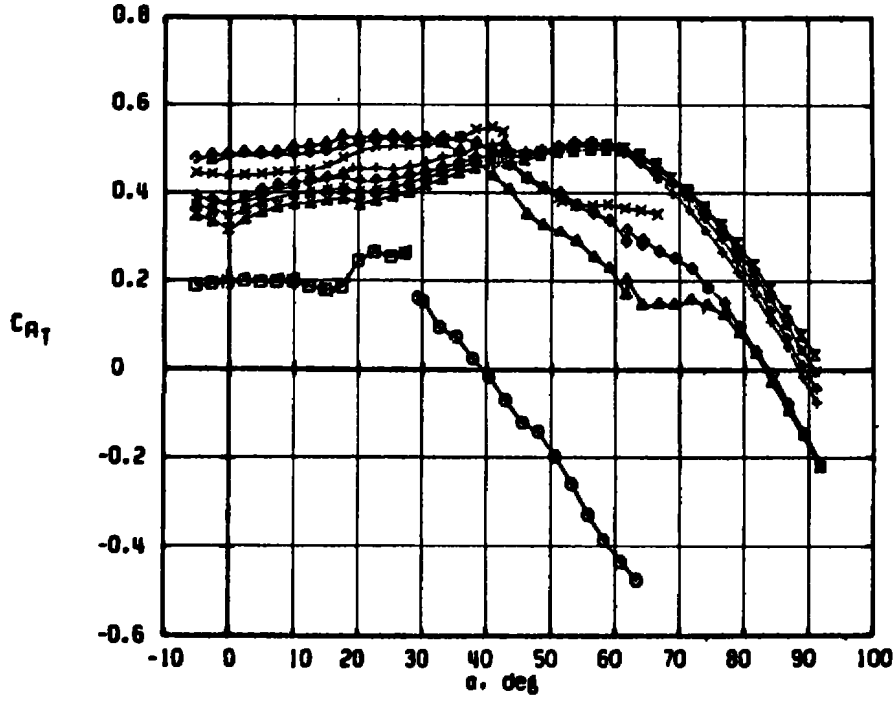

b. $Re_d = 4.1 \times 10^5$

Figure 23. Axial-force characteristics of the Modified Basic Finner Model, $p \approx 100$ radians/sec.

NOMENCLATURE

A	Reference area, 2.545 in.^{2} or 0.01767 ft^2
C_{A_T}	Total axial-force coefficient, axial force/$q_\infty A$
$C\ell_o$	Rolling-moment coefficient at p = 0, $(L_{o_W} - L_{o_B})/q_\infty Ad$
$C\ell_T$	Total rolling-moment coefficient, $(L_{T_W} - L_{T_B})/q_\infty Ad$
$C\ell_p$	Roll-damping coefficient, $\partial C\ell_T/\partial[pd/2V_\infty]$, radian^{-1}
C_m	Pitching-moment coefficient, pitching moment/$q_\infty Ad$
C_N	Normal-force coefficient, normal force/$q_\infty A$
C_n	Yawing (Magnus)-moment coefficient, yawing moment/$q_\infty Ad$
C_{n_p}	Magnus-moment spin derivative coefficient (see Section 3.3.2), $\partial C_n/\partial[pd/2V_\infty]$, radian^{-1}
C_Y	Side (Magnus)-force coefficient, side force/$q_\infty A$
C_{Y_p}	Magnus-force spin derivative coefficient (see Section 3.3.2), $\partial C_Y/\partial[pd/2V_\infty]$, radian^{-1}
d	Reference length, model diameter, 1.8 in. or 0.15 ft
$F_{N_{B_T}}$	Total bearing normal-force loading, lb
I_x	Model moment of interia (see Fig. 2), slugs-ft^2
L_o	Model static rolling moment at p = 0, ft-lb
L_{o_W}	Model-bearing system static rolling moment at p = 0 (aerodynamic plus bearing), ft-lb
L_{o_B}	Bearing static rolling moment at p = 0, ft-lb
L_p	Model roll-damping moment, ft-lb-sec/radian
L_{p_1}, L_{p_2}, L_{p_3}, L_{p_5}	Rolling-moment terms for the nonlinear equation of motion in roll, (see Section 3.3.1)

L_{p_B}	Bearing roll-damping moment, ft-lb-sec/radian
L_{p_W}	Model-bearing system roll-damping moment (aerodynamic plus bearing), ft-lb-sec/radian
L_T	Total rolling moment, ft-lb
L_{T_B}	Bearing total rolling moment, ft-lb
L_{T_W}	Model-bearing system total rolling moment (aerodynamic plus bearing), ft-lb
ℓ	Model length, 18 in. or 1.5 ft
M_∞	Free-stream Mach number
N_c	Number of constants determined in the solution of the equation of motion in roll
N_p	Number of data points fitted by the equation of motion in roll
p, ϕ	Model spin rate, radians/sec
p_I	Model initial spin rate, radians/sec
p_o	Tunnel stilling chamber pressure, psia
p_t	Vacuum tank pressure, psia
p_{ss}	Model steady-state spin rate, radians/sec
q_∞	Free-stream dynamic pressure lb/in.^{2} or lb/ft^2
Re	Free-stream Reynolds number, ft^{-1}
Re_d	Free-stream Reynolds number based on model diameter
T_o	Tunnel stilling chamber stagnation temperature, °R
t	Time, sec
t_I	Initial time, sec
V_∞	Free-stream velocity, ft/sec

x_p Distance from the model nose to the moment reference point (see Fig. 2), calibers

α Model angle of attack, deg

α_{pb} Sting prebend angle, deg

δ Model fin cant angle, deg

$\delta\phi$ Standard deviation of the roll position, $\left[\sum_{i=1}^{N_p} (\phi_c - \phi_d)_i^2/(N_p - N_c)\right]^{1/2}$

ϕ Model roll position, radian

ϕ_c Calculated model roll position from the fitted equation, radian

ϕ_d Measured model roll postion, radian

ϕ_I Initial model roll position, radian

$\dot{\phi}$, p Model roll rate, radian/sec

$\ddot{\phi}$ Model angular acceleration, radian/sec^2